



Light dark sector via thermal decays of Dark Matter: the case of a 17 MeV particle coupled to electrons

Facoltà di Scienze matematiche, fisiche e naturali
Laurea Magistrale in Fisica

Marco Graziani
ID number 1962894

Relatore Interno
Dott. Ludovico Vittorio

Relatore Esterno
Dott. Giacomo Landini

Academic Year 2024/2025

Thesis defended on 26 Gennaio 2026
in front of a Board of Examiners composed by:
Prof. Enzo Marinari (chairman)
Prof. Roberto Contino
Prof. Anna Maria Siani
Prof. Sandro De Cecco
Prof. Luca Graziani
Prof. Valeria Cimini
Prof. Luca Angelani

Light dark sector via thermal decays of Dark Matter: the case of a 17 MeV particle coupled to electrons

Sapienza University of Rome

© 2026 Marco Graziani. All rights reserved

This thesis has been typeset by L^AT_EX and the Sapthesis class.

Author's email: graziani.1962894@studenti.uniroma1.it

Abstract

Recent experimental observations, most notably those reported by the ATOMKI and Positron Annihilation into Dark Matter Experiment (PADME) collaborations, have hinted anomalies that may indicate the presence of a new resonance with a mass around 17 MeV, potentially interacting with both nucleons and electrons. Since 2020, ATOMKI has observed this resonance in nuclear transitions from excited to ground states in ^8Be , ^4He , and ^{12}C . More recently, in 2025, PADME, operating at the Laboratori Nazionali di Frascati, has also hinted a similar excess, in this case in the e^+e^- final-state events originating from positron annihilation on fixed-target atomic electrons of Carbonium. This concordance strengthens the case for a common underlying origin, potentially involving a new boson, conventionally referred to as X_{17} .

Despite these intriguing developments, the global experimental landscape remains highly dynamic, particularly in light of recent MEG II constraints, and a definitive confirmation or exclusion of the X_{17} hypothesis is still lacking.

Within this evolving and exciting context, this thesis investigates whether a hypothetical 17 MeV particle, coupled to electrons as suggested by the PADME observations, could function as a mediator between the Standard Model and previously unexplored hidden sectors. Such a mediator could, in principle, offer a novel pathway toward addressing one of the principal outstanding inconsistencies of the Standard Model: the nature and origin of dark matter.

Contents

| | | |
|----------|---|-----------|
| 1 | Introduction and Motivation | 1 |
| 1.1 | The Standard Model of Particle Physics | 1 |
| 1.2 | Dark Matter | 3 |
| 1.2.1 | Evidences of Dark Matter | 3 |
| 1.2.2 | General Properties and Theoretical models of DM | 5 |
| 1.2.3 | Dark Matter Constraints and Hints of New Physics Resonances | 7 |
| 1.3 | Hints of a Hypothetical Resonance at 17 MeV, X_{17} Boson | 7 |
| 1.3.1 | Nuclear Transitions and Spin-parity Selection Rules | 8 |
| 1.3.2 | A 17 MeV Particle Coupled to electrons and PADME hints | 10 |
| 2 | Theoretical Framework Of Our Model | 13 |
| 2.1 | The Effective Interaction Lagrangian | 13 |
| 2.1.1 | Gauge-invariant Interactions Classification | 14 |
| 2.1.2 | Model Limitations and Future Extensions | 17 |
| 2.2 | Relic Abundance Calculation: Diagram Evaluation | 18 |
| 3 | Our Model: Dark Matter Relic Abundance | 23 |
| 3.1 | Boltzmann Equation | 23 |
| 3.2 | Production Mechanisms | 26 |
| 3.2.1 | Freeze-out | 26 |
| 3.2.2 | Freeze-in Mechanism | 29 |
| 3.3 | Freeze-in Calculation | 30 |
| 3.3.1 | Freeze-in by $X \rightarrow \chi\chi$ Decay | 31 |
| 3.3.2 | Freeze-in by $e^+e^- \rightarrow \chi\chi$ Scattering | 33 |
| 3.4 | Freeze-in Abundance: Mass Regimes and Analytic Limits | 35 |
| 3.4.1 | Resonant Regime | 35 |
| 3.4.2 | Non-Resonant Regime | 37 |
| 3.4.3 | Relic-Abundance Condition and Freeze-In Parameter Space | 38 |

| | |
|---|-----------|
| 4 Our Results: Astrophysical and Low-Energy Probes | 41 |
| 4.1 Indirect Detection Searches | 41 |
| 4.1.1 X-Ray from Dark Matter Annihilations | 42 |
| 4.1.2 Limits on the Thermally-Averaged Annihilation Cross Section | 44 |
| 4.2 Final Results: Bridging Cosmological with Low-Energy Data | 48 |
| 5 Conclusions | 57 |
| A Neutrino Coupling | 59 |
| A.1 Neutrino mixing term | 60 |
| A.2 Neutrino pseudo-Yukawa term | 62 |
| B UV Completion | 65 |
| C Validity of the Narrow-Width and Non-Resonant Approximations | 67 |
| Bibliography | 71 |
| Acknowledgments | 75 |

Chapter 1

Introduction and Motivation

Recently, a series of experiments, most notably those carried out by ATOMKI [1–3] and PADME [4], have reported tensions that might hint at a new resonance with a mass around 17 MeV, possibly interacting with nucleons and electrons. At present, however, the experimental situation remains highly dynamic, also in light of the recent MEG II result [5], and a definitive confirmation or exclusion of the X_{17} hypothesis is therefore still lacking.

Within this evolving and exciting context, we aim to address in this thesis the following question: *could a hypothetical 17 MeV particle, coupled to electrons as suggested by the PADME observations, serve as a mediator describing interactions between the Standard Model and new hidden sectors?*

In this chapter we will introduce the background of this thesis, reviewing the particle content of the Standard Model, summarizing the experimental evidence supporting the existence of dark matter, and examining the current status of the 17 MeV anomalies in light of both existing data and forthcoming experimental efforts. This overview chapter summarizes the context and motivates the analyses presented in the rest of the thesis.

1.1 The Standard Model of Particle Physics

The Standard Model (SM) of particle physics provides a remarkably successful description of the fundamental constituents of matter and of their interactions. It is a quantum field theory based on the gauge symmetry group

$$\mathcal{G}_{SM} \equiv SU(3)_C \times SU(2)_L \times U(1)_Y. \quad (1.1)$$

We now briefly review the main features of the SM that will be used as the theoretical basis for the developments discussed in this thesis.

The SM Lagrangian can be decomposed into three main sectors: the fermionic sector, the gauge sector, and the Higgs sector.

The first SM sector consists of fermions, arranged in three replicated generations. Each generation contains two quarks and two leptons, differing only by their masses and mixing patterns. Quarks

carry color charge and therefore participate in strong interactions, while leptons are color singlets. The SM fermions are chiral, meaning that left-handed fields transform as doublets under $SU(2)_L$, while right-handed fields are singlets. For one generation, the fermionic content can be written as

$$Q_L = \begin{pmatrix} u_L \\ d_L \end{pmatrix}, \quad L_L = \begin{pmatrix} \nu_L \\ e_L \end{pmatrix}, \quad u_R, d_R, e_R, \quad (1.2)$$

where Q_L and L_L denote the quark and lepton weak doublets, respectively. In the SM, right-handed neutrinos are absent and neutrinos are exactly massless.

The gauge representations and hypercharges of the SM fermion fields are summarized in tab. 1.1.

| | $SU(3)_C$ | $SU(2)_L$ | $U(1)_Y$ |
|----------|-----------|-----------|----------|
| Q_L | 3 | 2 | +1/6 |
| u_R | 3 | 1 | +2/3 |
| d_R | 3 | 1 | -1/3 |
| L_L | 1 | 2 | -1/2 |
| ℓ_R | 1 | 1 | -1 |

Table 1.1 Gauge quantum numbers of one fermion generation in the SM under $SU(3)_C \times SU(2)_L \times U(1)_Y$.

The interactions among SM particles are mediated by gauge bosons associated with the gauge symmetries. The $SU(3)_C$ group describes quantum chromodynamics (QCD) and is mediated by eight massless gluons. The electroweak sector is governed by $SU(2)_L \times U(1)_Y$ and involves four gauge fields, which after electroweak symmetry breaking (EWSB) give rise to the massive W^\pm and Z bosons, as well as the massless photon.

A central ingredient of the SM is the Higgs mechanism, responsible for EWSB. The Higgs sector contains a single complex scalar doublet $H \sim (\mathbf{1}, \mathbf{2}, 1/2)$, with potential

$$V(H) = -\mu^2 |H|^2 + \lambda |H|^4. \quad (1.3)$$

When $\mu^2 > 0$, the Higgs field acquires a non-vanishing vacuum expectation value (vev), defined as

$$\langle H \rangle = \frac{1}{\sqrt{2}} \begin{pmatrix} 0 \\ v_h \end{pmatrix}, \quad v_h \equiv \sqrt{\frac{\mu^2}{\lambda}} \simeq 246 \text{ GeV}, \quad (1.4)$$

which triggers the spontaneous breaking of the electroweak gauge symmetry $SU(2)_L \times U(1)_Y$ down to the electromagnetic subgroup $U(1)_{\text{em}}$. As a consequence, the W^\pm and Z bosons acquire masses, while the photon remains massless. The Higgs mechanism also generates fermion masses through Yukawa interactions of the form

$$\mathcal{L}_Y = -y \bar{\psi}_L H \psi_R + \text{h.c.}, \quad (1.5)$$

where y are dimensionless Yukawa couplings. After EWSB, fermion masses are given by $m = y v_h / \sqrt{2}$.

The SM successfully describes a vast range of phenomena, nevertheless, it is widely regarded as an incomplete theory. It does not account for several well-established observations, including the existence of Dark Matter (DM), the small but nonzero neutrino masses, the matter–antimatter asymmetry of the Universe, and the origin of gravity. In particular, the absence of viable DM candidates within the SM strongly points to new physics, possibly indicating the existence of an additional sector, commonly referred to as a *dark sector*.

This observation forms the conceptual basis for the models explored in this thesis, where additional degrees of freedom are introduced while preserving the SM gauge structure at low energies.

1.2 Dark Matter

Observations of astrophysical systems over a wide range of length scales, from individual galaxies to the largest structures in the universe, indicate the presence of a non-luminous matter component, commonly referred to as DM. In this section we briefly summarize the main observational arguments that historically led to the formulation of the DM hypothesis. We will then review the general properties that DM must satisfy in order to be consistent with cosmological and astrophysical constraints, setting the basis for the specific framework adopted in this thesis.

1.2.1 Evidences of Dark Matter

Spiral galaxies, including the Milky Way, exhibit rotational motion around their symmetry axis. The corresponding tangential velocity profile can be experimentally reconstructed through Doppler measurements of spectral lines emitted by stars and gas clouds. An historical and a recent example are plotted in fig. 1.1.

The tangential velocity (v_{\tan}) of a test particle m (e.g., a star) at a distance r from the galactic center can be obtained from Newtonian dynamics. Equating the centripetal force to the gravitational attraction generated by the enclosed mass ($M(r)$), one finds

$$m \frac{v_{\tan}^2(r)}{r} = \frac{G m M(r)}{r^2} \quad \Rightarrow \quad v_{\tan}(r) = \sqrt{\frac{G M(r)}{r}}, \quad (1.6)$$

where G denotes Newton's gravitational constant. In spiral galaxies, the luminous matter is predominantly concentrated in the central bulge and in the disk. As a consequence, beyond a characteristic radius of order several tens of kiloparsecs, the enclosed mass is expected to approach a constant value, $M(r) \rightarrow M$. In this regime, eq. (1.6) predicts a Keplerian decrease of the tangential velocity, $v_{\tan}(r) \propto r^{-1/2}$.

Observationally, this behavior is not seen, as shown in fig. 1.1. Measurements suggest that the tangential velocity remains approximately constant out to the largest probed radii, leading to so-called flat rotation curves.

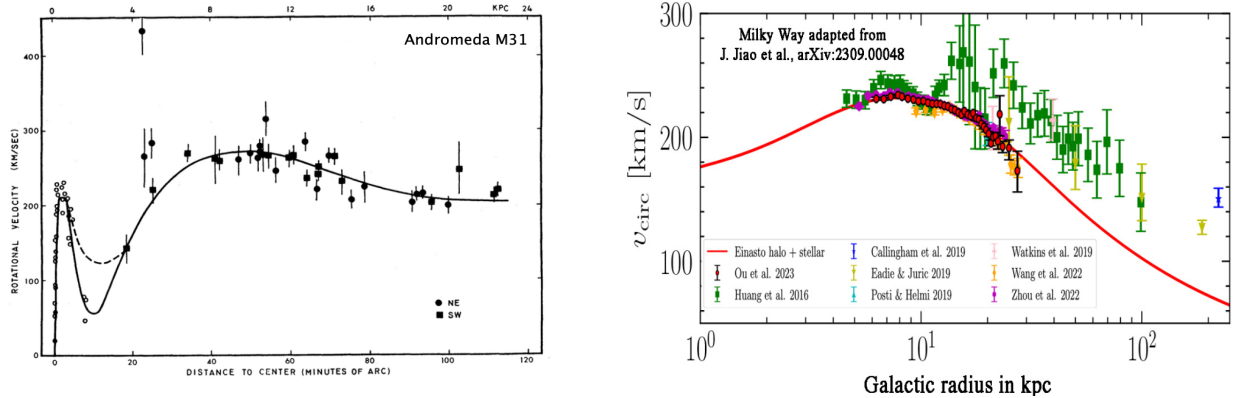


Figure 1.1 Rotation curves of spiral galaxies taken from [6]. On the left, the original rotation curve of Andromeda by Rubin and Ford (1970). On the right, a recent rotation curve for the Milky Way adapted from [7]. Both are plotted in function of the distance with respect to the center of the galaxy

To maintain a flat rotation curve, additional gravitating matter must be present at large radii. This motivates the hypothesis that galaxies are embedded in extended DM halos. From eq. (1.6), it follows that a flat rotation curve requires the enclosed mass to grow linearly with radius, $M(r) \propto r$. This behavior can be achieved if the halo density profile scales as $\rho(r) \propto \frac{1}{r^2}$, since

$$M(r) = 4\pi \int_0^r dr' r'^2 \rho(r') \propto 4\pi r \quad \Rightarrow \quad v_{\tan}(r) = \sqrt{\frac{GM(r)}{r}} \simeq \text{const.} \quad (1.7)$$

At sufficiently large distances from the galactic center, the DM halo is expected to become less dense, and the rotation curve eventually starts to decline. This qualitative behavior is supported by observations of large samples of spiral galaxies, as discussed in detail in ref. [6].

Galaxy clusters are the largest gravitationally bound systems in the Universe, and their dynamics provide an important probe of the total matter content on large scales.

One of the earliest and most influential indications of missing mass in galaxy clusters was obtained by Fritz Zwicky in 1933 through his study of the Coma Cluster. By measuring the radial velocities of cluster member galaxies, Zwicky observed velocity dispersions of order $v \sim 2000$ km/s, significantly larger than what could be accounted for by the luminous matter alone. While similar discrepancies had already been noted by Hubble and Humason, Zwicky was the first to interpret them quantitatively by applying the virial theorem.

For a system of N galaxies of mass m bound by gravity, the virial theorem implies

$$\langle K \rangle = -\frac{1}{2} \langle V \rangle \quad \Rightarrow \quad N \frac{mv^2}{2} = \frac{N^2 G m^2}{4R} \Rightarrow M \equiv Nm = \frac{2Rv^2}{G}, \quad (1.8)$$

where R denotes the characteristic size of the cluster. Inserting the observed values for the Coma Cluster, Zwicky found that the inferred total mass exceeds the mass associated with luminous matter by more than an order of magnitude.

The observations discussed above represent only the earliest historical evidence that motivated the introduction of DM. Over the years, a wide range of independent and complementary observations has further strengthened this hypothesis, including gravitational lensing, cosmic microwave background anisotropies, large-scale structure formation, and precision cosmology. A detailed discussion of these additional probes goes beyond the scope of this thesis and can be found in Ref. [6].

Having established the empirical motivation for the existence of DM, we now turn to a discussion of its general properties, which will guide the construction and analysis of the particle-physics models considered in this thesis.

1.2.2 General Properties and Theoretical models of DM

A first and fundamental requirement concerns the present-day DM density (ρ_{DM}). In cosmology, the quantity used to account for ρ_{DM} is the parameters combination $\Omega_{DM} = \rho_{DM}/\rho_{cr}$, where $\rho_{cr} = 3H_0^2/8\pi G$ is the critical density of the universe. Defining the parameter h as $H_0 = h \times 100 \text{ km s}^{-1} \text{ Mpc}^{-1}$, the explicit dependence of the Hubble constant H_0 may be removed, hence hereafter we will consider directly the quantity $\Omega_{DM} h^2$. This observable is known with extreme precision through the measurement of the peaks of the cosmic microwave background (CMB) by the Planck Collaboration [8]

$$\Omega_{DM} h^2 = 0.1200 \pm 0.0012. \quad (1.9)$$

At present, the mass of DM is essentially unconstrained. Both theoretical arguments and observational considerations allow it to span an enormous range, covering roughly ninety orders of magnitude. Constraints however can nonetheless be derived by considering generic astrophysical arguments.

A lower bound on the DM mass follows from the requirement that its de Broglie wavelength fits inside dwarf galaxies, leading to (see [9])

$$m_{DM} \gtrsim 10^{-21} \text{ eV}. \quad (1.10)$$

In principle a particle cannot be heavier than M_{Pl} , otherwise it would be a black hole. However, Dark matter could be composed of composite compact objects. In this case, the relevant requirement is that the constituents of such objects are not themselves black holes. A simple heuristic estimate reported in [6] is that their mass should not exceed that of the smallest dwarf galaxies

$$m \lesssim 10^4 M_{\odot} \simeq 10^{34} \text{ kg}, \quad (1.11)$$

and this gives an upper bound on DM mass.

Depending on its mass, DM can therefore exhibit qualitatively different physical behaviors, motivating the classification of DM candidates into three distinct regimes, as illustrated in fig. 1.2: fields, particles and macroscopic objects.

1. Fields: if the DM mass is $M_{DM} \ll \text{eV}$, it will behave like a classical field.

This is analogous to the electromagnetic field: for such light DM, the number of particles

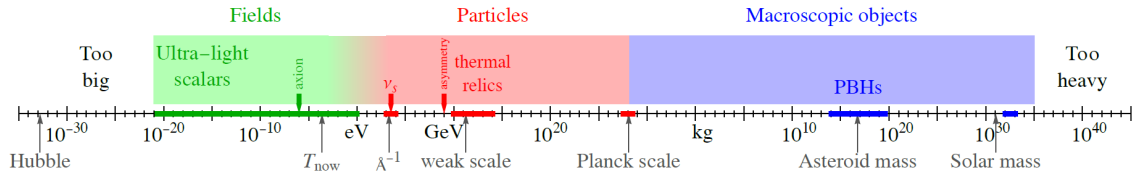


Figure 1.2 Possible mass range for DM candidates. In this work, we focus specifically on the MeV region.

required to account for the observed gravitational effects is enormous, so—as in the case of many photons—it is more convenient to describe it as a classical field.

2. **Particles:** in this case, we are in the range $eV < m_{DM} < M_{Pl}$. The upper limit is motivated by the fact that, for masses larger than the Planck scale, an object would collapse and should be regarded as a black hole rather than as an elementary particle.
3. **Macroscopic objects:** in this regime the DM is not described in terms of elementary particles, but rather as composite objects with masses exceeding the Planck scale, $m_{DM} > M_{Pl}$. Such objects are intrinsically macroscopic and behave as classical gravitating bodies. Examples that are often discussed in the literature include Massive Astrophysical Compact Halo Objects (MACHOs) and primordial black holes, among other possibilities.

In this thesis we focus on the second hypothesis, namely that DM is composed of elementary particles. Under this assumption, a viable DM particle candidate must satisfy a number of general requirements, which can be summarized as follows:

- Particle DM must be *cold*, meaning that it is non-relativistic at the time of matter–radiation equality. This condition is required in order for DM to efficiently cluster and drive the formation of large–scale structures.
- DM must be electrically neutral, or carry at most an extremely small electric charge. Strong bounds from cosmology, astrophysics and laboratory experiments constrain any possible electromagnetic interaction to be many orders of magnitude weaker than ordinary SM interactions.
- The interaction strength of DM with SM particles must be sufficiently suppressed. In particular, experimental bounds imply that the elastic scattering cross section of DM on ordinary matter is well below a typical weak–scale cross section over a wide range of masses. This requirement severely restricts the allowed range of couplings between DM and SM fields.
- DM self–interactions must also be limited. Large self–interaction cross sections would modify the dynamical behavior of DM in galaxies and clusters, in conflict with observations that indicate that DM behaves, to a good approximation, as a collisionless component on astrophysical scales.

- Finally, DM must be stable on cosmological timescales, or at least its lifetime (τ_{DM}) must be greater than the age of the universe $T_U \approx 13.8$ Gyr. If DM were unstable, its decay products would leave observable imprints in cosmological and astrophysical data, which are not seen. This requirement is often enforced by imposing an exact or approximate symmetry that forbids DM decay.

It is worth commenting on the allowed mass range for fermionic DM. Unlike bosonic candidates, fermionic DM is subject to the Pauli exclusion principle, which imposes the stronger, well-known Gunn-Tremaine bound [10, 11]. For the Milky Way halo, this implies a lower limit of order

$$m_{DM} \gtrsim \mathcal{O}(0.1\text{-}1) \text{ keV.} \quad (1.12)$$

For the purposes of this thesis, and in order to keep the phenomenological analysis as simple and transparent as possible, we will restrict ourselves to DM masses in the range from the MeV to the GeV scale. This choice is primarily motivated by the experimental anomalies and detection strategies discussed in the following sections.

1.2.3 Dark Matter Constraints and Hints of New Physics Resonances

The above general considerations define the theoretical framework within which particle DM models are constructed and will guide the model-building strategy and the phenomenological analyses developed in the following chapters. In particular, they motivate the study of minimal and predictive extensions of the SM that can provide a *viable DM candidate* while remaining consistent with the wide range of existing experimental constraints.

Processes involving DM and SM particles can be grouped into three broad phenomenological categories, according to the experimental strategy that is sensitive to them. Indirect-detection (ID) experiments search for SM particles produced in DM annihilations or decays in astrophysical environments. Direct-detection experiments instead aim at observing the effect of DM particles coming from the galactic halo scattering off SM targets. Finally, collider searches look for the production of DM in high-energy collisions of SM particles, typically through missing-energy signatures. These three classes of processes, and their connection through the DM–SM mediator, are schematically summarized in fig. 1.3.

In this broader context, it is also useful to consider experimental hints that may point at physics beyond the SM and that may be properly connected to DM physics. Among these, particular attention has been drawn to the so-called X_{17} anomaly, which if confirmed is a new physics particles with light mass. In the next section, we summarize the current experimental status of this X_{17} anomaly, and discuss its possible theoretical implications within the framework outlined above.

1.3 Hints of a Hypothetical Resonance at 17 MeV, X_{17} Boson

Over the last decade, a series of intriguing anomalies observed by the ATOMKI collaboration in nuclear transition experiments has sparked considerable interest in the possibility of new physics at

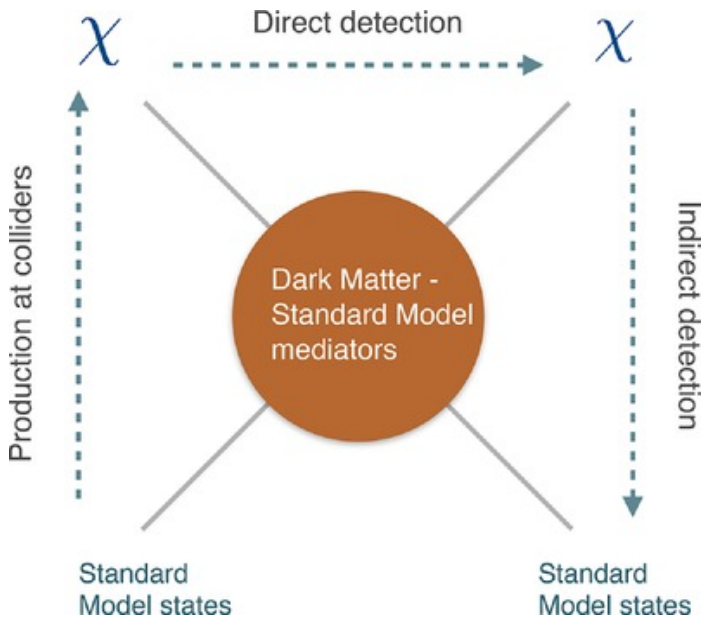


Figure 1.3 Schematic representation of the three main experimental strategies to probe particle DM: indirect detection, direct detection, and collider searches. They correspond respectively to SM final states from DM, DM-SM scattering, and DM production from SM collisions. The symbol χ denotes the dark-matter particle. Image taken from [12].

the MeV scale. The anomalies were first reported in processes associated with excited nuclear states of ${}^8\text{Be}$, and were later reinforced by similar observations in transitions involving ${}^4\text{He}$ and ${}^{12}\text{C}$.

In this section we will first review these experimental results and discuss their possible interpretation in terms of a new light neutral boson, commonly referred to as X_{17} . We will then revisit how nuclear transition properties can be used to assess which combinations of spin and parity are more compatible with the available data. Finally, we will then turn to a putative 17 MeV resonance hinted by PADME experiment at 1.7σ via e^+e^- annihilation.

1.3.1 Nuclear Transitions and Spin-parity Selection Rules

Since 2020, anomalous features have been reported in the angular distributions of electron-positron pairs emitted in nuclear transitions by the ATOMKI collaboration. These anomalies were first observed in internal pair creation (IPC) processes associated with excited states of ${}^8\text{Be}$ [1]. Subsequently, similar deviations from SM expectations were reported in nuclear transitions of ${}^4\text{He}$ [2] and ${}^{12}\text{C}$ [3]. In all cases, the anomaly manifests itself as an excess of e^+e^- pairs at large opening angles between the electron and the positron. Such a behavior cannot be accounted for by conventional IPC alone and suggests the presence of an intermediate particle emitted in the nuclear transition and decaying promptly into an electron-positron pair. The data can be consistently interpreted by postulating the emission of a new, light, electrically neutral boson with a mass of about 17 MeV, commonly referred to as X_{17} . In this interpretation, the nuclear transition proceeds through the emission of the X_{17} ,

| Process | $S^\pi = 1^-$ | $S^\pi = 1^+$ | $S^\pi = 0^-$ | $S^\pi = 0^+$ |
|--|---------------|---------------|---------------|---------------|
| ${}^8\text{Be}(18.15) \rightarrow {}^8\text{Be}$ | 1 | 0, 2 | 1 | / |
| ${}^8\text{Be}(17.64) \rightarrow {}^8\text{Be}$ | 1 | 0, 2 | 1 | / |
| ${}^4\text{He}(21.01) \rightarrow {}^4\text{He}$ | / | 1 | 0 | / |
| ${}^4\text{He}(20.21) \rightarrow {}^4\text{He}$ | 1 | / | / | 0 |
| ${}^{12}\text{C}(17.23) \rightarrow {}^{12}\text{C}$ | 0, 2 | 1 | / | 1 |

Table 1.2 Allowed values of the orbital angular momentum L of the emitted X boson for different choices of its spin-parity S^π . The symbol "/" corresponds to forbidden transitions, excluded by angular momentum and parity conservation

followed by the decay $X_{17} \rightarrow e^+e^-$, leading to a characteristic angular correlation that matches the observed excess.

Given the set of nuclear anomalies reported by the ATOMKI collaboration, a natural question concerns the spin and parity quantum numbers of the hypothetical X_{17} boson. Once the mass scale is fixed by kinematics, the consistency of the interpretation hinges on whether the observed nuclear transitions are dynamically allowed for a given spin-parity assignment of X_{17} . For each nuclear transition, angular momentum and parity conservation impose selection rules. These constraints determine whether the emission of an intermediate boson with given spin J and parity π is allowed, and, if so, which values of the orbital angular momentum L between the final nuclear state and the emitted boson are permitted. In this way, each anomaly can be mapped onto a set of allowed or forbidden spin-parity assignments for X_{17} .

The results of this analysis are summarized in table 1.2, where we report, for each nuclear transition involved in the ATOMKI anomalies, the allowed values of the orbital angular momentum L associated with the emission of an X_{17} boson with definite spin and parity. Entries marked as "/" correspond to forbidden transitions. From the table, two robust conclusions can be drawn. First, the beryllium transitions exclude a CP-even scalar interpretation of X_{17} , as no value of the orbital angular momentum satisfies the required selection rules. Second, the carbon transition rules out a pseudoscalar assignment, since the corresponding emission is forbidden by parity conservation. As a consequence, not all spin-parity hypotheses are compatible with the full set of observed anomalies. These considerations significantly restrict the viable quantum numbers of X_{17} and play a central role in guiding the theoretical interpretation of the ATOMKI results.

At this point it is useful to add a brief remark motivated by recent experimental activity. The MEG-II collaboration has investigated the same excited ${}^8\text{Be}$ transitions that, according to table 1.2, would exclude a CP-even scalar interpretation of X_{17} . No statistically significant signal was observed in this channel. This result has prompted a renewed discussion in the literature, and in particular a

re-assessment of whether a scalar X may still be viable once theoretical uncertainties and modelling assumptions entering the nuclear–transition analysis are taken into account, see ref. [13].

1.3.2 A 17 MeV Particle Coupled to electrons and PADME hints

An important ingredient of the phenomenological analysis developed in this thesis is the coupling of the X_{17} boson to electrons (g_e), appearing in a low-energy Lagrangian as

$$\mathcal{L} \supset g_e X \bar{e} e. \quad (1.13)$$

The ATOMKI experiment, however, does not provide a direct measurement of g_e . The observable signal at ATOMKI arises from nuclear transitions of the form $p + \text{Target} \rightarrow N^* \rightarrow N + e^+ e^-$, where $N = {}^8\text{Be}, {}^4\text{He}, {}^{12}\text{C}$. If the $e^+ e^-$ pair originates from the decay of an on-shell intermediate boson X_{17} , the measured signal rate is proportional to

$$\text{Signal Rate} \propto \sigma(p + \text{Target} \rightarrow N^*) \text{BR}(X_{17} \rightarrow e^+ e^-). \quad (1.14)$$

As a consequence, the experimental sensitivity is only to the branching ratio of the decay into electron-positron pairs, and not to the electron coupling itself. Under the assumption that X_{17} decays exclusively into $e^+ e^-$, one has $\text{BR}(X_{17} \rightarrow e^+ e^-) \simeq 1$, and the explicit dependence on g_e is lost.

An independent probe of the X_{17} hypothesis is provided by the PADME experiment. PADME is a fixed-target experiment in which a positron beam impinges on a thin diamond target. In this setup, new light bosons can be searched for through their direct production in purely leptonic processes. Unlike nuclear experiments, this approach does not rely on nuclear transitions and provides direct sensitivity to the coupling of X_{17} to electrons.

By varying the energy of the incident positron beam, PADME has scanned the center-of-mass energy range $14 \lesssim \sqrt{s} \lesssim 23$ MeV. This interval includes the region around $\sqrt{s} \simeq 17$ MeV, where the production of an X_{17} boson is expected. Within this energy window, PADME has reported a mild excess in the $e^+ e^-$ channel corresponding to an invariant mass around $m_X \simeq 16.90$ MeV. While the statistical significance of this fluctuation is limited, it is compatible with the mass scale suggested by the ATOMKI anomalies. Interpreting this excess under the assumption that X is a vector mediator, PADME performed a fit to the data and extracted a preferred value for the electron coupling, $g_e \simeq 5.6 \times 10^{-4}$. This result provides an additional, purely leptonic indication that is consistent with the X_{17} hypothesis and complements the constraints derived from nuclear transitions.

This overview sets the stage for the theoretical framework developed in the following chapter, where the X_{17} boson will be embedded into a consistent particle-physics model and its implications for DM phenomenology will be explored. We also highlight that in cap 4 we will place our results in a broader context by reviewing the comprehensive analysis of ref. [14] and by comparing them with a wide set of laboratory constraints on light bosons coupled to electrons.

Before moving to the next chapter, it is worth noting that possible connections between X_{17} and the dark sector have already been explored in the literature. For instance, in Refs. [15, 16] X_{17} is interpreted as a dark photon and its role as a portal between DM and the SM sector is analyzed in detail. The work in this thesis, however, is highly different from this set-up for two main reasons: *i*) we will explicitly consider X_{17} as a scalar boson; *ii*) we will not forbid direct interactions among SM, DM and the X_{17} . The second item implies, as we will see, that particular care will be devoted to ensuring the requirement of stability of the DM in our framework.

Chapter 2

Theoretical Framework Of Our Model

Here begins the original contribution of this thesis. In this chapter we will introduce the theoretical setup that will be used throughout the rest of the thesis. Starting from the SM field content and gauge symmetries, we will explore the possibility that X_{17} -boson may mediate interactions between SM and DM particles. We define the relevant interaction Lagrangian, discuss the assumptions underlying the effective description, and identify the couplings that will control the phenomenology studied in the following chapters.

The dark sector is assumed to be minimal and consists of a real scalar field X and a fermionic vector-like DM particle χ . While our original motivation arises from anomalies observed at an energy of approximately 17 MeV, we will present results for a generic mediator X with mass m_X , allowing our analysis to extend beyond the specific X_{17} case.

In addition, we extend the SM leptonic sector by introducing a right-handed Majorana neutrino ν_R , singlet under the SM gauge group. The DM particle χ is taken to be a Majorana right-handed fermion, and can either coincide with ν_R or represent an independent field.

In this chapter we construct the effective interaction Lagrangian describing the couplings beyond the SM introduced by the new degrees of freedom. Working in an effective field theory framework, we classify all gauge-invariant operators under the SM gauge group $SU(3)_C \times SU(2)_L \times U(1)_Y$ up to dimension six. The resulting operator basis is shown in Tables 2.1–2.4 and provides the starting point for the diagrammatic analysis carried out in Sec. 2.2.

2.1 The Effective Interaction Lagrangian

In this section we aim at building up a minimal model, characterized by two key interactions involving the new mediator X . The first is a coupling of X to electrons, motivated directly by the experimental anomalies observed at PADME and associated with the X_{17} hypothesis; the second is a coupling of X to DM. In this way, the same mediator can interact with SM particles only, with both SM and DM particles or, finally, with only DM (in this last case, X can be thus thought as a portal to the dark sector). Additional interactions, such as the coupling to neutrinos or to the

Higgs-boson, appear as natural byproducts of gauge invariance, and will be treated with care. In particular, we must ensure that they do not introduce additional couplings between DM and other SM fields, which may spoil DM stability.

We focus now on the interaction with the electrons (and positrons). At low energies, this interaction can be parametrized in a model-independent way as

$$\mathcal{L}_{X,e}^{\text{SM}} = g_e (\bar{e} \Gamma_X e) X + \dots, \quad (2.1)$$

where, in general, $\Gamma_X = 1, \gamma^5$ or $\gamma^\mu, \gamma^\mu \gamma^5$ depending on whether X is a scalar, pseudoscalar or (axial-)vector state. Pure vector couplings are strongly disfavoured by current data [14].

We now turn to the coupling between X and DM. At low energies, this interaction can be parametrized as

$$\mathcal{L}_{X,\chi}^{\text{DM}} = g_\chi (\bar{\chi} \Gamma_\chi \chi) X + \dots, \quad (2.2)$$

where χ is a SM-singlet fermion and Γ_χ denotes the Lorentz structure of the coupling.

In addition to the electron and DM couplings, an interaction of X with neutrinos is also phenomenologically interesting and arises naturally in our setup. At low energies, a generic coupling to SM neutrinos and DM takes the form:

$$\mathcal{L}_{X,\chi,\nu}^{\text{DM}} = g_{\chi\nu} (\bar{\chi} \Gamma_{\chi\nu} \nu) X + \dots. \quad (2.3)$$

Our goal for this section is, then, to derive the set of operators that are invariant under the SM gauge group $SU(3)_C \times SU(2)_L \times U(1)_Y$ and that reproduce the low-energy couplings of X_{17} to electrons as in eq.(2.1), as well as its interactions with the rest of the visible and dark sectors, see eqs. (2.2-2.3).

2.1.1 Gauge-invariant Interactions Classification

We collect all the allowed operators in four tables. The first two, Tables 2.1 and 2.2, correspond to the case in which X is a scalar (0^{++}), while Tables 2.3 and 2.4 correspond to the pseudoscalar case (0^{+-}). Tables 2.1 and 2.3 describe the scenario in which the right-handed neutrino ν_R and the dark fermion χ are independent fields ($\chi \neq \nu_R$), whereas Tables 2.2 and 2.4 refer to the case in which they coincide and χ plays the role of a Majorana right-handed neutrino ($\chi = \nu_R$).

The first two columns of each of the four Tables specify the gauge quantum numbers of X and of the dark fermion χ under the SM gauge group. We adopt the compact notation

$$(d_{SU(3)}, d_{SU(2)}, Y)$$

to denote the dimensions of the representation under $SU(3)_C$, $SU(2)_L$ and the hypercharge Y under $U(1)_Y$.¹ Thus, it is clear that each row in the Tables corresponds to a different theoretical model.

¹We always take both X and χ to be color-singlets, i.e. $d_{SU(3)} = 1$. Allowing them to transform non-trivially under $SU(3)_C$ would lead to a much richer (and more constrained) phenomenology, which lies beyond the scope of this thesis.

All the remaining columns of Tables 2.1-2.4 show the new interactions beyond the SM that are allowed for each choice of gauge quantum numbers. They are grouped according to their field content.

The terms collected under $\mathcal{L}_{X,\phi}^{\text{SM}}$, with $\phi \in \{e, H, B_\mu, W_\mu^a\}$, are couplings of X to SM fields. In particular, they include the interactions with electrons and positrons, as well as couplings to the Higgs doublet and to the electroweak gauge bosons, which in turn may induce interactions with photons after electroweak symmetry breaking. All such couplings of X with the SM are allowed by gauge invariance. However, for the purposes of this Thesis, it is sufficient to focus only on $\mathcal{L}_{X,e}^{\text{SM}}$ hereafter.

The last two columns, labeled $\mathcal{L}_X^{\text{DM}}$ and $\mathcal{L}_{X,SM}^{\text{DM}}$, contain instead the interactions involving the dark fermion χ . The operators in $\mathcal{L}_X^{\text{DM}}$ describe the desired portal couplings between χ and X , which, as we will see in chapter 3, are responsible for production of DM in the early Universe. On the contrary, the terms in $\mathcal{L}_{X,SM}^{\text{DM}}$ involve both DM and SM fields, and may or may not contain an explicit X . After electroweak symmetry breaking, these operators might induce effective direct couplings between DM and SM fields that are not purely mediated by the exchange of X . In particular, such terms can endanger the DM role of χ (for instance by inducing fast decays). For this reason, the operators in $\mathcal{L}_{X,SM}^{\text{DM}}$ must be treated with care.

It is worth emphasize on some final comments regarding the tables:

- Note that an $SU(2)_L$ doublet field contains one electrically neutral component regardless of whether its hypercharge is $+\frac{1}{2}$ or $-\frac{1}{2}$. This applies both to X and to χ . Since the interactions that appear in the Lagrangian are essentially the same in both cases, up to the use of a conjugated doublet (e.g., \tilde{X} instead of X), we chose not to explicitly list the multiplicity of hypercharge assignments in the table for clarity.

It is worth stressing, however, that whenever either X or χ is embedded in an $SU(2)_L$ doublet, the spectrum necessarily contains additional electrically charged partners. As a consequence, such model realizations entail the presence of extra degrees of freedom beyond the neutral state responsible for the observed anomalies or for the DM phenomenology. This introduces the additional theoretical and phenomenological requirement of accounting for the effects induced by these charged states, and of ensuring their consistency with existing experimental constraints.

- In the cases where $X \sim (1, 2, 1/2)$, the field shares the same quantum numbers as the SM Higgs doublet. As a result, terms involving combinations or permutations of X and H in operators containing both fields are, in principle, allowed by gauge invariance. However, these additional terms have not been explicitly listed in the table for simplicity.
- Finally, we stress that all operators with mass dimension $d > 4$ in tables 2.1–2.4 are written in an Effective Field Theory (EFT) form. A generic operator \mathcal{O}_d of dimension d appears in the Lagrangian as $c_d/\Lambda^{d-4} \mathcal{O}_d$, so that higher-dimensional interactions are suppressed by inverse

| $X(0^{++})$ | $\chi \neq \nu_R$ | $\mathcal{L}_{X,e}^{\text{SM}}$ | $\mathcal{L}_{X,H}^{\text{SM}}$ | $\mathcal{L}_{X,B}^{\text{SM}}$ | $\mathcal{L}_{X,W}^{\text{SM}}$ | $\mathcal{L}_X^{\text{DM}}$ | $\mathcal{L}_{X,SM}^{\text{DM}}$ |
|-----------------------|-----------------------|---|---|---|--|--|---|
| (1,1,0) | (1,1,0) | $\frac{1}{\Lambda} X \bar{\ell} H e_R$ | $XXH^\dagger H$ $\lambda X H^\dagger H$ | $\frac{1}{\Lambda} X B_{\mu\nu} B^{\mu\nu}$ | $\frac{1}{\Lambda} X W_{\mu\nu}^a W^{a\mu\nu}$ | $\bar{\chi} \chi X$ $\bar{\chi}_L \nu_R X$ $\bar{\nu}_R^c \nu_R X$ $X \bar{\chi}_L \nu_R$ | $y \bar{\ell} \tilde{H} \chi_R$ $\lambda \bar{\chi}_L \nu_R$ $\frac{1}{\Lambda} X \bar{\ell} \tilde{H} \chi_R$ $X \bar{\chi}_L \nu_R$ |
| (1,1,0) | (1,2, $\frac{1}{2}$) | $\frac{1}{\Lambda} X \bar{\ell} H e_R$ | $XXH^\dagger H$ $\lambda X H^\dagger H$ | $\frac{1}{\Lambda} X B_{\mu\nu} B^{\mu\nu}$ | $\frac{1}{\Lambda} X W_{\mu\nu}^a W^{a\mu\nu}$ | $\bar{\chi} \chi X$ | $\bar{\chi}_L H \nu_R$ $X \bar{\ell} \chi_L^c$ $\lambda \bar{\ell} \chi_L^c$ $\frac{1}{\Lambda} X \bar{\chi}_L H \nu_R$ |
| (1,2, $\frac{1}{2}$) | (1,1,0) | $\bar{\ell} X e_R$ $\frac{1}{\Lambda} (\bar{\ell} X) (H^\dagger \ell)$ | $(H^\dagger H)(X^\dagger X)$ $\lambda^2 H^\dagger X$ | $\frac{1}{\Lambda^2} (X^\dagger H) B_{\mu\nu} B^{\mu\nu}$ $\frac{1}{\Lambda^2} (X^\dagger \frac{\sigma_a}{2} H) W_{\mu\nu}^a B^{\mu\nu}$ | $\frac{1}{\Lambda^2} (X^\dagger H) W_{\mu\nu}^a W^{a\mu\nu}$ $\frac{1}{\Lambda^2} (X^\dagger \frac{\sigma_a}{2} H) W_{\mu\nu}^a B^{\mu\nu}$ | $\frac{1}{\Lambda} X^\dagger H \bar{\chi} \chi$ $\frac{1}{\Lambda} X^\dagger H \bar{\chi}_L \nu_R$ $\frac{1}{\Lambda} X^\dagger H \bar{\nu}_R^c \nu_R$ $\frac{1}{\Lambda} X^\dagger H \bar{\chi}_L \nu_R$ | $\bar{\ell} \tilde{H} \chi_R$ $\bar{\ell} \tilde{X} \chi_R$ $\lambda \bar{\chi}_L \nu_R$ $\frac{1}{\Lambda} X^\dagger H \bar{\chi}_L \nu_R$ |
| (1,2, $\frac{1}{2}$) | (1,2, $\frac{1}{2}$) | $\bar{\ell} X e_R$ $\frac{1}{\Lambda} (\bar{\ell} X) (H^\dagger \ell)$ | $(H^\dagger H)(X^\dagger X)$ $\lambda^2 H^\dagger X$ | $\frac{1}{\Lambda^2} (X^\dagger H) B_{\mu\nu} B^{\mu\nu}$ $\frac{1}{\Lambda^2} (X^\dagger \frac{\sigma_a}{2} H) W_{\mu\nu}^a B^{\mu\nu}$ | $\frac{1}{\Lambda^2} (X^\dagger H) W_{\mu\nu}^a W^{a\mu\nu}$ $\frac{1}{\Lambda^2} (X^\dagger \frac{\sigma_a}{2} H) W_{\mu\nu}^a B^{\mu\nu}$ | $\bar{\chi}_L X \nu_R$ $\frac{1}{\Lambda} \bar{\chi} \chi X^\dagger H$ | $\frac{1}{\Lambda} \bar{\ell} \chi_R X^\dagger \tilde{H}$ $\bar{\chi}_L H \nu_R$ $\lambda \bar{\ell} \chi_L^c$ $\frac{1}{\Lambda} X^\dagger H \bar{\ell} \chi_L^c$ |

Table 2.1 Gauge quantum numbers and effective operators for a scalar mediator $X(0^{++})$ in the case $\chi \neq \nu_R$. The first two columns specify the $(d_{SU(3)}, d_{SU(2)}, Y)$ assignments of X and of the dark fermion χ . The columns $\mathcal{L}_{X,\phi}^{\text{SM}}$ collect the gauge-invariant couplings of X to SM fields ϕ , while $\mathcal{L}_X^{\text{DM}}$ and $\mathcal{L}_{X,SM}^{\text{DM}}$ contain, respectively, portal interactions involving X and χ , and additional operators with both χ and SM fields.

powers of the heavy scale Λ . In other words, the larger the operator dimension, the more strongly its contribution is suppressed at energies well below Λ . We also note that, differently from the EFT operators discussed above, the parameter λ denotes a genuine dimensionful coupling, it appears in operators of mass dimension $d = 3$ and $d = 2$.

- In the tables, χ_L and χ_R denote the left- and right-handed components of the fermion field χ , defined through the chiral projection operators

$$\chi_{L,R} \equiv P_{L,R} \chi, \quad P_{L,R} = \frac{1}{2} (1 \mp \gamma^5). \quad (2.4)$$

And σ_a are the pauli matrices.

Having now listed our operators in full detail, we can directly examine the terms in the last columns, which are the ones that could potentially jeopardize the stability of χ by inducing fast decay channels.

| $X(0^{++})$ | $\chi = \nu_R$ | $\mathcal{L}_{X,e}^{\text{SM}}$ | $\mathcal{L}_{X,H}^{\text{SM}}$ | $\mathcal{L}_{X,B}^{\text{SM}}$ | $\mathcal{L}_{X,W}^{\text{SM}}$ | $\mathcal{L}_X^{\text{DM}}$ | $\mathcal{L}_{X,SM}^{\text{DM}}$ |
|-----------------------|----------------|---|---|---|--|---|--|
| (1,1,0) | (1,1,0) | $\frac{1}{\Lambda} X \bar{\ell} H e_R$ | $XXH^\dagger H$ $\lambda X H^\dagger H$ | $\frac{1}{\Lambda} X B_{\mu\nu} B^{\mu\nu}$ | $\frac{1}{\Lambda} X W_{\mu\nu}^a W^{a\mu\nu}$ | $\bar{\chi}^c \chi X$ | $y \bar{\ell} \tilde{H} \chi$ $\frac{1}{\Lambda} X \bar{\ell} \tilde{H} \chi$ |
| (1,2, $\frac{1}{2}$) | (1,1,0) | $\bar{\ell} X e_R$ $\frac{1}{\Lambda} (\bar{\ell} X) (H^\dagger \ell)$ | $(H^\dagger H)(X^\dagger X)$ $\lambda^2 H^\dagger X$ | $\frac{1}{\Lambda^2} (X^\dagger H) B_{\mu\nu} B^{\mu\nu}$ | $\frac{1}{\Lambda^2} (X^\dagger H) W_{\mu\nu}^a W^{a\mu\nu}$ $\frac{1}{\Lambda^2} (X^\dagger \frac{\sigma_a}{2} H) W_{\mu\nu}^a B^{\mu\nu}$ | $\frac{1}{\Lambda} X^\dagger H \bar{\chi}^c \chi$ | $\bar{\ell} \tilde{H} \chi$ $\bar{\ell} \tilde{X} \chi$ |

Table 2.2 Same as tab. 2.1, but for the case in which the dark fermion coincides with the right-handed neutrino, $\chi = \nu_R$, so that only one singlet fermion appears in the dark sector.

Schematically, the operators in $\mathcal{L}_{X,SM}^{\text{DM}}$ fall into two classes: mixing terms between χ and ν , and interaction terms of the type $\chi \nu_R X$ (or the ones involving the SM neutrino, such as $\bar{\ell} \tilde{H} \chi$). These interactions can, indeed, induce DM decays into SM states, potentially ruling out χ as a viable DM candidate. We will return to this issue in the appendix A.

In what follows we will adopt as benchmark scenario the minimal configuration corresponding to the first row of tab. 2.2, in which the mediator is a real scalar $X_{17}(0^{++}) \sim (1, 1, 0)$ and the dark fermion coincides with a single right-handed Majorana neutrino, $\chi = \nu_R \sim (1, 1, 0)$. This set-up is, in fact, the one which already captures all the ingredients relevant for our analysis: a coupling of X_{17} to electrons, a portal coupling to DM, and the minimal set of additional interactions implied by gauge invariance, without introducing extra degrees of freedom in addition to X and χ .

2.1.2 Model Limitations and Future Extensions

Before proceeding to the detailed calculations, it is useful to highlight three non-trivial features of our model. First, in the present work, we omit quark operators in order to keep our model (e.g. Tables 2.1–2.4) as minimal as possible and to focus exclusively on the electron excess observed at PADME. Couplings of an X_{17} -like mediator to quarks are, however, not forbidden by any fundamental principle; on the contrary, they are expected to play a role in a complete description of the ATOMKI anomalies discussed in Chapter 1, which originate from nuclear transitions. A more comprehensive analysis that incorporates quark couplings may be developed in future extensions of this framework.

Another relevant aspect of our model concerns its flavour structure. In the discussion above, we have treated ν_R (and, when applicable, χ) as a single right-handed Majorana state. In a more realistic setup, one would promote this field to a flavour multiplet, for example a triplet of right-handed neutrinos, in order to account for the observed pattern of light neutrino masses and mixings via a seesaw-like mechanism. Such an extension would generically induce additional couplings of X_{17} to muons and taus, as well as a non-trivial flavour structure within the dark sector. While technically straightforward, this generalization would introduce an additional complexity that is largely orthogonal to the questions addressed in this thesis. For this reason, we keep the flavour structure as minimal as possible and restrict ourselves to a single effective right-handed state.

Finally, the available experimental data do not allow for a definitive determination of the spin of

| $X(0^{+-})$ | $\chi \neq \nu_R$ | $\mathcal{L}_{X,e}^{\text{SM}}$ | $\mathcal{L}_{X,H}^{\text{SM}}$ | $\mathcal{L}_{X,B}^{\text{SM}}$ | $\mathcal{L}_{X,W}^{\text{SM}}$ | $\mathcal{L}_X^{\text{DM}}$ | $\mathcal{L}_{X,SM}^{\text{DM}}$ |
|-----------------------|-----------------------|--|---------------------------------|---|--|--|---|
| (1,1,0) | (1,1,0) | $\frac{1}{\Lambda} i X \bar{\ell} H e_R$ | $XXH^\dagger H$ | $\frac{1}{\Lambda} X B_{\mu\nu} \tilde{B}^{\mu\nu}$ | $\frac{1}{\Lambda} X W_{\mu\nu}^a \tilde{W}^{a\mu\nu}$ | $i \bar{\chi} \chi X$ $i \bar{\chi}_L \nu_R X$ $i \bar{\nu}_R^c \nu_R X$ $i X \bar{\chi}_L \nu_R$ | $y \bar{\ell} \tilde{H} \chi_R$ $\lambda \bar{\chi}_L \nu_R$ $\frac{1}{\Lambda} i X \bar{\ell} \tilde{H} \chi_R$ $i X \bar{\chi}_L \nu_R$ |
| (1,1,0) | (1,2, $\frac{1}{2}$) | $\frac{1}{\Lambda} i X \bar{\ell} H e_R$ | $XXH^\dagger H$ | $\frac{1}{\Lambda} X B_{\mu\nu} \tilde{B}^{\mu\nu}$ | $\frac{1}{\Lambda} X W_{\mu\nu}^a \tilde{W}^{a\mu\nu}$ | $i \bar{\chi} \chi X$ | $\bar{\chi}_L H \nu_R$ $\lambda \bar{\ell} \chi_L^c$ $i X \bar{\ell} \chi_L^c$ $\frac{1}{\Lambda} i X \bar{\chi}_L H \nu_R$ |
| (1,2, $\frac{1}{2}$) | (1,1,0) | $i \bar{\ell} X e_R$ | $(H^\dagger H)(X^\dagger X)$ | $\frac{1}{\Lambda^2} (X^\dagger H) B_{\mu\nu} \tilde{B}^{\mu\nu}$ $\frac{1}{\Lambda^2} (X^\dagger \frac{\sigma_a}{2} H) W_{\mu\nu}^a \tilde{B}^{\mu\nu}$ | $\frac{1}{\Lambda^2} (X^\dagger H) W_{\mu\nu}^a \tilde{W}^{a\mu\nu}$ $\frac{1}{\Lambda^2} (X^\dagger \frac{\sigma_a}{2} H) W_{\mu\nu}^a \tilde{B}^{\mu\nu}$ | $\frac{1}{\Lambda} i X^\dagger H \bar{\chi} \chi$ $\frac{1}{\Lambda} i X^\dagger H \bar{\chi}_L \nu_R$ $\frac{1}{\Lambda} i X^\dagger H \bar{\nu}_R^c \nu_R$ $\frac{1}{\Lambda} i X^\dagger H \bar{\chi}_L \nu_R$ | $\bar{\ell} \tilde{H} \chi_R$ $\lambda \bar{\chi}_L \nu_R$ $i \bar{\ell} \tilde{X} \chi_R$ $\frac{1}{\Lambda} i X^\dagger H \bar{\chi}_L \nu_R$ |
| (1,2, $\frac{1}{2}$) | (1,2, $\frac{1}{2}$) | $i \bar{\ell} X e_R$ | $(H^\dagger H)(X^\dagger X)$ | $\frac{1}{\Lambda^2} (X^\dagger H) B_{\mu\nu} \tilde{B}^{\mu\nu}$ $\frac{1}{\Lambda^2} (X^\dagger \frac{\sigma_a}{2} H) W_{\mu\nu}^a \tilde{B}^{\mu\nu}$ | $\frac{1}{\Lambda^2} (X^\dagger H) W_{\mu\nu}^a \tilde{W}^{a\mu\nu}$ $\frac{1}{\Lambda^2} (X^\dagger \frac{\sigma_a}{2} H) W_{\mu\nu}^a \tilde{B}^{\mu\nu}$ | $i \bar{\chi}_L X \nu_R$ $\frac{1}{\Lambda} i \bar{\chi} \chi X^\dagger H$ | $\frac{1}{\Lambda} i \bar{\ell} \chi_R X^\dagger \tilde{H}$ $\bar{\chi}_L H \nu_R$ $\lambda \bar{\ell} \chi_L^c$ $\frac{1}{\Lambda} X^\dagger H \bar{\ell} \chi_L^c$ |

Table 2.3 Gauge quantum numbers and effective operators for a pseudoscalar mediator $X(0^{+-})$ in the case $\chi \neq \nu_R$. The structure of the table is analogous to tab. 2.1, with some replacements in structures induced by the pseudoscalar nature of X appropriate to a pseudoscalar coupling (e.g. i terms and dual field strengths $\tilde{B}_{\mu\nu}$, $\tilde{W}_{\mu\nu}^a$).

the X_{17} . In the tables, we restricted our analysis to the simpler case of a (pseudo)scalar mediator. As discussed in sec. 1.3, recent analyses in [13] of the experimental anomalies associated with the ATOMKI measurements indicate that a scalar, CP-even interpretation of the new particle is currently favored, once theoretical uncertainties and nuclear-structure effects are properly taken into account. In the near future, however, PADME runs will probe the possible coupling of the X_{17} mediator to photons with significantly sensitivity, providing then a direct information on its spin. Indeed, according to the Landau–Yang theorem [17, 18], a massive spin-1 particle cannot decay into two photons. Therefore, the information of the $X_{17} \rightarrow \gamma\gamma$ decay would favor or not a scalar interpretation of X_{17} .

| $X(0^{+-})$ | $\chi = \nu_R$ | $\mathcal{L}_{X,e}^{\text{SM}}$ | $\mathcal{L}_{X,H}^{\text{SM}}$ | $\mathcal{L}_{X,B}^{\text{SM}}$ | $\mathcal{L}_{X,W}^{\text{SM}}$ | $\mathcal{L}_X^{\text{DM}}$ | $\mathcal{L}_{X,SM}^{\text{DM}}$ |
|-----------------------|----------------|--|---------------------------------|---|--|---|--|
| (1,1,0) | (1,1,0) | $\frac{1}{\Lambda} i X \bar{\ell} H e_R$ | $X X H^\dagger H$ | $\frac{1}{\Lambda} X B_{\mu\nu} \tilde{B}^{\mu\nu}$ | $\frac{1}{\Lambda} X W_{\mu\nu}^a \tilde{W}^{a\mu\nu}$ | $i \bar{\chi}^c \chi X$ | $y \bar{\ell} \tilde{H} \chi$ |
| (1,2, $\frac{1}{2}$) | (1,1,0) | $i \bar{\ell} X e_R$ | $(H^\dagger H)(X^\dagger X)$ | $\frac{1}{\Lambda^2} (X^\dagger H) B_{\mu\nu} \tilde{B}^{\mu\nu}$ | $\frac{1}{\Lambda^2} (X^\dagger H) W_{\mu\nu}^a \tilde{W}^{a\mu\nu}$ $\frac{1}{\Lambda^2} (X^\dagger \frac{\sigma_a}{2} H) W_{\mu\nu}^a \tilde{B}^{\mu\nu}$ | $\frac{1}{\Lambda} i X^\dagger H \bar{\chi}^c \chi$ | $\bar{\ell} \tilde{H} \chi$ $i \bar{\ell} \tilde{X} \chi$ |

Table 2.4 Same as tab. 2.3, but for the case $\chi = \nu_R$, where the dark fermion is identified with the right-handed neutrino.

2.2 Relic Abundance Calculation: Diagram Evaluation

In the previous section we classified all the effective operators allowed by gauge invariance and identified a minimal benchmark scenario, corresponding to the first row of tab. 2.2.

In this section we move from the operator level to the evaluation of the corresponding Feynman diagrams. First, we extract the Feynman rules starting from the Lagrangian terms discussed in the previous section and, then, we compute the squared amplitudes for the decay and scattering processes of interest, such as $X \rightarrow \chi\chi$ and $e^+e^- \rightarrow \chi\chi$, which will be relevant for the computations in chapter 3. We recall that the total Lagrangian is given by

$$\mathcal{L}_{\text{tot}} = \mathcal{L}_{\text{SM}} + \mathcal{L}_{\text{DS}}. \quad (2.5)$$

Here, \mathcal{L}_{DS} is the dark sector Lagrangian

$$\begin{aligned} \mathcal{L}_{\text{DS}} \equiv & \frac{1}{2} (\partial_\mu X) (\partial^\mu X) - \frac{1}{2} m_X^2 X^2 - \frac{1}{3} \kappa_X X^3 - \frac{1}{4} \lambda_X X^4 + \frac{1}{2} \bar{\chi} i \not{D} \chi - \frac{1}{2} \hat{m} \bar{\chi}^c \chi \\ & - \frac{g_{Xee}}{\Lambda} X \bar{\ell} H e_R + g_{XDM} X \bar{\chi}^c \chi - y_{mix} \bar{\ell} \tilde{H} \chi - \frac{g_{XDM\nu}}{\Lambda} X \bar{\ell} \tilde{H} \chi \\ & - g_H X X H^\dagger H - \tilde{g}_H X H^\dagger H - \frac{g_{XBB}}{\Lambda} X B_{\mu\nu} B^{\mu\nu} - \frac{g_{XWW}}{\Lambda} X W_{\mu\nu}^a W^{a\mu\nu} + \text{h.c.} . \end{aligned} \quad (2.6)$$

In what follows we will retain only the interaction terms that are directly relevant for the phenomenology discussed in this thesis, namely

$$\mathcal{L}_{\text{int}} \equiv \frac{g_{Xee}}{\Lambda} X \bar{\ell} H e_R + g_{XDM} X \bar{\chi}^c \chi + y_{mix} \bar{\ell} \tilde{H} \chi + \frac{\hat{g}_{XDM\nu}}{\Lambda} X \bar{\ell} \tilde{H} \chi + \text{h.c.} . \quad (2.7)$$

After electroweak symmetry breaking and working in the unitary gauge, i.e.

$$H = \begin{pmatrix} 0 \\ \frac{v_h + h}{\sqrt{2}} \end{pmatrix}, \quad \tilde{H} = \begin{pmatrix} \frac{v_h + h}{\sqrt{2}} \\ 0 \end{pmatrix}, \quad \ell = \begin{pmatrix} \nu_L \\ e_L \end{pmatrix}, \quad (2.8)$$

where v_h is the Higgs vacuum expectation value, defined in sec. 1.1, and h is the physical Higgs field, the interaction Lagrangian becomes:

$$\mathcal{L}_{\text{int}}^{\text{EWSB}} = -\frac{v_h}{\sqrt{2}} \frac{g_{Xee}}{\Lambda} X \bar{e}_L e_R - g_{XDM} X \bar{\chi}^c \chi - y_{mix} \frac{v_h}{\sqrt{2}} \bar{\nu}_L \chi - \frac{v_h}{\sqrt{2}} \frac{\hat{g}_{XDM\nu}}{\Lambda} X \bar{\nu}_L \chi + \text{h.c.} , \quad (2.9)$$

(2.9) contains explicit couplings of X to electrons and neutrinos, as well as mass and mixing terms for the dark fermion χ .

It is convenient to parametrize the mixing between the active neutrino and the dark fermion in terms of a small dimensionless mixing angle θ , defined as

$$\theta \equiv \frac{y_{\text{mix}} v_h}{\sqrt{2} m_\chi}. \quad (2.10)$$

For later convenience it is also useful to rewrite the interaction terms in terms of effective low-energy couplings. We therefore define:

$$\begin{aligned} g_e &\equiv \frac{v_h}{\sqrt{2}\Lambda} g_{Xee}, \\ g_\nu &\equiv \frac{v_h}{\sqrt{2}\Lambda} g_{XDM\nu}, \\ g_\chi &\equiv 2 g_{XDM}, \end{aligned} \quad (2.11)$$

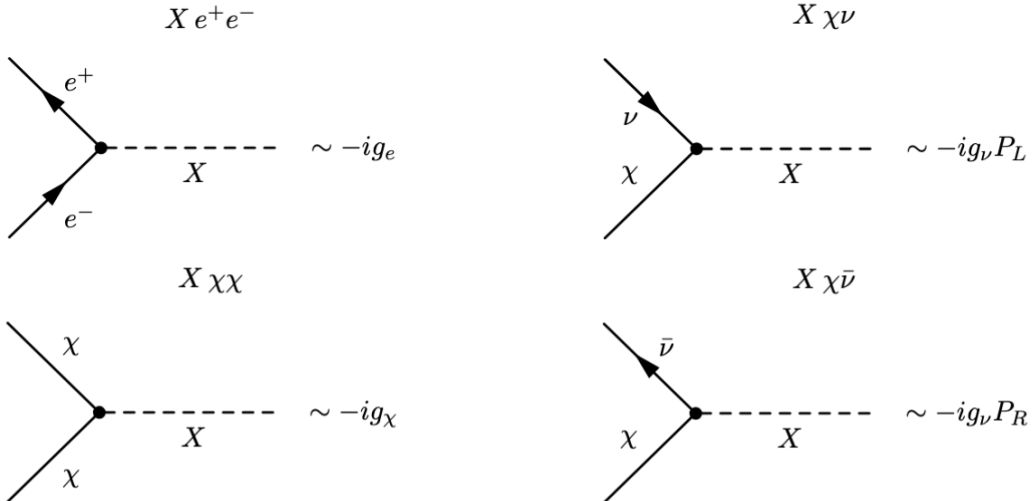
so that g_e and g_ν directly parametrise the strength of the $X\bar{e}e$ and $X\bar{\chi}\nu$ vertices after EWSB, while the extra factor of 2 in g_χ accounts for the Majorana nature of χ in the $X\chi\chi$ vertex. These effective parameters g_e , g_ν and g_χ are precisely the low-energy couplings that appeared earlier in the interactions (2.1)–(2.3).

The interaction Lagrangian relevant for our analysis can be re-written in terms of such effective couplings (g_e , g_ν , g_χ) as

$$\mathcal{L}_{\text{int}}^{\text{EWSB}} = -g_e X \bar{e}_L e_R - \frac{g_\chi}{2} X \bar{\chi}^c \chi - g_\nu X \bar{\nu}_L \chi + \text{h.c.} \quad (2.12)$$

As anticipated in the previous section, after electroweak symmetry breaking the Lagrangian is effectively controlled by the two couplings we are interested in, namely g_e and g_χ . At the same time, one additional interaction involving neutrinos, proportional to g_ν , is still present. As previously mentioned, this "unwanted" term may destabilize χ , and therefore require a dedicated discussion in appendix A.

Starting from the interaction Lagrangian in eq. (2.12), the corresponding Feynman rules read:



We then compute explicitly the squared amplitudes for the processes relevant for our computations of the DM production, as it will be discussed in the next chapter. Below, we list the squared moduli of the amplitudes, summed over all initial and final state polarisations (and *not* averaged over the initial state polarisations):

$$\sum_{\text{pol}} |\mathcal{A}(X \rightarrow \chi\chi)|^2 = 2 g_\chi^2 (m_X^2 - 4m_\chi^2), \quad (2.13)$$

$$\sum_{\text{pol}} |\mathcal{A}(X \rightarrow \chi\nu)|^2 = g_\nu^2 (m_X^2 - m_\chi^2 - m_\nu^2), \quad (2.14)$$

$$\sum_{\text{pol}} |\mathcal{A}(e^+e^- \rightarrow \chi\nu)|^2 = \frac{2 g_\nu^2 g_e^2 (s - 4m_e^2) (s - m_\chi^2 - m_\nu^2)}{(m_X^2 - s)^2}, \quad (2.15)$$

$$\sum_{\text{pol}} |\mathcal{A}(e^+e^- \rightarrow \chi\chi)|^2 = \frac{4 g_\chi^2 g_e^2 (s - 4m_e^2) (s - 4m_\chi^2)}{(m_X^2 - s)^2}. \quad (2.16)$$

The last two amplitudes arise from the following diagrams:



The inclusion of the finite width of the mediator in the s -channel propagator brings to the modification

$$(m_X^2 - s) \rightarrow (m_X^2 - s + i m_X \Gamma_X),$$

so that the last two expressions become

$$\sum_{\text{pol}} |\mathcal{A}(e^+e^- \rightarrow \chi\nu)|^2 = \frac{2 g_\nu^2 g_e^2 (s - 4m_e^2) (s - m_\chi^2 - m_\nu^2)}{(m_X^2 - s)^2 + m_X^2 \Gamma_X^2}, \quad (2.17)$$

$$\sum_{\text{pol}} |\mathcal{A}(e^+e^- \rightarrow \chi\chi)|^2 = \frac{4 g_\chi^2 g_e^2 (s - 4m_e^2) (s - 4m_\chi^2)}{(m_X^2 - s)^2 + m_X^2 \Gamma_X^2}. \quad (2.18)$$

Before concluding, we stress two considerations:

- We have not listed *all* possible processes involving the dark fermion χ , but only those that are relevant for our purposes. In view of the DM-production related calculation in chapter 3, the amplitudes above are precisely the ones for which the number of DM particles differs between the initial and final states at least by one unit.

- During the rest of this thesis, we will effectively neglect the X -mediated interactions between χ and active neutrinos, since they are expected to be phenomenologically suppressed for several independent reasons.
 - (i) Couplings involving neutrinos generically open decay channels of the form $\chi \rightarrow \nu + \dots$. Requiring DM to be stable on cosmological time scales therefore strongly suppresses such interactions.
 - (ii) Neutrino couplings typically lead to enhanced annihilation or decay channels producing high-energy neutrinos. Existing indirect detection searches place stringent bounds on these processes, making sizable neutrino couplings disfavored.
 - (iii) Interactions involving neutrinos can generate monochromatic or sharply peaked neutrino signals. The absence of observed neutrino lines in current experiments further constrains these couplings.

For similar reasons, we also neglect the effects induced by active-sterile mixing between χ and the SM neutrinos. In summary, the active-sterile mixing angle θ defined in eq. 2.10 is forced to be very small by three independent considerations.

- (i) The correction to the light neutrino mass induced by the seesaw-like structure, $\Delta m_\nu \simeq \theta^2 m_\chi$, must satisfy the cosmological bound on $\sum_\nu m_\nu$.
- (ii) DM stability on cosmological time-scales requires the total decay rate induced by the mixing to be much smaller than T_U^{-1} .
- (iii) Radiative decays $\chi \rightarrow \nu\gamma$ are additionally constrained by X-ray observations, which demand an extremely long lifetime for this specific channel.

A more detailed discussion of the suppression mechanisms associated with neutrino couplings is deferred to the app. A.

In this chapter we have constructed a theoretical framework linking a light scalar mediator X to a fermionic dark-matter particle χ . We have then derived the squared amplitudes for the key decay and scattering processes. On this basis, we are now ready to move to Chapter 3, where these results will be used to reproduce the observed dark-matter relic abundance.

Chapter 3

Our Model: Dark Matter Relic Abundance

In this chapter we will study DM production to test our model, outlined in cap. 2. After an introductory discussion on the structure of the Boltzmann equation and two DM production mechanisms, we will compute the relic abundance of DM. We will exploit controlled analytic limits to expose the parametric behavior, and identify the regions of the parameter space compatible with the observed relic abundance.

3.1 Boltzmann Equation

In cap. 2 we built up a theoretically self-consistent DM model, in which the X -boson acts as a mediator of the interactions between the DM particle and the SM ones. In order to check its viability, we need to describe how to compute in practice the abundance of DM.

For a DM model to be viable, it must reproduce coherently the current DM abundance observed in the universe ($\Omega_{DM} h^2$), parameter introduced in sec. 1.2. Our aim is, thus, to figure out how the dynamics of our specific particle-physics model may explain DM abundance we observe today. Boltzmann equation has precisely this aim, since it connects the DM particle number density (n_{DM}), a parameter strictly tied to abundance, to the amplitudes of particle-physics processes.

Consider the simplest case, in which a particle species A has no interactions at all. The number density of particles A (n_A) in a comoving volume V will then remain constant

$$\frac{d}{dt}(n_A V) = 0. \quad (3.1)$$

On the contrary, let us assume that a particle species A may interact with a particle species B via the processes:



The number density of A particles in a volume V will vary in time as

$$\begin{aligned} \frac{d}{dt}(n_A V) = & V S_f \sum_{dofs} \int d\Pi_B \int d\Pi_{A_1} \int d\Pi_{A_2} (2\pi)^4 \delta^{(4)}(p_B - p_{A_1} - p_{A_2}) \\ & \times \left[2|\mathcal{A}_{B \rightarrow AA}|^2 f_B (1 \pm f_A)^2 - 2|\mathcal{A}_{AA \rightarrow B}|^2 (1 \pm f_B) f_A^2 \right], \end{aligned} \quad (3.3)$$

where $S_f = 1/2!$ is the overall symmetry factor, accounting for the presence of identical particles in the initial and/or final state of the reaction. This factor ensures that the phase-space integrals do not overcount physically equivalent configurations. Here $d\Pi_a \equiv \frac{d^3 p_a}{(2\pi)^3 2E_a}$ is the relativistic phase space of particle species a ($a = B, A_1, A_2$). $|\mathcal{A}_{B \rightarrow AA}|^2$ and $|\mathcal{A}_{AA \rightarrow B}|^2$ are the squared amplitudes of the processes we are considering. The sum in eq. (3.3) runs over the initial and final states internal degrees of freedom ($dofs$). f_i ($i = A, B$) are the phase space densities of the various particle species, namely

$$n_i = \hat{g}_i \int \frac{d^3 p}{(2\pi)^3} f_i, \quad (3.4)$$

\hat{g}_a counts the internal degrees of freedom such as polarizations and multiplet components.

Each process is weighted by relative phase space density f_i of each of the initial state particles, while terms like $(1 \pm f_i)$ takes into account stimulated emission effects for bosonic final state particles (plus sign) or Pauli blocking for fermionic ones (minus sign). Finally, pre-factors ± 2 take into account the fact that the process $B \rightarrow A A$ is adding two A particles to the bath, while $A A \rightarrow B$ is removing two. (In what follows, we will use the shorthand notation $B \Leftrightarrow A A$ to include both processes)

Notice that here A_1 and A_2 denote the two identical particles in the final state: they carry, in general, different momenta in the phase-space integration, but share the same phase space densities f_A since they belong to the same species.

The same reasoning applies to a generic $2 \rightarrow 2$ scattering or annihilation process, where the species A interacts with other particles B, C and D through

$$A B \Leftrightarrow C D. \quad (3.5)$$

Repeating the steps outlined above, one finds that the Boltzmann equation for the number density of A in a comoving volume V takes the form

$$\begin{aligned} \frac{d}{dt}(n_A V) = & V S_i S_f \sum_{dofs} \int d\Pi_A \int d\Pi_B \int d\Pi_C \int d\Pi_D (2\pi)^4 \delta^{(4)}(p_A + p_B - p_C - p_D) \\ & \times \left[|\mathcal{A}_{CD \rightarrow AB}|^2 f_C f_D (1 \pm f_A)(1 \pm f_B) - |\mathcal{A}_{AB \rightarrow CD}|^2 f_A f_B (1 \pm f_C)(1 \pm f_D) \right]. \end{aligned} \quad (3.6)$$

All symbols appearing in eq. ((3.6)) have the same meaning as in the previous case. Notice that in this case, the symmetry factors S_i and S_f are nothing but the same kind of combinatorial factors discussed above, now written in a fully general form for arbitrary initial and final states:

$$S_i = \begin{cases} \frac{1}{2!} & \text{for } A = B, \\ 1 & \text{for } A \neq B, \end{cases} \quad S_f = \begin{cases} \frac{1}{2!} & \text{for } C = D, \\ 1 & \text{for } C \neq D. \end{cases} \quad (3.7)$$

This makes clear that the structure of the Boltzmann equation is completely general: for a process with n incoming and m outgoing particles, the Boltzmann equation always contains a product of n distribution functions f_i for the initial states and m statistical factors $(1 \pm f_i)$ for the final states.

After these two examples, it is useful to introduce a few general quantities, that will be key ingredients in the following analysis.

From the physical point of view, the expansion of the universe dilutes the concentration of particles. In the Boltzmann equation (3.3) this can be made evident by expanding the time derivative in the LHS

$$\frac{1}{V} \frac{d}{dt} (n_A V) = \dot{n}_A + 3 n_A H = \dot{Y}_A s, \quad (3.8)$$

where H is the Hubble expansion rate. The term $3 n_A H$ is taking into account the dilution effect. The abundance is defined as $Y \equiv n/s$, where s is the entropy density. The entropy density and the Hubble parameter vary with the temperature of the Universe as:

$$\begin{aligned} s(T) &= \frac{2\pi^2}{45} g_S^*(T) T^3, \\ H(T) &= 1.66 \sqrt{g_\rho^*(T)} \frac{T^2}{M_{\text{Pl}}}, \end{aligned} \quad (3.9)$$

where M_{Pl} is the Planck mass. The functions $g_S^*(T)$ and $g_\rho^*(T)$ quantify the total number of relativistic degrees of freedom contributing to the entropy and energy density of the Universe. Their values decrease whenever a particle species becomes non-relativistic. They are defined as:

$$g_\rho^*(T) = \sum_{i \in \text{bosons}} \hat{g}_i \left(\frac{T_i}{T} \right)^4 + \frac{7}{8} \sum_{i \in \text{fermions}} \hat{g}_i \left(\frac{T_i}{T} \right)^4, \quad (3.10)$$

$$g_S^*(T) = \sum_{i \in \text{bosons}} \hat{g}_i \left(\frac{T_i}{T} \right)^3 + \frac{7}{8} \sum_{i \in \text{fermions}} \hat{g}_i \left(\frac{T_i}{T} \right)^3, \quad (3.11)$$

where, again, \hat{g}_i counts the internal degrees of freedom of species i and T_i is its temperature.

The evolution of $g_\rho^*(T)$ and $g_S^*(T)$ across the thermal history of the Universe is shown in fig.3.1.

Before moving to specific models, it is also convenient to introduce the thermally averaged cross section, which will be useful in the following. For a generic $2 \rightarrow 2$ process $A B \rightarrow C D$, we define $\langle \sigma v \rangle$ as:

$$\langle \sigma v \rangle \equiv \int \frac{d\Pi_A d\Pi_B}{n_A^{\text{eq}} n_B^{\text{eq}}} d\Pi_C d\Pi_D f_A^{\text{eq}}(p_A) f_B^{\text{eq}}(p_B) (2\pi)^4 \delta^{(4)}(p_A + p_B - p_C - p_D) |\mathcal{A}_{AB \rightarrow CD}|^2, \quad (3.12)$$

where $f_{A,B}^{\text{eq}}$ are the equilibrium distribution functions. A species is in equilibrium when the processes that create and annihilate it occur at the same rate, so that on average its number density tracks the equilibrium value $n_i^{\text{eq}}(T)$ associated with the Maxwell–Boltzmann distribution $f_i^{\text{eq}}(p, T) \propto e^{-E(p)/T}$.

A more detailed discussion of equilibrium, and of the conditions under which a species follows or departs from $n^{\text{eq}}(T)$ will be given in the next section.

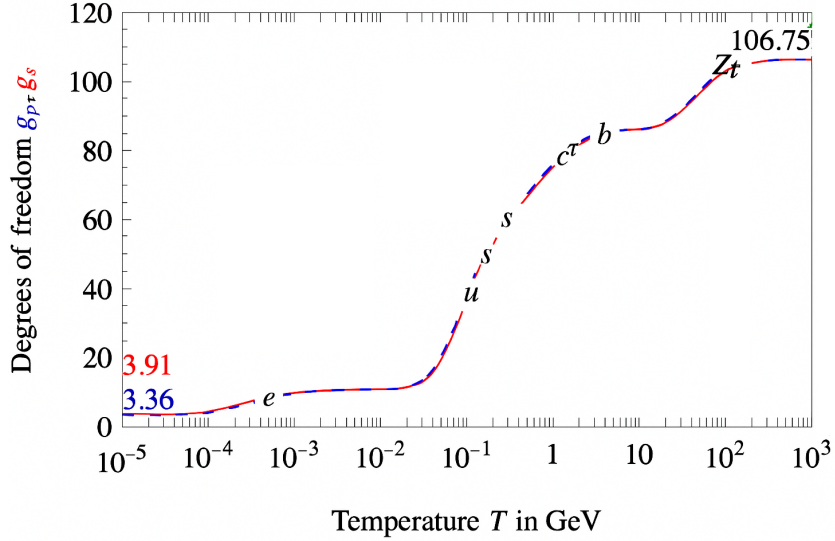


Figure 3.1 Temperature evolution of the effective numbers of degrees of freedom. Image taken from Ref. [6].

Let us highlight that Boltzmann equation allows us to compute the DM abundance, but being a differential equation, is highly dependent from initial state conditions. From a physical point of view, this means that the same abundance of DM we observe today can be obtained through very different production mechanisms, corresponding to radically different dynamics in the early Universe. In the next section, we will discuss two DM production scenarios which differ from each other in this sense: freeze-in and freeze-out.

3.2 Production Mechanisms

We will now discuss the main features of two of the possible DM production scenarios.

3.2.1 Freeze-out

Historically, freeze-out is the standard framework for DM production. Freeze-out has two main assumptions: DM was already present in the early Universe after the Big Bang, and was in equilibrium with the SM particles present in the hot plasma, namely the thermal bath.

At a qualitative level, freeze-out has three phases: as long as equilibrium holds, the DM number density closely tracks its equilibrium value, then, once temperature drops below DM mass, it decreases exponentially. As the Universe cools further, however, the annihilation rate can no longer keep up with the Hubble expansion, so the number of dark matter particles stops decreasing and a non-zero relic abundance is left over. These three regimes are shown in fig. 3.2, which displays the evolution of the abundance as a function of the dimensionless parameter $z \equiv M/T$, where M is the DM mass.

Before proceeding, it is convenient to introduce a compact notation for processes that change

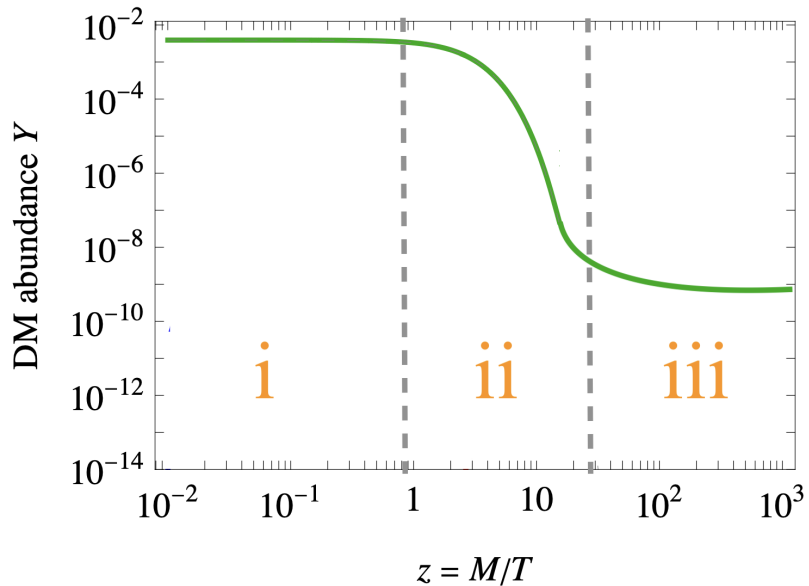


Figure 3.2 Evolution of the DM abundance Y in a freeze-out scenario. (i) For $z \ll 1$ ($T \gg m_\chi$) the abundance tracks its equilibrium value and remains approximately constant. (ii) Around $z \sim 1$ the DM becomes non-relativistic, annihilations become inefficient, and the abundance rapidly departs from equilibrium. (iii) For $z \gg 1$ annihilations freeze out and the abundance settles to its final asymptotic value, determining the relic density. Figure adapted from Ref. [6].

the number of DM particles. We denote by $M \leftrightarrow N$ a reaction in which M DM particles appear in the initial state and N in the final state. For simplicity, in the standard freeze-out analysis one considers the case of a $2 \leftrightarrow 0$ process, namely $\chi \chi \leftrightarrow S M S M$ annihilations, where χ denotes a single dark-matter species and ‘‘SM’’ stands for an arbitrary of Standard Model particle. In this setup, the Boltzmann equation takes precisely the form discussed in sec. 3.1, in eq. (3.6).

We will now discuss more in depth the main ingredients and the features involved in freeze-out computations, describing separately the three regimes from fig. 3.2.

(i) Thermal equilibrium regime

As long as the temperature is higher than the DM mass, $T \gtrsim m_\chi$, the typical kinetic energy of particles in the plasma is large enough to efficiently produce and annihilate DM. Indeed, in this regime, both the annihilation processes $\chi \chi \rightarrow S M S M$ and the inverse $S M S M \rightarrow \chi \chi$ are kinematically allowed and unsuppressed. As a result, for every annihilation there is, on average, a corresponding inverse process. This condition is referred to as (chemical) equilibrium. Consequently, the DM number density closely tracks its equilibrium value $n_\chi^{\text{eq}}(T)$, corresponding to the usual Maxwell-Boltzmann distribution $f_\chi^{\text{eq}}(p, T) \propto e^{-E(p)/T}$. This behavior is clearly illustrated by region (i) in fig. 3.2, where the abundance exhibits an extended plateau at early times (small z). In the plot, up to $z \simeq 1$ ($T \simeq m_\chi$) the abundance remains constant thanks to equilibrium.

(ii) Freeze-out epoch

When the temperature drops below the DM mass, $T \lesssim m_\chi$, the situation changes qualitatively. Inverse processes like $SM \rightarrow \chi \chi$ are fed only by the exponentially rare tail of the Boltzmann distribution, and their rate becomes strongly suppressed compared to annihilations. As the universe cools, DM concentration therefore falls exponentially and the actual DM abundance keeps following the Boltzmann-suppressed equilibrium curve down, as shown by the behavior in region (ii) of fig. 3.2.

(iii) Frozen relic regime

Decoupling is the final key aspect: provided again that DM is coupled to SM, interactions between the two sectors will occur with a annihilation rate Γ . If the rate is much larger than the Hubble rate, namely

$$\Gamma \gg H, \quad (3.13)$$

the typical timescale between interactions, Γ^{-1} , is much shorter than the expansion timescale, H^{-1} . In this regime, a DM particle undergoes many interactions before the cosmic expansion can significantly dilute the plasma. As the universe expands and cools further, the interaction rate between DM particles and the thermal bath decreases. When the temperature reaches a decoupling value T_{dec} , the annihilation rate per particle becomes too small to balance the dilution, i.e. when $\Gamma \lesssim H$. From that point on, the Hubble expansion dominates over annihilations: DM particles become effectively decoupled from the plasma, and their number density freezes to an almost constant value. This determines the so-called freeze-out of the DM abundance, after which the relic abundance remains essentially unchanged, as illustrated by the third slice in fig. 3.2, where the abundance settles to its asymptotic freeze-out value.

Now we will derive a rough estimate for the mass and coupling scalings in this scenario: we will treat the observed relic abundance as a constraint in the Boltzmann equation and we will determine which parameters allow to reproduce it.

Consider the standard annihilation process relevant for freeze-out, $2 \leftrightarrow 0$, whose rate per particle is

$$\Gamma_{\text{ann}}(T) \equiv n_\chi(T) \langle \sigma v \rangle(T). \quad (3.14)$$

The expression above (eq. 3.14) can be understood as follows: for a $2 \leftrightarrow 0$ process, the probability that a given DM particle annihilates in a unit time is equal to the probability of encountering another DM particle in the plasma, n_χ , multiplied by the interaction strength, encoded in the thermally averaged cross section $\langle \sigma v \rangle$.

As mentioned before, freeze-out occurs when, at a temperature T_{fo} , annihilations become too slow to compete with the Hubble expansion,

$$\Gamma_{\text{ann}}(T) \simeq H(T) \quad (3.15)$$

with $H(T)$ defined in eq. (3.9). As discussed in any standard reference on thermal relic dark matter (see for instance [19]), the requirement of reproducing the observed relic abundance implies a thermally averaged annihilation cross section of the order

$$\langle\sigma v\rangle_{\text{DM}} \sim 10^{-9} \text{ GeV}^{-2} \sim 10^{-26} \text{ cm}^3/\text{s}. \quad (3.16)$$

The cross section derived above is naturally obtained for weak-scale couplings and masses. This numerical coincidence led to the so-called Weakly Interacting Massive Particle (WIMP) miracle: the observation that dark matter could simply be made of particles with approximately electroweak strength interactions, automatically yielding the correct relic abundance.

However, despite extensive searches no experiment has yet observed a signal compatible with WIMPs. These persistent null results now strongly constrain the simplest WIMP models, and motivate the study of alternative production mechanisms for dark matter.

3.2.2 Freeze-in Mechanism

During the recent years, another DM production mechanism was brought to light, turning upside down the freeze-out perspective. Firstly introduced in [20], freeze-in assumes that after the big bang the DM concentration was negligible, and DM is so feebly coupled with SM particles that it never reached equilibrium with the thermal bath. Although the interactions with SM particles are feeble, they increment the DM abundance gradually over time, with each rare interaction contributing only a small fraction of the final relic density. This behavior is clearly visible in the blue and red curves of fig. 3.3.

Before examining the quantitative evolution of the abundance, it is useful to distinguish the two qualitatively different regimes of freeze-in production: IR and UV freeze-in, both illustrated in fig. 3.3. In the first scenario the production of DM occurs entirely at low energies. As we will show later, the dominant contribution to the abundance comes from temperatures close to the dark matter mass. Most of the abundance is therefore accumulated around $z \sim 1$ (i.e. $T \sim m_\chi$), just like the red line in fig. 3.3. Notice that in our model, if DM is lighter than X , an analogous argument applies to m_X : the resonant contribution at temperatures $T \sim m_X$ dominates the production rate, so that this temperature range gives the largest contribution to the final abundance.

UV freeze-in on the other hand is characterized by a high-energy (and high temperature) DM production. This behavior typically arises when the interactions responsible for DM production originate from non-renormalizable operators. Since the interaction induced by a non-renormalisable operator scales with energy, $\sigma \propto E^2/\Lambda^2$ (or, in general, with an even higher power for operators of dimension > 5), the corresponding production rate increases at high temperatures. As a result, the dominant contribution to the DM abundance is generated at the earliest, hottest stages of the thermal history, making this channel intrinsically UV-dominated. This behavior is precisely what is illustrated by the blue curve in fig. 3.3, where the DM abundance is built up predominantly at very early times (small z), when the temperature is the highest.

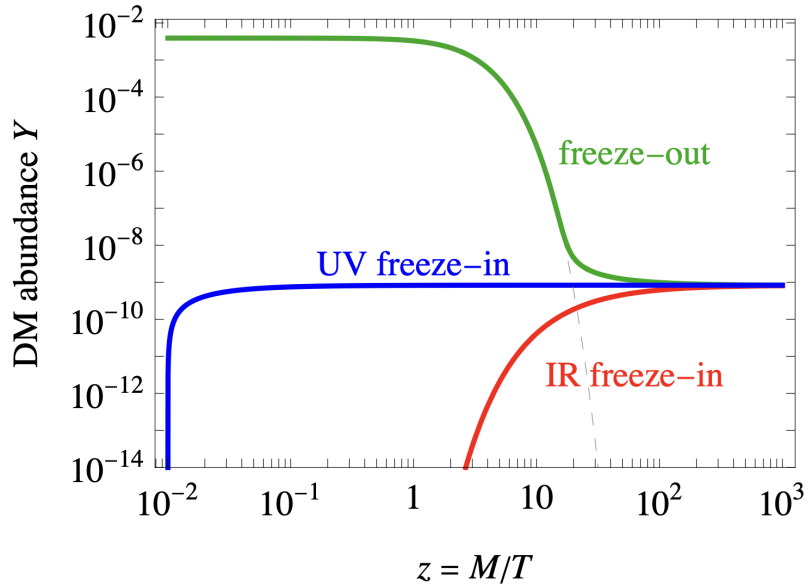


Figure 3.3 Log-Log plot of the evolution of the DM abundance Y as a function of the dimensionless parameter $z = M/T$, where M denotes the mass scale of the heaviest particle involved in the production process. The green curve shows the standard freeze-out behavior. The blue and red curves illustrate UV and IR freeze-in production, respectively.

Finally, we comment on the role of other possible production channels. In the present model, DM production proceeds exclusively through processes of the type $2 \leftrightarrow 0$. In principle, one could also consider scenarios where freeze-in is driven by $1 \leftrightarrow 0$ processes, corresponding to the decay of a particle in the thermal bath directly into DM. Such scenarios have been studied in the context of thermal decays of DM. We do not consider this possibility further here, and refer the reader to refs. [21, 22].

Having outlined the qualitative features of freeze-out and freeze-in production mechanism, we now focus on the scenario relevant for our model. In particular, in our framework the model adopted is the one from the first line of tab. 2.2, and DM is produced through IR freeze-in. In what follows we specialize to this case and derive the relic abundance in detail, computing step by step all the quantities entering the Boltzmann equation and identifying the parameter space consistent with observations.

3.3 Freeze-in Calculation

In this section we present the core calculation of the DM abundance in our model. As mentioned before, we work within a framework where the dark matter particle χ is a right-handed Majorana fermion, interacting with the visible sector through a light scalar mediator X , which acts as the portal between the SM and the dark sector. Starting from the general freeze-in formalism discussed

above, we now derive explicit analytic expressions for the relic density, and evaluate how it depends on the parameters of the theory.

Before diving into calculations, we list the main standard approximations for freeze-in, in accordance with those used in classic freeze-in analyses in literature (e.g. [20]).

First of all, we assume that the X boson is in equilibrium with the SM plasma during the DM production era. This is justified because DM is mainly produced at temperatures $T_{\text{prod}} \sim \mathcal{O}(m_X)$ (as hinted above, and as we will see in sec. 3.4), where equilibrium is easily maintained. A rough estimate of the equilibrium condition from eq. (3.13) gives

$$\frac{\Gamma_X}{H(T = m_X)} \sim \frac{g_e^2 M_{\text{Pl}}}{m_X} \gg 1. \quad (3.17)$$

For the values relevant to our setup, $g_e \sim \mathcal{O}(10^{-4})$ and $m_X \sim \mathcal{O}(10 \text{ MeV})$, this ratio is of the order $10^{13} \gg 1$, so the equilibrium assumption is safely satisfied.

Then we assume the usual Boltzmann phase space distribution for species at equilibrium

$$f_X = f_X^{\text{eq}} \approx e^{-\frac{E_X}{T}}.$$

For detailed definitions and equilibrium criteria, see the standard reference [23].

Finally, in the freeze-in framework, DM concentration remains negligible during the whole production. Hence we set to zero its phase space density: $f_\chi \approx 0$.

Our model features several interaction channels that contribute to dark-matter production, all originating from the low-energy interaction Lagrangian introduced earlier. In what follows, we analyze each relevant process in turn, insert it into the Boltzmann equation, and compute its individual contribution to the final DM abundance. The channels of interest are

1. $X \rightleftharpoons{} \chi\chi$
2. $e^+e^- \rightleftharpoons{} \chi\chi$
3. $e^+e^- \rightleftharpoons{} \chi\nu$.

In practice, the third process will be neglected in the subsequent analysis. As discussed at the end of cap. 2 and further motivated by the considerations presented in appendix A, interactions involving neutrinos are phenomenologically suppressed and do not play a significant role in determining the DM relic abundance. For this reason, in the remainder of this chapter we will focus exclusively on the first two channels, which set the freeze-in relic abundance.

3.3.1 Freeze-in by $X \rightarrow \chi\chi$ Decay

We consider the case where the only possible channel available for DM production is $X \leftrightarrow \chi\chi$. This case is analogous to the first one discussed in sec. 3.1, the Boltzmann equation takes the same form

as the expression in eq. (3.3). Once the freeze-in approximations introduced above are applied the formula reduces to

$$\dot{Y}_\chi s \approx \frac{1}{2!} \int d\Pi_X e^{-\frac{E_X}{T}} \int d\Pi_{\chi_1} \int d\Pi_{\chi_2} (2\pi)^4 \delta^{(4)}(p_X - p_1 - p_2) \times 2 \sum_i |\mathcal{A}_{X \rightarrow \chi\chi}|^2. \quad (3.18)$$

The squared modulus of the amplitude summed over initial and final polarizations ($\sum_i |\mathcal{A}_{X \rightarrow \chi\chi}|^2$) was derived in sec. 2.2. The factor $\frac{1}{2!}$ is the final state symmetry factor.

Substituting the standard two-body decay rate

$$\Gamma_{X \rightarrow \chi\chi} = \frac{1}{2m_X} \frac{1}{2!} \int d\Pi_{\chi_1} d\Pi_{\chi_2} (2\pi)^4 \delta^{(4)}(P - p_1 - p_2) |\mathcal{A}_{X \rightarrow \chi\chi}|^2, \quad (3.19)$$

we obtain:

$$\dot{Y}_\chi s \approx 2 \int d\Pi_X e^{-\frac{E_X}{T}} 2m_X \Gamma_{X \rightarrow \chi\chi}. \quad (3.20)$$

Exploiting spherical coordinates for the 3-momenta and recalling that $|p_X|d|p_X| = E_X dE_X$

$$\begin{aligned} \dot{Y}_\chi s &\approx \frac{m_X \Gamma_{X \rightarrow \chi\chi}}{\pi^2} \int_{m_X}^{\infty} dE_X \sqrt{E_X^2 - m_X^2} e^{-\frac{E_X}{T}} \\ &= \frac{m_X^2 \Gamma_{X \rightarrow \chi\chi}}{\pi^2} T K_1\left(\frac{m_X}{T}\right), \end{aligned} \quad (3.21)$$

where K_1 is the modified Bessel function of the first type.

As the RHS does not depend explicitly upon Y_χ , we simply integrate it in time. Since $\dot{T} \approx -H(T)T$, where $H(T)$ is the Hubble parameter discussed in eq. (3.9), the integration measure can be rewritten as $dt \approx -dT/(H(T)T)$. Indeed, the integration over time is equivalent to an integration over temperature so that

$$\begin{aligned} Y_\chi &\approx \int_{t_{min}}^{t_{max}} dt \frac{m_X^2 T \Gamma_{X \rightarrow \chi\chi}}{\pi^2 s} K_1\left(\frac{m_X}{T}\right) \\ &\approx \frac{m_X^2 \Gamma_{X \rightarrow \chi\chi}}{\pi^2} \int_{T_{min}}^{T_{max}} dT \frac{K_1\left(\frac{m_X}{T}\right)}{H(T)s(T)}. \end{aligned} \quad (3.22)$$

The explicit temperature dependence of s is expressed again in eq. (3.9).

We perform the integral above by using $z \equiv m_X/T$, which was firstly introduced in sec. 3.2. This step allows us to simplify the integral. In fact, since $T_{min} \ll m_X$ and $T_{max} \gg m_X$, we can take $z_{min} \approx 0$ and $z_{max} \approx \infty$ for the integration range:

$$\begin{aligned} Y_\chi &\approx \frac{45}{1.66 \cdot 2 \pi^4} \frac{M_{Pl}}{g_s^* \sqrt{g_\rho^*}} \frac{\Gamma_{X \rightarrow \chi\chi}}{m_X^2} \int_0^\infty dz z^3 K_1(z) \\ &= \frac{135}{1.66 \cdot 4 \pi^3} \frac{M_{Pl}}{g_s^* \sqrt{g_\rho^*}} \frac{\Gamma_{X \rightarrow \chi\chi}}{m_X^2}. \end{aligned} \quad (3.23)$$

The factor z^3 in the first line originates from the explicit T -dependence of the parameters H and s , once rewritten in terms of the dimensionless variable $z = m_X/T$.

Regarding the temperature dependence of the effective numbers of relativistic degrees of freedom, $g_\rho^*(T)$ and $g_s^*(T)$, can be safely neglected in this context. This is due to the general feature of IR

freeze-in mentioned in sec. 3.2: the production of DM is dominated at most around temperatures of order the mediator mass, $T \sim m_X$, which in our setup lies at the level of a few MeV. Below $\mathcal{O}(10 \text{ MeV})$ both g_ρ^* and g_s^* remain essentially constant throughout the entire production epoch. For this reason we evaluate them at $T \simeq m_X$ and treat them as fixed parameters in the integral. At these temperatures the only SM species that are still relativistic are photons, electrons and positrons, and the three active neutrino flavors. As a result, we compute the effective number of relativistic degrees of freedom from eq. (3.10) and (3.11)

$$g^* \simeq g_\rho^* \simeq g_s^* = \hat{g}_\gamma + \frac{7}{8}(2\hat{g}_e + 3\hat{g}_{\nu_i}) = 2 + \frac{7}{8}(4 + 3 \times 2) = 10.75. \quad (3.24)$$

For further clarity, one may look at fig. 3.1: below temperatures of order $\mathcal{O}(10 \text{ MeV})$ the effective relativistic degrees of freedom remain essentially constant, confirming that g_ρ^* and g_s^* can be treated as temperature independent throughout the IR freeze-in production epoch.

At this point, we can derive the decay rate from eq. (3.19) using the amplitude derived in sec. 2.2

$$\Gamma_{X \rightarrow \chi\chi} = \frac{1}{2!} \frac{\sqrt{m_X^2 - 4m_\chi^2}}{16\pi m_X^2} |\mathcal{A}_{X \rightarrow \chi\chi}|^2 = \frac{1}{2!} \frac{g_\chi^2}{8\pi m_X^2} (m_X^2 - 4m_\chi^2)^{\frac{3}{2}}. \quad (3.25)$$

Inserting this in eq. (3.23) we can finally write the abundance as

$$Y_\chi = g_\chi^2 \frac{135}{1.66 \cdot 64\pi^4} \frac{M_{Pl}}{g_s^* \sqrt{g_\rho^*}} \frac{(m_X^2 - 4m_\chi^2)^{3/2}}{m_X^4}. \quad (3.26)$$

The physical parameter constrained by cosmology (see sec. 1.2.2) is the present-day relic density $\Omega_\chi h^2$, which is directly related to Y_χ through

$$\Omega_\chi h^2 \approx 2.74 \times 10^5 m_\chi [\text{MeV}] Y_\chi \approx \frac{1.09 \times 10^{27}}{g_s^* \sqrt{g_\rho^*}} \frac{m_\chi \Gamma_{X \rightarrow \chi\chi}}{m_X^2}. \quad (3.27)$$

This concludes the analysis of the freeze-in production via the decay channel $X \rightarrow \chi\chi$. We now move to the second class of processes contributing to dark-matter production in our model, the scattering channel $e^+e^- \rightarrow \chi\chi$, which requires a separate treatment within the Boltzmann framework.

3.3.2 Freeze-in by $e^+e^- \rightarrow \chi\chi$ Scattering

In the case of DM interacting with the SM only via $e^+e^- \rightarrow \chi\chi$ process, we can start our computation of the frozen-in abundance from eq. (3.6).

Working directly with the variable z , for the specific case of $e^+e^- \rightarrow \chi\chi$, eq. (3.6) becomes

$$s H z \frac{dY_\chi}{dz} = \sum_{\text{all}} \int d\Pi_{e^+} d\Pi_{e^-} d\Pi_{\chi_1} d\Pi_{\chi_2} (2\pi)^4 \delta^{(4)}(p_{e^+} + p_{e^-} - p_{\chi_1} - p_{\chi_2}) \times \quad (3.28) \\ \left(2 |\mathcal{A}_{e^+e^- \rightarrow \chi\chi}|^2 f_{e^+} f_{e^-} (1 - f_\chi)^2 - 2 |\mathcal{A}_{\chi\chi \rightarrow e^+e^-}|^2 f_\chi^2 (1 - f_{e^-})(1 - f_{e^+}) \right).$$

Using the same approximations introduced at the beginning of this section (the very first ones applied in the decay case $X \rightarrow \chi\chi$), the Boltzmann equation simplifies to

$$s H z \frac{dY_\chi}{dz} = \sum_{\text{all}} \int d\Pi_{e^+} d\Pi_{e^-} e^{-\frac{E_{e^+}}{T}} e^{-\frac{E_{e^-}}{T}} \int d\Pi_{\chi_1} d\Pi_{\chi_2} (2\pi)^4 \delta^{(4)}(p_{e^+} + p_{e^-} - p_{\chi_1} - p_{\chi_2}) \times \quad (3.29)$$

$$2 |\mathcal{A}_{e^+ e^- \rightarrow \chi\chi}|^2.$$

To proceed, it is convenient to rewrite the phase-space integrals in terms of Lorentz-invariant Mandelstam variables. We first introduce:

$$\hat{s} = (p_{e^-} + p_{e^+})^2, \quad \hat{t} = (p_{e^-} - p_{\chi_1})^2, \quad \hat{u} = (p_{e^-} - p_{\chi_2})^2, \quad (3.30)$$

which encode the full kinematics of the $2 \rightarrow 2$ scattering process.

In order to change the integration variables from momenta to $(\hat{s}, \hat{t}, \hat{u})$, we recall that the Mandelstam variables satisfy the constraint:

$$\hat{s} + \hat{t} + \hat{u} = 2m_e^2 + 2m_\chi^2, \quad (3.31)$$

so only two of them are independent variables. This allows us to rewrite the phase-space integrals in terms of (\hat{s}, \hat{t}) alone, with \hat{u} fixed by the relation above.

After rewriting the phase-space measure in terms of Mandelstam invariants and using the energy-conserving delta function, the equilibrium factors reorganize into the modified Bessel function $K_1(\sqrt{\hat{s}}/T)$. The Boltzmann equation thus reduces to two remaining integrals, over \hat{s} and \hat{t} .

At this point, the remaining integral over the Mandelstam variable \hat{t} can be performed explicitly. This step isolates the standard cross section $\sigma(\hat{s})$ defined as follows:

$$\sigma(\hat{s}) = S_f \sum_{\text{final}} \int_{t_{min}}^{t_{max}} d\hat{t} \frac{\langle |\mathcal{A}|^2 \rangle_{\text{initial}}}{16\pi \hat{s}^2 \lambda}. \quad (3.32)$$

Here S_f is the final-state symmetry factor and $\lambda \equiv \lambda_{\text{Kal}}(1, m_e^2/\hat{s}, m_e^2/\hat{s})$ is the normalized usual Källén function.

The integration limits in \hat{t} are also standard. For fixed \hat{s} , the allowed kinematic range of the Mandelstam variable \hat{t} in the center of mass is obtained from the usual two-body scattering relations (see the PDG kinematics review [19]):

$$t_{\min/\max} = - (p_{e^-, \text{cm}} \mp p_{\chi_1, \text{cm}})^2. \quad (3.33)$$

Finally, we highlight that the quantity $\langle |\mathcal{A}|^2 \rangle_{\text{initial}}$ appearing in the integrand (3.32) is the standard spin-averaged squared amplitude from collider physics. In the freeze-in context this choice is merely conventional: the averaging over initial states is exactly compensated later when multiplying by the corresponding initial-state multiplicities \hat{g}_{e^+} and \hat{g}_{e^-} (as we will do in eq. (3.34)). We keep this convention only to ease the comparison with standard cross-section formulae.

Putting all these ingredients together, one arrives at the compact expression of eq. (3.29)

$$s H z \frac{dY_\chi}{dz} = \hat{g}_{e^+} \hat{g}_{e^-} \frac{T}{16\pi^4} \int_{\hat{s}_{\min}}^{\infty} d\hat{s} \hat{s}^{3/2} \lambda \sigma(\hat{s}) K_1\left(\frac{\sqrt{\hat{s}}}{T}\right). \quad (3.34)$$

The integration boundaries in \hat{s} follow directly from kinematics. For the process we are considering, energy conservation implies that the Mandelstam variable satisfies $\hat{s} \geq \hat{s}_{\min} = \max(4m_e^2, 4m_\chi^2)$, while no upper bound exists in general, so that $\hat{s}_{\max} = \infty$.

The result in 3.34 matches with the literature formula (see e.g. Appendix C of [6]) once specialized to the $e^+ e^- \rightarrow \chi\chi$ channel.

As done for the case of the $X \rightarrow \chi\chi$ decay, we solve the differential equation (3.34) integrating over z

$$\begin{aligned} Y_\chi &= \frac{\hat{g}_{e^+} \hat{g}_{e^-}}{16\pi^4} \int_{\hat{s}_{\min}}^{\infty} d\hat{s} \hat{s}^{3/2} \bar{\lambda} \sigma_{e^+ e^- \rightarrow \chi\chi}(\hat{s}) \int_{z_{\min}}^{z_{\max}} dz \frac{T(z)}{s(z) H(z) z} K_1\left(\frac{\sqrt{\hat{s}}}{T(z)}\right) \\ &= \frac{135}{1.66 \cdot 64 \pi^5} \frac{M_{Pl}}{g_s^* \sqrt{g_\rho^*}} \hat{g}_{e^+} \hat{g}_{e^-} \int_{\hat{s}_{\min}}^{\infty} d\hat{s} \frac{\bar{\lambda}}{\sqrt{\hat{s}}} \sigma_{e^+ e^- \rightarrow \chi\chi}(\hat{s}). \end{aligned} \quad (3.35)$$

Using the squared amplitude derived in sec. 2.2 (see eq. (2.18)) and plugging it into eq. (3.32), we have that

$$\sigma(\hat{s}) = \frac{g_\chi^2 g_e^2 (\hat{s} - 4m_\chi^2)^{3/2} \sqrt{\hat{s} - 4m_e^2}}{8\pi \hat{g}_{e^+} \hat{g}_{e^-} (\Gamma_X^2 m_X^2 + (m_X^2 - \hat{s})^2) \hat{s}}, \quad (3.36)$$

so that

$$Y_\chi = \frac{135}{1.66 \cdot 64 \pi^5} \frac{M_{Pl}}{g_s^* \sqrt{g_\rho^*}} \frac{g_\chi^2 g_e^2}{8\pi} \int_{\hat{s}_{\min}}^{\infty} d\hat{s} \frac{(\hat{s} - 4m_\chi^2)^{3/2} (\hat{s} - 4m_e^2)^{3/2}}{\hat{s}^{5/2} [\Gamma_X^2 m_X^2 + (m_X^2 - \hat{s})^2]}. \quad (3.37)$$

The integral in eq. (3.37) has no analytical solution, thus we keep the abundance in its integral representation. The results of a specific numerical study of this integral will be presented in a more detailed way in sec. 3.4 when discussing analytic limits.

3.4 Freeze-in Abundance: Mass Regimes and Analytic Limits

In this section we will analyze the freeze-in abundance generated by the scattering process discussed in sec. 3.3.2. Starting from the integral expression in eq. (3.37), we will derive simple analytic approximations in two complementary DM mass regimes. Specifically, we will study the case of DM lighter than the mediator X and the opposite, showing how the relic abundance scales with the DM mass and the couplings in each limit.

3.4.1 Resonant Regime

The resonant regime is the one in which the decay $X \rightarrow \chi\chi$ is kinematically allowed, namely $m_\chi < m_X/2$, and in the following we will show how the scattering $e^+ e^- \rightarrow \chi\chi$ gives the same contribution to the DM abundance.

To evaluate 3.37 in this regime, we will adopt the narrow-width approximation (NWA), which is valid when the decay width of the mediator X is much smaller than its mass, namely

$$\frac{\Gamma_X}{m_X} \ll 1. \quad (3.38)$$

tiny values of the coupling g_e imply

$$\frac{\Gamma_X}{m_X} \approx \mathcal{O}\left(\frac{g_e^2}{8\pi}\right) \ll 1. \quad (3.39)$$

Notice that among the decay channels of X allowed by the interaction Lagrangian (eq. (2.12)), we will focus only on $X \rightarrow e^+ e^-$; since the dark-sector couplings governing $X \rightarrow \chi \chi$ are expected to be tiny (as we will see in what follows), and the ones entering in $X \rightarrow \chi \nu$ decay are phenomenologically ultra-suppressed, as discussed in app. A. Indeed the total decay width can be approximated to:

$$\Gamma_X \approx \Gamma_{X \rightarrow e^+ e^-} = \frac{g_e^2}{8\pi m_X^2} (m_X^2 - 4m_e^2)^{3/2}. \quad (3.40)$$

Using the NWA

$$\frac{1}{(\hat{s} - m^2)^2 + m^2 \Gamma^2} \xrightarrow{\Gamma \ll m} \frac{\pi}{m \Gamma} \delta(\hat{s} - m^2), \quad (3.41)$$

so that the abundance can be expressed as

$$Y_\chi = g_\chi^2 \frac{135}{1.66 \cdot 64\pi^4} \frac{M_{Pl}}{g_s^* \sqrt{g_\rho^*}} \frac{g_e^2 (m_X^2 - 4m_\chi^2)^{3/2} (m_X^2 - 4m_e^2)^{3/2}}{8\pi \Gamma_X m_X^6}. \quad (3.42)$$

We stress that, in the presence of a thermal bath, the validity of the NWA is more subtle than the one proposed in equation 3.38. In appendix C we report both a comparison with the full numerical integration of the abundance integral in eq. (3.37) and the discussion of the validity domain of the NWA developed in ref. [24].

Substituting the decay rate for the $X \rightarrow e^+ e^-$ from equation 3.40 in equation 3.42 we obtain

$$Y_\chi = g_\chi^2 \frac{135}{1.66 \cdot 64\pi^4} \frac{M_{Pl}}{g_s^* \sqrt{g_\rho^*}} \frac{(m_X^2 - 4m_\chi^2)^{3/2}}{m_X^4}. \quad (3.43)$$

Comparing the resonant result above with eq. (3.26), one immediately sees that the two expressions coincide. In the following, we will clarify the physical reason for this agreement and how it is linked to the treatment of the on-shell X in thermal equilibrium. The NWA, eq. (3.41), makes explicit that the resonant contribution to the scattering is dominated by the production of an on-shell X from the $e^+ e^-$ pair, followed by its decay into DM. In practice, the main contribution to the abundance comes from scatterings where the center-of-mass energy satisfies $s \simeq m_X^2$, where the available energy is just enough to produce the mediator on-shell. For this reason, the process $e^+ e^- \rightarrow \chi \chi$ is effectively described as a two-step sequence: the pure annihilation $e^+ e^- \rightarrow X$ and the decay $X \rightarrow \chi \chi$. This

factorization of the resonant contribution is the usual optical-theorem picture: the imaginary part of the propagator picks up the on-shell intermediate state and relates the scattering amplitude to the decay width of X .

The key point is that, in our setup, the X boson is assumed to remain in equilibrium with the SM bath. This means that its number density is fixed by equilibrium and does not depend on the details of how efficiently e^+e^- can resonantly produce X . As a consequence, the only relevant ingredient for the dark matter abundance is the decay $X \rightarrow \chi\chi$ itself, evaluated for an equilibrium population of X bosons. This is precisely the contribution we computed in the decay picture in sec. 2.2, and it explains why the resonant scattering result in eq. (3.26) reproduces the same expression for Y_χ . Including both the decay channel and the resonant part of the scattering channel would therefore amount to double counting the same physical process. For this reason, in what follows we retain only the decay contribution.

We stress that the resonant expression above applies to both mass hierarchies $m_\chi > m_e$ and $m_\chi < m_e$. Indeed, as long as $m_\chi < m_X/2$, the lower limit of the integral, $s_{\min} = \max(4m_e^2, 4m_\chi^2)$, always lies below m_X^2 . Therefore, the integration domain includes the on-shell pole at $s \simeq m_X^2$ picked out by the narrow-width δ -function.

3.4.2 Non-Resonant Regime

In this case only $e^+e^- \rightarrow \chi\chi$ is kinematically open, and the X never goes on-shell. As a consequence, there is no resonant peak in the propagator, and the scattering contribution is much smaller than in the previous case.

In this regime $m_\chi > m_X/2$, thus the lower limit of the integral in eq. (3.37) is $\hat{s}_{\min} = 4m_\chi^2$. Since then $m_\chi \gg m_e$, throughout the integration domain one has $\hat{s} > 4m_\chi^2 \gg 4m_e^2$, so the electron mass can be safely neglected, which simplifies the integral in eq. (3.37) to

$$Y_\chi \approx \frac{135}{1.66 \cdot 64 \pi^5} \frac{M_{\text{Pl}}}{g_s^* \sqrt{g_\rho^*}} \frac{g_\chi^2 g_e^2}{8\pi} \int_{\hat{s}_{\min}}^\infty d\hat{s} \frac{(\hat{s} - 4m_\chi^2)^{3/2}}{\hat{s} [\Gamma_X^2 m_X^2 + (m_X^2 - \hat{s})^2]} . \quad (3.44)$$

eq.3.44 can be re-written by computing the integral analitically, obtaining

$$Y_\chi \approx \frac{135}{1.66 \cdot 64 \pi^5} \frac{M_{\text{Pl}}}{g_s^* \sqrt{g_\rho^*}} \frac{g_\chi^2 g_e^2}{8 \Gamma_X m_X^2 (\Gamma_X^2 + m_X^2)} \times [8 \Gamma_X m_\chi^3 - (\Gamma_X^2 m_X^2 + (-4m_\chi^2 + m_X^2)^2)^{3/4} \left[\Gamma_X \cos\left(\frac{3}{2} \arctan\left(\frac{4m_\chi^2 - m_X^2}{\Gamma_X m_X}\right)\right) + m_X \sin\left(\frac{3}{2} \arctan\left(\frac{4m_\chi^2 - m_X^2}{\Gamma_X m_X}\right)\right) \right]] . \quad (3.45)$$

As in the resonant case, we explicitly compare the analytic result with the full numerical integration in app. C, thereby confirming the validity of the approximation in the non-resonant regime.

It is useful to look at the asymptotic behavior of eq. (3.45) in the limit of very heavy dark matter.

Expanding for $m_\chi \gg m_X$ one finds, at leading order in $1/m_\chi$,

$$Y_\chi \simeq \frac{135}{1.66 \cdot 64 \pi^5} \frac{3}{16 \cdot 8} \frac{g_\chi^2 g_e^2 M_{\text{Pl}}}{g_s^* \sqrt{g_\rho^* m_\chi}} + \mathcal{O}\left(\frac{1}{m_\chi^3}\right). \quad (3.46)$$

3.4.3 Relic-Abundance Condition and Freeze-In Parameter Space

After deriving the analytic expressions for the freeze-in abundance in the different kinematic regimes, we can now combine the results and determine the region of parameter space that reproduces the observed DM relic density, using the standard formula

$$\Omega_\chi h^2 = \frac{m_\chi s_0 Y_\chi}{\rho_c/h^2}, \quad (3.47)$$

where $s_0 \simeq 2.89 \times 10^3 \text{ cm}^{-3}$ and $\rho_c/h^2 \simeq 1.05 \times 10^{-5} \text{ GeV cm}^{-3}$ are standard cosmological parameters, for which we adopt the values reported in Ref. [19].

In particular, within the framework outlined in cap. 2, the freeze-in mechanism fixes a relation between the dark-sector coupling g_χ and the DM mass m_χ . Imposing the relic-density condition discussed in sec. 1.2

$$\Omega_{\text{DM}} h^2(g_e, m_X, g_\chi, m_\chi) = 0.12, \quad (3.48)$$

we can then identify the subset of parameters for which our scenario accounts for the present dark-matter abundance. In the present analysis we fix the X mass and its coupling to electrons (g_e) according to phenomenologically motivated considerations. In particular, we take $m_X = 17 \text{ MeV}$, consistently with the X_{17} interpretation, and we consider three representative benchmark values for the electron coupling, namely $g_e = 10^{-3}, 10^{-4}, 10^{-5}$. With these choices, the relic-density condition above determines three curves in the (g_χ, m_χ) plane along which the observed value $\Omega_{\text{DM}} h^2 \simeq 0.12$ is reproduced, and plotted in fig. 3.4.

The behavior shown in fig. 3.4 is a direct consequence of the freeze-in production mechanism. As discussed in sec. 3.2, in this regime the dark sector never thermalizes with the SM bath, and reproducing the observed relic abundance requires extremely suppressed interaction strengths. In particular, the effective coupling (g_{eff}) controlling DM production must typically lie around $g_{\text{eff}} \sim 10^{-13}$ ¹, which explains why the values of g_χ obtained in fig. 3.4 are very small.

The sharp change in behaviour visible around $m_\chi = m_X/2$ can be understood as the transition between the resonant and non-resonant regimes. For $m_\chi < m_X/2$ the process proceeds through an on-shell mediator and we are in the resonant regime, in which DM production is dominated by decays and the effective coupling is simply $g_{\text{eff}} = g_\chi \sim 10^{-13}$. For $m_\chi > m_X/2$ the resonance is no longer accessible and the dominant production mechanism becomes scattering. In this case the relevant effective coupling is $g_{\text{eff}} = g_\chi g_e \sim 10^{-13}$, so that a larger value of g_χ is required to reproduce the observed relic abundance. This explains the upward shift of the curves in the non-resonant region.

¹in agreement with the general freeze-in estimates obtained in ref. [20]

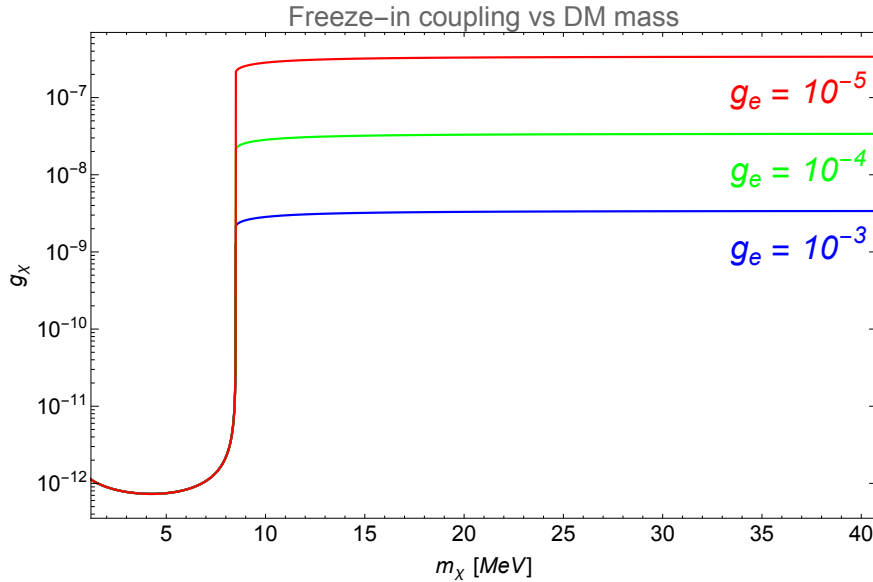


Figure 3.4 Freeze-in parameter space in the plane (m_χ, g_χ) reproducing the observed DM relic abundance within the model discussed in cap. 2. The curves are obtained by numerically evaluating the freeze-in abundance from decays and scattering processes and imposing $\Omega_{\text{DM}}h^2 = 0.12$. Different regions correspond to the resonant and non-resonant regimes discussed in sec. 3.4. In this plot we fix the mediator mass to $m_X = 17$ MeV and consider three representative benchmark values of the electron coupling, $g_e = 10^{-3}, 10^{-4}, 10^{-5}$.

Finally, it is worth stressing what is original about the result shown in fig. 3.4. The plot combines three specific ingredients: a light ~ 17 MeV mediator motivated by the PADME anomalies and DM production via the freeze-in mechanism. Works that do consider freeze-in typically treat the mediator in a model-independent way and do not match the electron coupling to the PADME-preferred scale. By concentrating on a light scalar mediator and showing that the observed relic abundance can be consistently reproduced in a genuine freeze-in regime, our analysis provides a novel and complementary perspective on DM directly linked to the PADME anomalies.

Having identified the region of parameter space that yields the correct freeze-in relic abundance, we now turn to its phenomenology. In the next chapter, we confront this region with current astrophysical and experimental bounds to assess the model's viability and its prospects for future tests.

Chapter 4

Our Results: Astrophysical and Low-Energy Probes

The goal of this chapter is to understand whether our DM model can be further constrained through astrophysical and low-energy observations. In the first case, we will focus on indirect detection (ID), which may be a further important probe on the NP couplings of our model, complementarily to the relic abundance calculation discussed in the previous chapters. Then, we will compare our results with additional constraints coming from low-energy particle-physics observables, which are sensitive to light mediators coupled to electrons.

4.1 Indirect Detection Searches

ID is a strategy to search for DM by looking at SM particles produced by DM annihilations or decays in astrophysical environments, such as the Milky Way halo. These SM particles, if detected, may carry distinct information on their DM origin.

There is, however, a well-known sensitivity gap in indirect-detection searches in the $\mathcal{O}(0.1 - 100)$ MeV energy range, where current experiments are significantly less sensitive than at both higher (GeV–TeV) and lower (keV) energies:

- charged SM particles are not valid probes below the GeV scale, since solar modulation prevents a reliable detection of low-energy cosmic rays;
- neutrinos do not provide competitive bounds in this window, due to limited experimental sensitivity (see [25]).
- Thus, photons represent the only and most promising ID channel in this energy range, even though current experiments are still only marginally sensitive to energies $\mathcal{O}(\text{MeV}) - \mathcal{O}(\text{GeV})$.

An alternative strategy for ID consists in looking at photons with energies well below the MeV scale. Such low-energy photons, specifically X-rays, can be produced as secondary radiation from

DM annihilations. In particular, in the context of our model the dominant annihilation channel will be $\chi\chi \rightarrow e^+e^-$ and will lead to the injection of energetic electrons and positrons in the astrophysical environment. These charged particles may subsequently radiate photons through well-known electromagnetic processes.

This kind of signal originates from two main channels: inverse Compton scattering (ICS), where the produced e^\pm up-scatter ambient low-energy photons in the astrophysical environment, and final state radiation (FSR), associated with photon emission directly from the final state charged particles in the DM annihilation process.

We will now briefly discuss the formalism related to the production of X-rays from DM annihilations, as discussed in ref. [26]. In particular, we will derive the differential flux of such photons. We will then make use of the results of ref. [26], obtained by integrating the differential flux over the spatial region probed by the INTEGRAL telescope [27].

A revised and updated version of the analysis of [26] has subsequently appeared, making use of the same ID strategy but incorporating a broader set of X-ray observations [28]. While the methodology is essentially unchanged, the updated study combines data from several instruments, namely XMM-Newton [29], INTEGRAL, NuSTAR [30, 31] and Suzaku [32]. By exploiting this enlarged dataset, the authors significantly strengthen the constraints on sub-GeV dark matter. These results will place upper bounds on the thermally averaged annihilation cross section, which we will thus compare with the one predicted within our model.

4.1.1 X-Ray from Dark Matter Annihilations

We fix a generic direction of observation from Earth, specified either by the angular separation θ from the Galactic Center or, equivalently, by the Galactic coordinates (b, ℓ) . The corresponding line of sight (LOS) is the straight line connecting the observer to points in the Galactic halo along this direction, parametrized by the distance from Earth. Along this LOS, DM particles annihilate at each point in the halo, producing photons that contribute to the observed signal. The observed signal is therefore described in terms of a differential photon flux $d\Phi_\gamma/(dE_\gamma d\Omega)$, which is computed by integrating the local flux contributions over the LOS.

We start with the contribution to the flux coming from FSR, where a photon is emitted by one of the charged particles in the final state of the annihilation process $\chi\chi \rightarrow e^+e^-$.

To compute the local flux contributions, we first need to derive the annihilation rate per unit volume

$$\Gamma_{\text{ann}}(r) = \frac{1}{2} \langle \sigma v \rangle n_\chi^2(r) = \frac{1}{2} \langle \sigma v \rangle \left(\frac{\rho(r)}{m_\chi} \right)^2, \quad (4.1)$$

where $\langle \sigma v \rangle$ is the thermal-averaged annihilation cross section and the factor 1/2 avoids double counting of identical pairs. The radial coordinate r measures the distance from the Galactic Center and can be expressed in terms of the LOS variable s (with $s = 0$ corresponding to the position of the Earth) according to $r^2 = s^2 + r_\odot^2 - 2sr_\odot \cos \theta$. Here r_\odot represents the solar distance to the Galactic Center.

Secondly, let $dN_{FSR\gamma}/dE_\gamma$ denote the number of photons produced via FSR per annihilation and per unit energy in the channel of interest. Then

$$\Gamma_{\text{ann}}(r) \frac{dN_{FSR\gamma}}{dE_\gamma} = \frac{1}{2} \langle \sigma v \rangle \left(\frac{\rho(r)}{m_\chi} \right)^2 \frac{dN_{FSR\gamma}}{dE_\gamma}. \quad (4.2)$$

The flux observed from a direction θ on the sky is obtained by integrating the quantity just derived along the LOS in that direction and dividing by 4π (assuming isotropic emission):

$$\frac{d\Phi_{FSR\gamma}}{dE_\gamma d\Omega} = \frac{1}{4\pi} \int_{\text{l.o.s.}} ds \frac{1}{2} \langle \sigma v \rangle \left(\frac{\rho(r(s, \theta))}{m_\chi} \right)^2 \frac{dN_{FSR\gamma}}{dE_\gamma}. \quad (4.3)$$

It is convenient to factor out the local DM density ρ_\odot at the Sun's position and to define the dimensionless J -factor

$$J(\theta) \equiv \int_{\text{l.o.s.}} \frac{ds}{r_\odot} \left(\frac{\rho(r(s, \theta))}{\rho_\odot} \right)^2. \quad (4.4)$$

The flux can then be written as

$$\frac{d\Phi_{FSR\gamma}}{dE_\gamma d\Omega}(\theta) = \frac{1}{2} \frac{r_\odot}{4\pi} \left(\frac{\rho_\odot}{m_\chi} \right)^2 J(\theta) \langle \sigma v \rangle \frac{dN_{FSR\gamma}}{dE_\gamma}. \quad (4.5)$$

This result is consistent with the standard expression reported in ref. [26]. For completeness, the Galactic DM distribution is usually modelled with a Navarro-Frenk-White profile [33]

$$\rho_{\text{NFW}}(r) = \rho_s \frac{r_s}{r} \left(1 + \frac{r}{r_s} \right)^{-2}, \quad (4.6)$$

with $\rho_s = 0.184 \text{ GeV/cm}^3$ and $r_s = 24.42 \text{ kpc}$.

The quantity $\langle \sigma v \rangle$ denotes the thermally averaged annihilation cross section of the process $\chi \chi \rightarrow e^+ e^-$, defined in Eq. 3.12. In our setup this is the only model-dependent ingredient entering Eq. 4.5, while the remaining factors follow the standard treatment of ref. [26].

The last missing ingredient is the spectrum of photons from FSR, for which we adopt the expressions of ref. [34]:

$$\frac{dN_{FSR\gamma}^{e^+ e^-}}{dE_\gamma} = \frac{\alpha}{\pi \beta (3 - \beta^2) m_\chi} \left[\mathcal{A} \ln \left(\frac{1 + R(\nu)}{1 - R(\nu)} \right) - 2 \mathcal{B} R(\nu) \right], \quad (4.7)$$

where

$$\mathcal{A} = \left[\frac{(1 + \beta^2)(3 - \beta^2)}{\nu} - 2(3 - \beta^2) + 2\nu \right], \quad (4.8)$$

$$\mathcal{B} = \left[\frac{3 - \beta^2}{\nu} (1 - \nu) + \nu \right]. \quad (4.9)$$

Here we have defined

$$\nu \equiv \frac{E_\gamma}{m_\chi}, \quad \beta^2 \equiv 1 - 4\mu^2, \quad \mu \equiv \frac{m_\ell}{2m_\chi},$$

together with

$$R(\nu) \equiv \sqrt{1 - \frac{4\mu^2}{1 - \nu}}.$$

We now move on from the discussion of final state radiation and turn to ICS, which provides an additional contribution to the photon flux relevant for indirect detection. As anticipated above, ICS probes photons that have been upscattered by electrons and positrons produced in DM annihilations within the Galaxy. This contribution is obtained by integrating the emissivity produced in each infinitesimal volume element along the LOS. Unlike the FSR case, the resulting photon flux depends on the local distribution of photons, and therefore on the detailed astrophysical environment at each point in the Galaxy.

The differential photon flux from ICS along a given direction of observation can thus be written as

$$\frac{d\Phi_{\text{IC}\gamma}}{dE_\gamma d\Omega} = \frac{1}{E_\gamma} \int_{\text{l.o.s.}} ds \frac{j(E_\gamma, \vec{x}(s, b, \ell))}{4\pi}, \quad (4.10)$$

where $j(E_\gamma, \vec{x})$ denotes the photon emissivity at a position \vec{x} .

The emissivity depends on the spectrum of injected e^\pm , their energy losses in the Galactic medium, and the properties of the interstellar radiation field. Its explicit computation requires a detailed modeling of the Galactic environment and typically involves a numerical treatment. All the details have been already developed in the literature and can be found in ref. [26].

Finally, combining eq. (4.5) and (4.10) and integrating over the selected region of observation, the total flux of X-rays coming from DM annihilations is obtained:

$$\frac{d\Phi_{\text{DM}\gamma}}{dE_\gamma} = \int_{b_{\min}}^{b_{\max}} \int_{\ell_{\min}}^{\ell_{\max}} db d\ell \cos b \left(\frac{d\Phi_{\text{FSR}\gamma}}{dE_\gamma d\Omega} + \frac{d\Phi_{\text{IC}\gamma}}{dE_\gamma d\Omega} \right) \quad (4.11)$$

The integration boundaries $b_{\min, \max}$ and $\ell_{\min, \max}$ specify the region of the sky over which the signal is collected and depend on the particular observational strategy and field of view of the experiment under consideration.

In the next section we will compute our theoretical predictions for $\langle \sigma v \rangle$ within our model and compare them with the most recent ID constraints.

4.1.2 Limits on the Thermally-Averaged Annihilation Cross Section

In this section we derive constraints on the thermally averaged annihilation cross section $\langle \sigma v \rangle$ by comparing our prediction with the ID limits. In order to do so, we first need to specify how the thermally averaged cross section is evaluated.

In the Galactic environment, DM particles are highly non-relativistic, with typical velocities of order $v \sim \mathcal{O}(100) \text{ km/s}$. It is therefore well justified to work in the non-relativistic limit when computing the thermal average of the annihilation cross section.

The thermally averaged cross section (defined in chapter 3) can be expressed in terms of the Møller velocity. The Møller velocity is defined as

$$v_{\text{Møl}} = \sqrt{|v_1 - v_2|^2 - |v_1 \times v_2|^2}. \quad (4.12)$$

Here v_1 and v_2 denote the velocities of the two incoming particles, and are given by $v_1 = p_1/E_1$ and $v_2 = p_2/E_2$. Eq. (3.12) can thus be expressed in terms of the Møller velocity as:

$$\langle \sigma v \rangle = \frac{\int \sigma v_{\text{Møl}} e^{-E_1/T} e^{-E_2/T} d^3 p_1 d^3 p_2}{\int e^{-E_1/T} e^{-E_2/T} d^3 p_1 d^3 p_2}. \quad (4.13)$$

In the numerator, σ denotes the annihilation cross section for the process under consideration, as computed in the previous Chapter. This expression for the thermally averaged cross section coincides with the standard equation originally derived in ref. [35]. Moreover, following ref. [35], in the non-relativistic limit the thermal average can be rewritten in terms of the relative velocity $v_r = |v_1 - v_2|$. One finds that

$$\begin{aligned} \langle \sigma v \rangle_{n.r.} &= \int_0^\infty dv_r \sqrt{\frac{2}{\pi}} \left(\frac{m_\chi}{2T}\right)^{\frac{3}{2}} v_r^2 e^{\left(-\frac{m_\chi}{2T} \frac{v_r^2}{2}\right)} \sigma v_r \\ &= \int_0^\infty dv_r F_M(v_r) \sigma v_r \end{aligned} \quad (4.14)$$

The physical interpretation of this formula is straight-forward: in this non-relativistic regime, the thermal average reduces to an average over the relative velocity v_r of the annihilating particles. The corresponding distribution $F_M(v_r)$ has the same functional form as the Maxwell-Boltzmann distribution for the absolute velocity, with the particle mass replaced by the reduced mass $\mu = m_\chi/2$ and v_r replacing the single-particle velocity.

The computation of the annihilation cross section proceeds in close analogy with the calculation of $e^+e^- \rightarrow \chi\chi$ performed in sec. 3.3.2. The squared amplitude for the process $\chi\chi \rightarrow e^+e^-$ is the one derived in eq. 2.18. Inserting it into the standard $2 \rightarrow 2$ cross-section formula we obtain, in terms of the Mandelstam variable $\hat{s} = (p_{\chi_1} + p_{\chi_2})^2$

$$\sigma(\hat{s}) = \frac{g_\chi^2 g_e^2}{4\pi \hat{g}_\chi^2} \frac{\sqrt{\hat{s} - 4m_\chi^2} (\hat{s} - 4m_e^2)^{3/2}}{\hat{s} (\Gamma_X^2 m_X^2 + (m_X^2 - \hat{s})^2)}. \quad (4.15)$$

The Mandelstam variable \hat{s} can be rewritten in terms of the relative velocity v_r in the non-relativistic limit. A common way of doing this (see e.g. [35]) is to write $\hat{s} \simeq 4m_\chi^2 + m_\chi^2 v_r^2$. Substituting this relation in eq. (4.15), and expanding around $v_r \approx 0$ we obtain

$$\sigma v_r = \sigma_0 + \sigma_1 v_r^2 + \mathcal{O}(v_r^4), \quad \begin{cases} \sigma_0 \equiv 0, \\ \sigma_1 \equiv \frac{g_\chi^2 g_e^2 (m_\chi^2 - m_e^2)^{3/2}}{8\pi m_\chi (\Gamma_X^2 m_X^2 + (m_X^2 - 4m_\chi^2)^2)}. \end{cases} \quad (4.16)$$

We stress that, as expected, the leading s -wave contribution vanishes, $\sigma_0 = 0$.

Being σ_1 velocity-independent, we can derive the non relativistic limit of the thermally averaged cross section from eq. 4.14 as

$$\langle \sigma v \rangle_{\text{n.r.}} = \sigma_0 + \sigma_1 \langle v_r^2 \rangle \quad (4.17)$$

Here $\langle v_r^2 \rangle$ denotes the average of the squared relative velocity, computed with the Maxwell–Boltzmann distribution for the relative velocity $F_M(v_r)$ introduced above.

$$\langle v_r^2 \rangle = \int_0^\infty dv F_M(v_r) v_r^2, \quad F_M(v_r) = \sqrt{\frac{2}{\pi}} \left(\frac{\mu}{T}\right)^{3/2} v_r^2 \exp\left(-\frac{\mu}{T} \frac{v_r^2}{2}\right). \quad (4.18)$$

The integral can be evaluated analytically, yielding

$$\langle v_r^2 \rangle = \int_0^\infty dv \sqrt{\frac{2}{\pi}} \left(\frac{\mu}{T}\right)^{3/2} v_r^4 e^{-\frac{\mu v_r^2}{2T}} = \frac{3T}{\mu}. \quad (4.19)$$

In a halo the DM particles can be treated, to a good approximation, as a collisionless gas with Maxwell–Boltzmann velocity distribution. Associating the mean kinetic energy per particle, we can derive the halo temperature

$$\frac{1}{2} m_\chi v_0^2 = \frac{3}{2} k_B T_{\text{halo}}, \quad \Rightarrow \quad T_{\text{halo}} = \frac{m_\chi v_0^2}{3k_B}, \quad (4.20)$$

where v_0 is the characteristic velocity scale of the Standard Halo Model (typically $v_0 \simeq 220$ km/s for the Milky Way). Identifying T with T_{halo} in the expression above the average squared relative velocity becomes $\langle v_r^2 \rangle = 2v_0^2$.

A final remark concerns the resonant regime. Close to resonance, namely for $m_\chi \simeq m_X/2$, the non–relativistic expansion performed above is no longer valid and the full velocity dependence of the cross section must be retained. A detailed treatment of this case has been presented in ref. [36], where the annihilation cross section is written in terms of a narrow Breit–Wigner resonance as

$$\sigma \simeq \sigma_0 + \sigma_R \frac{\pi \Gamma}{2} \delta(E - E_R), \quad (4.21)$$

where E is the center–of–mass energy, E_R the resonant energy, and Γ the total width of the mediator. Performing the thermal average over a Maxwell–Boltzmann velocity distribution, the authors obtain the following analytic expression for the resonant contribution to the annihilation cross section for $m_\chi = m_X/2$

$$\langle \sigma v \rangle_R = \frac{2\pi^{1/2} v_R^2}{v_0^3} e^{-v_R^2/v_0^2} \sigma_R, \quad (4.22)$$

here v_R is the resonant velocity, defined as in [36]. For the numerical evaluation of the resonant cross section we adopt the same astrophysical velocity parameters discussed in ref. [36]. In particular, for the Milky Way halo we take again the characteristic velocity dispersion to be $v_0 = 220$ km/s.

We can now evaluate the non–relativistic thermally averaged annihilation cross section and study its dependence on the DM mass. We plot the resulting cross section and compare it with the

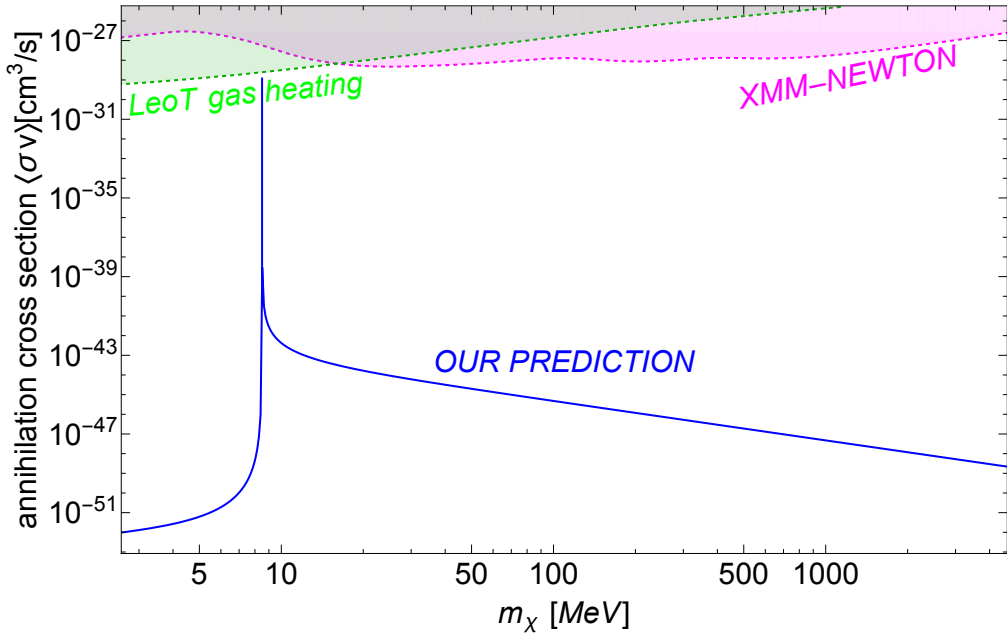


Figure 4.1 The experimental bound from indirect detection derived in the previous section (pink line) and the annihilation cross section predicted by our model. The green line is the bound derived from gas heating in the Leo-T dwarf galaxy.

experimental bound derived from indirect detection in the previous section, as shown in fig. 4.1. These limits are taken from the recent analysis of ref. [28], where the DM-induced X-ray signal was computed following the same phenomenological framework outlined in the previous section. The predicted flux is obtained by integrating the differential photon flux over the region of the sky observed by the instrument; in our notation, this corresponds to the expression in eq. (4.11), evaluated over the *XMM-Newton* field of view. In the framework considered here, where the relevant signal originates from DM annihilations into e^+e^- pairs, not all instruments contribute equally to the final constraint. Among the X-ray telescopes included in the analysis of ref. [28], the most constraining limit in the mass range of interest for our model is provided by *XMM-Newton*, and therefore sets the dominant bound shown in fig. 4.1.

The pink exclusion curve in fig. 4.1 is precisely the bound derived in ref. [28] from *XMM-Newton* data. It is obtained by requiring that the DM-induced X-ray flux predicted in this way does not exceed the observed emission in the corresponding region of the sky. These limits currently represent the most stringent constraints on annihilating DM for $m_\chi \gtrsim 11 \text{ MeV}$.

In addition to X-ray constraints, we also show in fig. 4.1 the limits derived from gas heating in the Leo-T dwarf galaxy. These bounds, indicated by the green curve, are obtained following

the analysis of [37], where the heating of the interstellar medium induced by DM annihilations is required not to exceed the observed gas cooling rate in Leo-T.

For what concerns the theoretical (blue) prediction, it is worth highlighting that it has been obtained by fixing the values of the NP couplings g_e and g_χ in accordance with the final results shown in fig. 3.4. The mass of the mediator has been also fixed as $m_X = 17$ MeV.

Figure 4.1 shows that the couplings determined through the freeze-in computations carried out in the previous Chapter are too tiny to be detected by current experiments. We expect that next-generation experiments will not be able to close the gap of more than 10 orders of magnitude between the blue and the green/pink curves. For this reason, in the next Section we will investigate whether our results can be, instead, compared with some low-energy data independent of astrophysics and cosmology.

4.2 Final Results: Bridging Cosmological with Low-Energy Data

In this section we will compare the results of the relic abundance computation within our theoretical framework with some complementary constraints coming from low-energy data.

Ref. [14] has recently analyzed several low-energy observables which can, indeed, constrain the coupling of the X -mediator to electrons (g_e) and its mass (m_X) in a largely model-independent way. Such quantities are related, for instance, to measurements of the anomalous magnetic moment of the electron [38], as well as to rare pion and muon decays [39–42]. Such a study has allowed the authors of ref. [14] to obtain several bounds in the plane (m_X, g_e) , which are reported in fig. 4.2 for reference and which constrain the parameter space of the hypothetical novel X_{17} -boson in a way which is complementary to the direct search carried out at PADME.

The main original point of this thesis is, as already stated in the previous chapters, to relate such X -boson particle to DM. As a direct consequence of this, at variance with ref. [14], we have to deal with more parameters, namely $(g_e, m_X, g_\chi, m_\chi)$. However, once some specific values are fixed for the DM mass m_χ and its coupling to the X -mediator g_χ , we will be able to directly compare the predictions of our freeze-in computations with the low-energy constraints computed in ref. [14] and shown in fig. 4.2.

It is clear that the chosen values of m_χ and g_χ have to be consistent with the condition

$$\Omega_{\text{DM}} h^2(g_e, m_X, g_\chi, m_\chi) = 0.12, \quad (4.23)$$

namely with the requirement that the abundance of DM produced within our framework matches the observations by Planck [8].

As discussed in sec. 3.4, the freeze-in production of DM in our framework naturally separates into two qualitatively different regimes, depending on the hierarchy between the mediator mass and twice the DM mass. These two regimes lead to distinct phenomenological behaviors and therefore to different implications when the relic-abundance requirement (eq. (4.23)) is combined with the low-energy constraints in fig. 4.2.

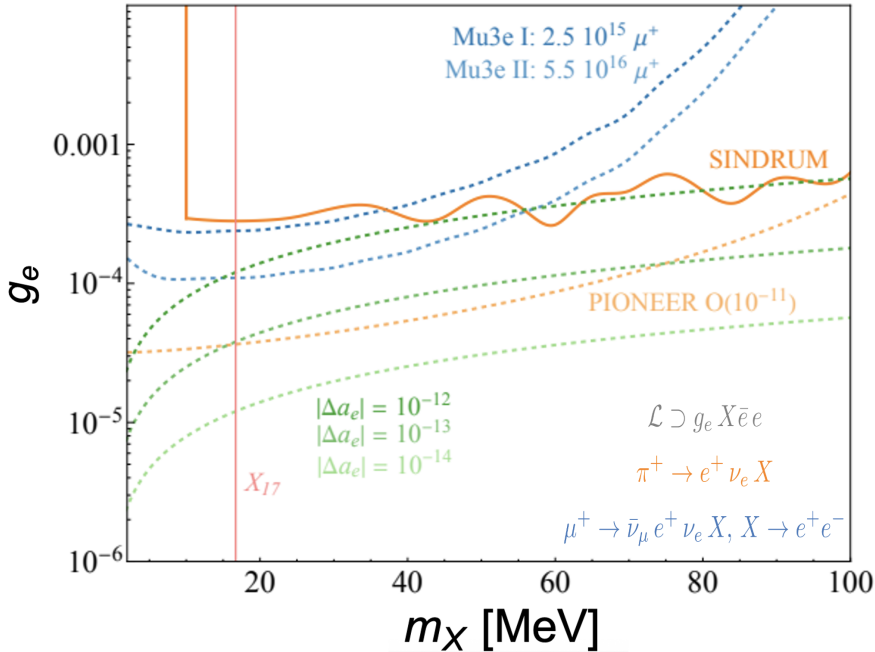


Figure 4.2 Exclusion plot for a scalar X -mediator, taken from ref. [14]. The solid curve corresponds to the current experimental limit, while the dashed curves indicate projected sensitivities of future experiments.

Non-Resonant Phenomenology

We begin by considering the non-resonant regime, in which $m_\chi > m_X/2$ and DM production is dominated by the off-shell process $e^+e^- \rightarrow \chi\chi$ rather than by on-shell mediator decays. This scattering is particularly interesting, since it is controlled not only by the DM coupling g_χ , but also by the electron coupling g_e , which is precisely the parameter constrained by the low-energy observables studied in ref. [14].

We proceed as follows: for fixed values of the dark sector coupling, (m_χ, g_χ) , we impose the relic-abundance condition

$$\Omega_{\text{DM}} h^2(m_\chi, g_\chi, m_X, g_e) = 0.12, \quad (4.24)$$

which identifies a curve in the (m_X, g_e) plane. These curves can then be directly overlaid on the exclusion plot of ref. [14]. In this way, the regions already excluded by low-energy measurements immediately translate into excluded portions of the parameter space of our DM model. In this sense, the low-energy constraints on g_e are effectively projected onto the dark sector, resulting in quantitative bounds on the strength of the χ - X interaction. The outcome of this procedure is illustrated in fig. 4.3, where the curves obtained from the condition above are superimposed onto the low-energy bounds of ref. [14].

In this plot we fix the DM mass to $m_\chi = 35$ MeV and consider four representative benchmark values of the DM coupling, namely $g_\chi = 10^{-9}, 10^{-8}, 10^{-7}$ and 10^{-6} . Each of these values defines a distinct freeze-in contour in the (m_X, g_e) plane, which can then be directly compared with the

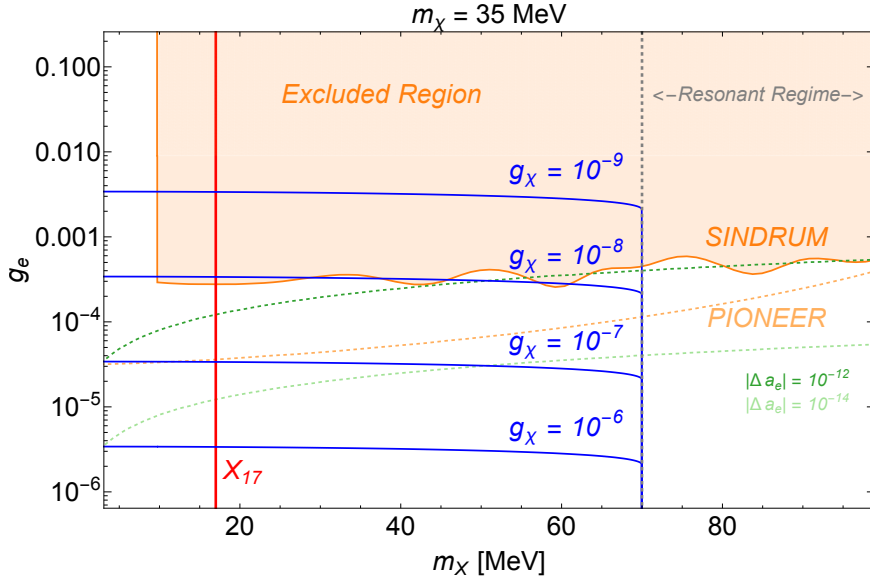


Figure 4.3 The orange solid band is the exclusion region on the $g_e - m_X$ plane coming from SINDRUM on $\pi^+ \rightarrow e^+ \nu_e X$ experiment, as computed in ref [14]. The orange and green dashed lines correspond to exclusion limits expected from next-generation experiments, as discussed and obtained in ref. [14]. The solid blue lines are the final results of our computations and show the values of g_e that reproduce the observed DM relic abundance via freeze-in, by fixing $m_\chi = 35$ MeV and by selecting some benchmark values of the coupling g_χ . The most important message of this plot is that, quite interestingly, the combination of the relic abundance and SINDRUM constraint yields a highly non-trivial information: if $m_\chi = 35$ MeV, then a lower bound on the NP coupling g_χ exists, namely $g_\chi \gtrsim 10^{-8}$. Such a lower bound may be even higher, as the projections by next-generation experiments suggest. The vertical gray dashed line at $m_X = 2m_\chi$ marks the transition between the non-resonant and resonant production regimes.

experimental exclusion regions.

We have also verified that varying the DM mass does not qualitatively modify the structure of the analysis. Changing m_χ mainly shifts the boundary between the resonant and non-resonant regimes, increasing or reducing the range of allowed values of the mediator mass m_X , but it does not alter the qualitative behavior of the freeze-in curves. As a consequence, the dominant phenomenological quantity in this regime is the DM coupling g_χ , which effectively controls the overall phenomenology of the relic-abundance curves, while m_χ only plays a secondary role by selecting the available kinematic domain.

The negligible dependence on the DM mass implies that the relevant phenomenological information in the (m_X, g_e) plane can be directly translated into constraints on the coupling g_χ . From the overlaid blue curves in fig. 4.3 one immediately observes that, in the non-resonant regime, the most stringent

constraint currently arises from the SINDRUM bound on $\pi^+ \rightarrow e^+ \nu_e X$ [39, 40]. When projected onto our freeze-in curves, this exclusion region translates into a lower limit on the dark-sector coupling

$$g_\chi \gtrsim 10^{-8}. \quad (4.25)$$

Up to now we have implicitly assumed that freeze-in production mediated by the X boson is the sole mechanism responsible for the present DM abundance. This leads to the equality condition $\Omega_{\text{DM}} h^2 = 0.12$. However, this hypothesis can be relaxed. If additional DM production mechanisms are present, the only robust requirement is that X -mediated freeze-in does not *overproduce* dark matter. In this case the relic-density condition becomes an inequality,

$$\Omega_{\text{DM}}^{(X)} h^2(m_\chi, g_\chi, m_X, g_e) \leq 0.12, \quad (4.26)$$

where $\Omega_{\text{DM}}^{(X)}$ denotes the contribution generated via X -mediated processes only. The boundary of this region is still given by the usual freeze-in curve satisfying $\Omega_{\text{DM}} h^2 = 0.12$, while the parameter space above it is excluded because it would lead to an excess of dark matter.

This situation is illustrated in fig. 4.4, where, for definiteness, we fix $m_\chi = 45$ MeV and $g_\chi = 10^{-7}$. The solid line corresponds to the parameter combinations reproducing the observed relic abundance, whereas the shaded area indicates the region excluded by DM overproduction.

It is worth emphasizing that this represents a genuinely new step with respect to ref. [14]. While that work constrained the parameter space of a light boson coupled to electrons in a largely model-independent way, here we embed the same mediator into a concrete DM scenario and show how their low-energy observables constrains the DM coupling itself. In other words, we are comparing a DM model not previously explored in the literature, with the set of precision low-energy probes developed in ref. [14].

Resonant Phenomenology

We now turn to the resonant regime, defined by $m_\chi < m_X/2$, in which DM is predominantly produced via on-shell decays of the mediator, $X \rightarrow \chi\chi$. As discussed in sec. 3.4, in this regime the scattering contribution is equivalent to production through on-shell decays of the mediator and is therefore not included explicitly in order to avoid double counting. As a consequence, the relic abundance is entirely controlled by the decay width $\Gamma_{X \rightarrow \chi\chi}$. An important consequence is that the freeze-in abundance no longer depends on the electron coupling g_e , but only on the dark-sector parameters (m_χ, g_χ) and on the mediator mass m_X .

Therefore, imposing the relic-abundance condition (eq. (4.23)) does not select a curve in the (m_X, g_e) plane as in the non-resonant case. Instead, for fixed (m_χ, g_χ) we expect a unique value of the mediator mass m_X . In the (m_X, g_e) plane this corresponds to a vertical line, reflecting the fact that the relic density is insensitive to g_e in this production regime.

In order to recover phenomenological sensitivity to the low-energy plane (m_X, g_e) , we relax again the assumption that freeze-in through the X_{17} mediator is the *only* mechanism responsible for DM production. The relic-density condition therefore becomes the inequality from eq. (4.26).

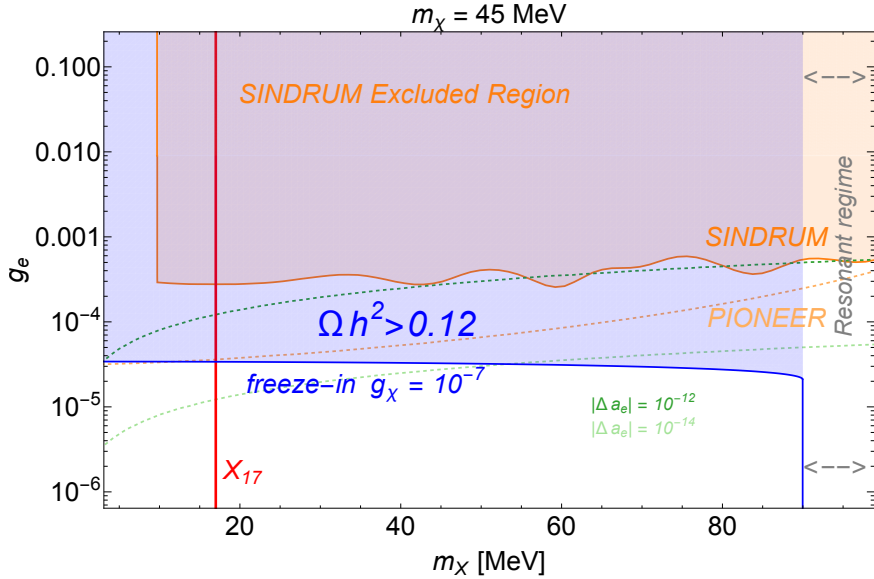


Figure 4.4 Freeze-in curve reproducing the observed relic abundance for $m_\chi = 45$ MeV and $g_\chi = 10^{-7}$ (solid line). The shaded region above the curve is excluded because it would lead to DM overproduction, corresponding to the condition $\Omega_{\text{DM}} h^2 > 0.12$. The vertical gray dashed line at $m_X = 2 m_\chi$ marks the transition between the non-resonant and resonant production regimes.

In order to make the phenomenology of this regime fully explicit, it is necessary to examine the functional dependence of the relic abundance on the X mass, in the resonant case, where DM production is dominated by on-shell decays $X \rightarrow \chi\chi$. Imposing the relic-abundance condition

$$\Omega_{\text{DM}} h^2(m_X) = 0.12 \quad (4.27)$$

one finds that, in the resonant regime, this equation typically admits *two* distinct solutions for the mediator mass m_X . The origin of this behaviour is not entirely trivial and is worth commenting on it.

Since from eq. (3.26) $Y_\chi \propto \Gamma_{X \rightarrow \chi\chi} = (m_X^2 - 4m_\chi^2)^{3/2}/m_X^2$, one may naively expect the relic abundance to increase monotonically with m_X , enhancing the efficiency of DM production. However, besides the growth of the decay rate, one must also take into account the cosmological dilution of the produced particles. To properly assess this effect, it is useful to recall a key feature of the freeze-in mechanism: DM is mainly produced at temperatures of the order of the mass of the heaviest particle involved in the process. Therefore, increasing m_X also shifts the production epoch to earlier times, corresponding to higher temperatures. The Hubble rate scales as $H(T) \propto T^2 \sim m_X^2$ in correspondence of the DM production epoch, so production occurring at higher temperatures experiences a stronger Hubble expansion and hence a stronger dilution. This interplay can be

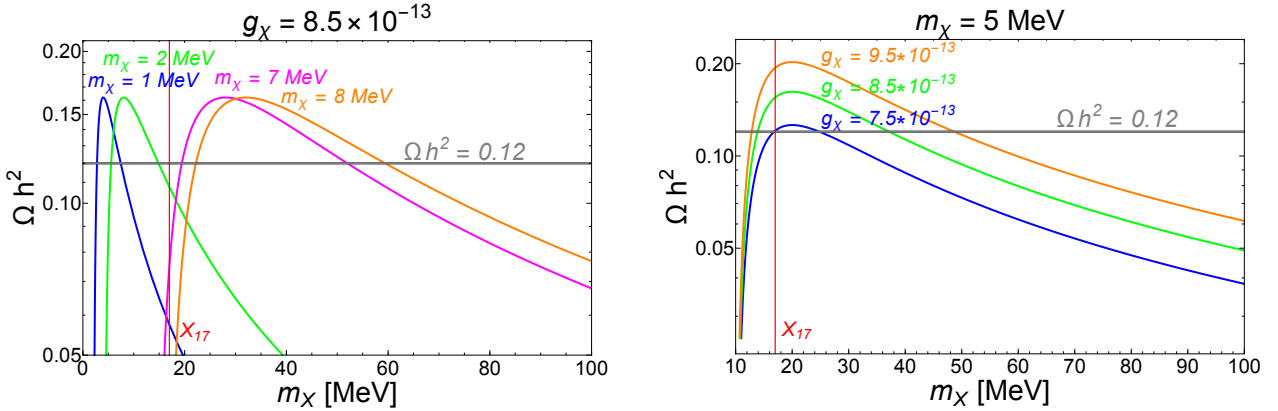


Figure 4.5 Relic abundance in the resonant regime as a function of the mediator mass m_X . The horizontal dashed line denotes the observed value $\Omega_{\text{DM}}h^2 = 0.12$, while the vertical red line corresponds to $m_X = 17$ MeV associated with the X_{17} hypothesis. In the left panel we fix the coupling to $g_\chi = 8.5 \times 10^{-13}$ and show the dependence on the mediator mass for four representative DM masses, $m_\chi = 1, 2, 7$ and 8 MeV. In the right panel instead we fix the DM mass to $m_\chi = 5$ MeV and plot the relic abundance for three benchmark values of the dark-sector coupling, namely $g_\chi = 7.5 \times 10^{-13}, 8.5 \times 10^{-13}$ and 9.5×10^{-13} .

appreciated more transparently by rewriting the mediator–mass and temperature dependence of the freeze–in abundance as

$$Y_\chi(m_X) \propto \frac{\Gamma_{X \rightarrow \chi\chi}}{H} \propto \frac{\Gamma_{X \rightarrow \chi\chi}}{T^2} \sim \frac{(m_X^2 - 4m_\chi^2)^{3/2}}{m_X^4}, \quad (4.28)$$

which is precisely the scaling in eq. (3.26).

As a consequence, increasing m_X has two competing effects: on the one hand the decay rate grows, enhancing production; on the other hand, the earlier production time increases the expansion rate and suppresses the final abundance.

The interplay between these effects leads to a maximum of $\Omega_{\text{DM}}h^2(m_X)$, so that the relic–abundance condition may be satisfied on both sides of this maximum, giving rise to two solutions for m_X . The qualitative behavior described above is illustrated in fig. 4.5. In both plots we show the relic abundance as a function of the mediator mass. The horizontal line corresponds to the observed value $\Omega_{\text{DM}}h^2 = 0.12$, while the vertical red line marks the value $m_X = 17$ MeV associated with the X_{17} hypothesis.

Unlike the non-resonant case, here both g_χ and m_χ are active parameters in the sense that variations in either of them significantly affect the resulting phenomenology. For this reason, we present two complementary plots: one in which the DM mass is kept fixed while the coupling is varied, and one in which the coupling is fixed and the DM mass is varied. This allows us to separately assess the phenomenological impact of each parameter.

In the left panel we fix the coupling to $g_\chi = 8.5 \times 10^{-13}$ and show the dependence on the mediator mass for four representative DM masses, $m_\chi = 1, 2, 7$ and 8 MeV. In the right panel we instead

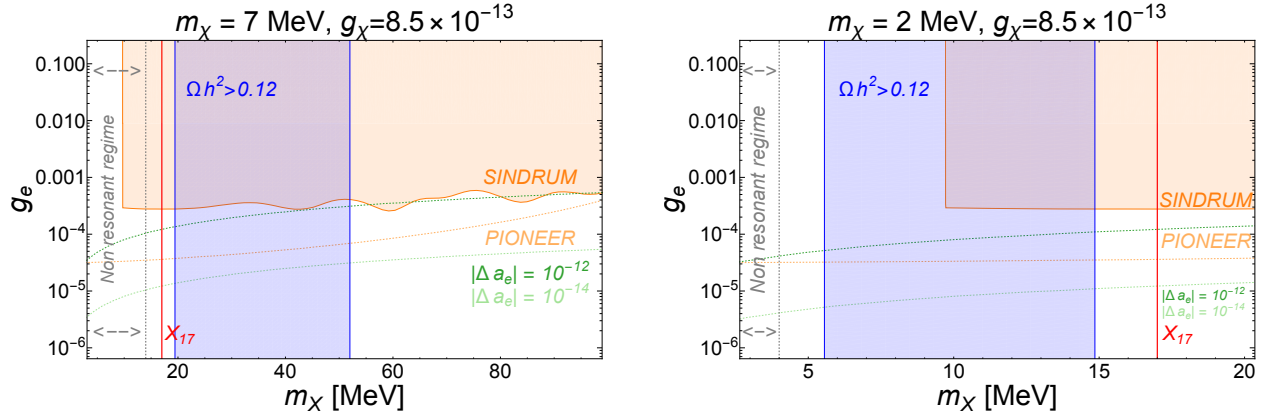


Figure 4.6 Overlay of the regions excluded by DM overproduction on top of the low-energy constraints of ref. [14] for the two benchmark scenarios described in the text. In the left panel the relic abundance is reproduced in the narrow kinematic-increase region close to $m_X \simeq 2m_\chi$, for $m_\chi = 7$ MeV and $g_\chi = 8.5 \times 10^{-13}$. In the right panel the correct relic density is obtained on the high-mass branch, for $m_\chi = 2$ MeV and the same coupling $g_\chi = 8.5 \times 10^{-13}$. The vertical gray dashed line at $m_X = 2m_\chi$ marks the transition between the non-resonant and resonant production regimes.

fix the DM mass to $m_\chi = 5$ MeV and plot the relic abundance for three benchmark values of the dark-sector coupling, namely $g_\chi = 7.5 \times 10^{-13}$, 8.5×10^{-13} and 9.5×10^{-13} .

It is worth stressing that, in contrast with the non-resonant regime, varying the coupling g_χ in the resonant case does modify the qualitative behavior of the curves. The dependence is extremely sharp: the relic-abundance curves in fig. 4.5 are highly sensitive to small changes in g_χ , which is in practice confined to a rather narrow interval, $g_\chi \sim (0.7-1) \times 10^{-12}$, as clear from Figure 3.4. Within this range even modest variations of g_χ can shift the position of the maximum or remove one of the two solutions entirely. When replacing the relic-density condition with the inequality in eq. (4.26), the requirement becomes simply that freeze-in production through the X mediator does not exceed the DM present in the Universe. As a consequence, instead of selecting isolated solutions, the allowed parameter space splits into two distinct regions.

A first, narrow allowed band appears close to threshold, where the relic abundance increases due to the kinematic increase of the decay rate, and is therefore confined around $m_X \gtrsim 2m_\chi$, hence this region is strongly controlled by the DM mass. A second, much broader allowed region emerges at larger mediator masses. In this domain the decrease driven by cosmological dilution opens up an extended parameter region that satisfies the non-overproduction condition.

To make this structure explicit, we overlay in fig. 4.6 the exclusion regions obtained from the non-overproduction condition on the low-energy plane (m_X, g_e) already constrained in ref. [14]. For illustration, we consider two benchmark cases chosen such that the X_{17} mass, $m_X = 17$ MeV, lies in different parts of the allowed region.

In the first case (left panel), we take $m_\chi = 7$ MeV and $g_\chi = 8.5 \times 10^{-13}$. For these values, the point $m_X = 17$ MeV falls within the narrow region close to threshold, where the relic abundance is

mainly controlled by the kinematic increase of the decay rate. The corresponding band allowed by the non-overproduction condition is plotted on top of the low-energy constraints of ref. [14].

In the second case (right panel), we keep the coupling fixed at $g_\chi = 8.5 \times 10^{-13}$ but choose a lighter DM mass, $m_\chi = 2$ MeV. In this configuration the same value $m_X = 17$ MeV lies instead on the broader, high-mass side of the curve, where the relic density is dominated by cosmological dilution. The corresponding exclusion region from DM overproduction is again superimposed on the (m_X, g_e) plane. In this way, both the threshold and dilution-dominated solutions associated with the X_{17} mass are directly compared with the existing low-energy bounds.

To summarize, in this section we have combined the relic-abundance requirement with the low-energy bounds in the (m_X, g_e) plane. In the non-resonant regime, where DM is produced through off-shell scatterings, this comparison directly constrains the dark-sector coupling, leading to a robust lower bound $g_\chi \gtrsim 10^{-8}$. In the resonant regime, instead, DM is mainly produced from on-shell X decays and the phenomenology is qualitatively different: the relic abundance becomes highly sensitive to the mediator mass and may admit two distinct solutions. Relaxing the assumption that X -mediated freeze-in is the only production mechanism, the non-overproduction condition selects two allowed regions, associated respectively with the kinematic increase near threshold and with the dilution-dominated branch at larger m_X .

Chapter 5

Conclusions

This thesis examined whether a light boson with a mass of order 17 MeV, motivated by the recent e^+e^- excess observed by PADME, can serve as a mediator between the SM and a minimal dark sector. DM remains one of the principal unresolved experimental puzzles of the Universe. Thus, although the experimental picture of 17 MeV resonance is still evolving, it is valuable from a theoretical point of view to scrutinize the available data and relate it to the broader DM puzzle. The confirmation of such a particle would not only represent a major breakthrough but could also open a novel pathway toward addressing one of the central outstanding inconsistencies of the SM: the nature and origin of DM.

Firstly, in Chapter 1 we outline the structure of the SM and review the experimental evidence supporting the existence of DM. We then introduce the main motivation for this thesis, summarizing the current status of the hints for a 17 MeV resonance reported by PADME and, earlier, by ATOMKI in nuclear transitions.

In Chapter 2, we construct an EFT framework extending the SM with a real scalar mediator X , a Majorana fermion χ , and a right-handed neutrino ν_R . We classify all gauge-invariant operators up to dimension six that couple these new states to SM fields, providing a systematic basis for the phenomenological analysis developed in the subsequent chapters. To be more specific, we define a minimal benchmark scenario of interest for phenomenology, namely the one in which the X mediator is a real scalar singlet and the DM particle χ coincides with the right-handed neutrino ν_R .

In Chapter 3, we apply this EFT to the early Universe, studying DM production through the freeze-in mechanism. Using analytic limits of the Boltzmann equation, we identify viable regions of parameter space in which thermal decays of DM reproduce the observed relic abundance.

In Chapter 4, we assess whether astrophysical ID probes can further constrain the model. Freeze-in generally implies the presence of weak couplings, which, indeed, are too tiny to be detected by existing ID experiments. However, our DM model remains testable with current and future low-energy observables and data, such as measurements of the anomalous magnetic moment of the electron, as well as of rare muon and pion decays.

The central outcomes of our analysis are presented in Figs. 4.3- 4.6 of Sec. 4.2, where we combine

the cosmological constraints derived in this work with the existing low-energy bounds—such as those from the electron anomalous magnetic moment and from rare muon and pion decays—reported in ref [14]. This unified picture offers the most comprehensive assessment to date of the viable parameter space for the X_{17} -mediated dark-sector scenario explored here.

Taken together, our results demonstrate that a light MeV-scale mediator—such as the hypothesized X_{17} —can be incorporated into a minimal and gauge-invariant extension of the SM, can be produced through thermal decays in a way that matches the observed relic abundance, and can remain compatible with a broad set of experimental astrophysical bounds, such as indirect detection. Such a mediator can offer a promising route toward unraveling the longstanding mystery of DM. The EFT framework ensures that these conclusions are not tied to any specific ultraviolet completion, while maintaining predictive power and internal consistency.

The originality of the work presented in this thesis can be summarized as follows. In cap. 2, the operator tables and all amplitude calculations are original and work out for this specific project. In cap. 3, sec. 3.3 includes the original computations (in particular sec. 3.3.2); the approximations in sec. 3.4 and the numerical comparisons in the Appendix C are fully original. In cap. 4, sec. 4.1.2 is original. All the figures 4.3-4.6, inspired by the bounds in Figure 4.2 (as computed in ref. [14]), would similarly contribute new original material.

Several extensions can follow from this thesis and are necessary to ultimately prepare it for publication. A more complete EFT could include couplings to quarks, which would be essential for a unified interpretation of the ATOMKI anomalies. Future PADME runs will further clarify the spin of the mediator through improved sensitivity to the decay channel $X_{17} \rightarrow \gamma\gamma$. Moreover, while freeze-in scenarios typically imply extremely small interaction strengths, the presence of a light (\sim MeV-scale) mediator can enhance scattering at very low recoil energies, opening a window for DM direct detection. It will therefore be useful to investigate this type of measurements in the near future to further constrain the parameter space identified in this thesis.

Appendix A

Neutrino Coupling

In this Appendix we will focus on the terms from the interaction Lagrangian (eq. (2.9)) that induce couplings of the dark fermion χ to active neutrinos, either directly or via mixing.

Our goal is to provide a qualitative but comprehensive discussion of their phenomenological implications. We show that astrophysical observations impose extremely stringent constraints on such interactions. These include, in particular, bounds from the stability of dark matter, limits on neutrino masses and mixing, and constraints from indirect detection. As a consequence of these considerations, the couplings appearing in the neutrino sector must be strongly suppressed, which justifies neglecting them in the main body of the thesis.

In our model, the SM neutrino may interact with the dark fermion χ in two distinct ways:

- firstly, through the Yukawa-like term

$$y_{mix} \bar{\ell} \tilde{H} \chi \xrightarrow{\text{EWSB}} \theta m_\chi \bar{\nu}_L \chi \quad (\text{A.1})$$

which induces a mixing between ν_L and χ , recall that θ is the parameter introduced in eq. (2.10);

- secondly, through a trilinear interaction

$$\frac{\hat{g}_{XDM\nu}}{\Lambda} X \bar{\ell} \tilde{H} \chi \xrightarrow{\text{EWSB}} g_\nu X \bar{\nu}_L \chi. \quad (\text{A.2})$$

As already discussed, these terms might allow DM to decay, undermining DM stability. However, a variety of experimental and observational inputs point towards extremely suppressed θ and g_ν , as we will show in this section. These results strongly disfavor neutrino interactions with our dark sector and, then, favor a portal-like interaction between the dark and the SM sectors. A theoretical explanation of the smallness of these couplings may rely on the introduction of an ad hoc discrete Z_2 symmetry that protects the dark sector, forbids the problematic operators, and at the same time stabilizes the DM candidate χ .

A.1 Neutrino mixing term

We are first considering the mixing term. Focusing our attention on eq.(A.1), there are three main experimental pieces of evidence to show why θ is ultra-suppressed: neutrino mass, DM lifetime and X-ray bounds.

The first handle comes from neutrino mass measurements. The most precise one comes from cosmology. It concerns the sum of the masses of three generations of neutrinos and it is taken from Ref. [43]

$$\sum_{\nu} m_{\nu} < 0.071 \text{ eV}. \quad (\text{A.3})$$

In particular, the mixing between the SM neutrino and the Majorana fermion χ induced by the dark-sector Lagrangian generates an additional contribution to the light neutrino mass. To make this explicit, it is useful to isolate from \mathcal{L}_{DS} the pieces that control the neutrino– χ mass mixing:

$$\mathcal{L}_{DS} \supset -\frac{1}{2} \hat{m} \bar{\chi}^c \chi + y_{mix} \bar{\ell} \tilde{H} \chi + \text{h.c.} \quad (\text{A.4})$$

After electroweak symmetry breaking, these terms generate a 2×2 mass matrix in the (ν_L, χ) basis:

$$\mathcal{L}_{DS}^{Broken} \supset -\frac{1}{2} \begin{pmatrix} \bar{\nu}_L & \bar{\chi}^c \end{pmatrix} \begin{pmatrix} 0 & y_{mix} \frac{v}{\sqrt{2}} \\ y_{mix} \frac{v}{\sqrt{2}} & \hat{m} \end{pmatrix} \begin{pmatrix} \nu_L \\ \chi \end{pmatrix} + \text{h.c.} \quad (\text{A.5})$$

We assume the limit $\hat{m} \gg y_{mix} v / \sqrt{2}$, which is naturally expected in a seesaw–like setup. Even in scenarios with relatively light DM, this approximation remains consistent provided that y_{mix} can be taken sufficiently small. In this sense, we can safely use the cosmological neutrino–mass bound to derive a conservative upper limit on y_{mix} . The mass matrix can be diagonalised perturbatively. To leading order one finds:

$$\begin{aligned} m_{\chi} &= \hat{m} \\ \Delta m_{\nu} &= \frac{y_{mix}^2 v^2}{2 \hat{m}} \end{aligned} \quad (\text{A.6})$$

corresponding to the physical mass of χ and a correction to the SM neutrino mass.

Using eq. (A.6), it is convenient to express the correction to the neutrino mass in terms of the active–sterile mixing angle:

$$\Delta m_{\nu} \simeq \theta^2 m_{\chi}. \quad (\text{A.7})$$

Requiring this contribution not to exceed the cosmological bound on the sum of neutrino masses, $\Delta m_{\nu} \lesssim \sum_{\nu} m_{\nu}$, immediately gives

$$\theta \lesssim \sqrt{\frac{\sum_{\nu} m_{\nu}}{m_{\chi}}} \quad \Rightarrow \quad \theta \lesssim 2.7 \times 10^{-4} \sqrt{\frac{\text{MeV}}{m_{\chi}}} \quad (\text{A.8})$$

A much stronger constraint on θ may, instead, arise from the requirement of dark matter stability, namely from the condition that the lifetime of the DM particle χ must be at least comparable to the

age of the Universe, $T_U \simeq 10^{18}$ s, so that it does not decay away on cosmological time scales. The total decay width Γ_χ is related to the lifetime by

$$\tau_\chi = \Gamma_\chi^{-1}, \quad (\text{A.9})$$

and the stability requirement can be written as

$$\tau_\chi \gtrsim T_U \iff \Gamma_\chi T_U \lesssim 1. \quad (\text{A.10})$$

To illustrate how this translates into a bound on the active–sterile mixing angle θ , let us consider a simple benchmark mass range. For $m_\chi < m_e$ the dominant decay channel is into SM neutrinos ($\chi \rightarrow 3\nu$) with the decay width given by [6]

$$\Gamma(\chi \rightarrow 3\nu) = \frac{G_F^2 m_\chi^5}{96\pi^3} \theta^2 \approx \frac{\theta^2}{33 T_U} \left(\frac{m_\chi}{\text{keV}} \right)^5, \quad (\text{A.11})$$

where G_F is the Fermi constant, and T_U denotes the age of the Universe.

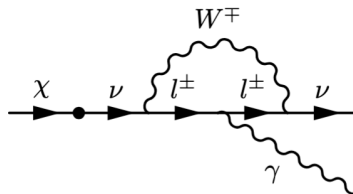
Putting together the expression in eq. (A.11) with the dark–matter stability requirement $\Gamma_\chi T_U \lesssim 1$ requirement in eq. (A.10), we obtain the following upper bound on the active–sterile mixing angle

$$\theta \lesssim 2 \times 10^{-7} \left(\frac{\text{MeV}}{m_\chi} \right)^{5/2} \quad (\text{A.12})$$

The stability bound above is stronger than the one derived from neutrino masses.

We remark that the estimate above has been obtained assuming $m_\chi < m_e$, so that only invisible decays into neutrinos are kinematically accessible. If the dark–matter particle were instead heavier than the electron, additional decay channels would open up, mediated by the same active–sterile mixing. In this case, charged final states particles would unavoidably produce photons, either via final-state radiation or inverse Compton scattering on ambient radiation fields. Such electromagnetic signatures are much more tightly constrained observationally than purely neutrino final states, in particular by X-ray and gamma-ray telescopes. As a consequence, once $m_\chi > m_e$ the corresponding bounds on the lifetime of χ become even stronger than those discussed above, implying an even more severe upper limit on the active–sterile mixing angle θ . Therefore, the constraint in Eq. (A.11) should be regarded as conservative, and neutrino couplings must in general be extremely suppressed throughout the entire mass range of interest.

Finally, the most significant bounds come from decay modes involving photons, since photons are easy to detect. The dominant such channel in this case is at one loop, namely $\chi \rightarrow \nu \gamma$, arising, for example, from the following diagram:



The corresponding decay width is (see Ref. [44])

$$\Gamma(\chi \rightarrow \nu\gamma) = \frac{9\alpha G_F^2 m_\chi^5}{256\pi^4} \theta^2 \approx \frac{\theta^2}{4250 T_U} \left(\frac{m_\chi}{\text{keV}} \right)^5, \quad (\text{A.13})$$

where α is the usual electromagnetic fine-structure constant $\alpha \approx \frac{1}{137}$. Very roughly, current X-ray observations (see [45–47]) require

$$\tau_\chi \text{BR}(\chi \rightarrow \nu\gamma) = \frac{1}{\Gamma(\chi \rightarrow \nu\gamma)} \gtrsim 10^8 T_U, \quad (\text{A.14})$$

i.e. the lifetime associated to the radiative decay channel must exceed the age of the Universe by at least eight orders of magnitude.

Imposing this X-ray lifetime bound on the decay rate immediately translates into the following upper limit on the active–sterile mixing angle:

$$\theta \lesssim 2 \times 10^{-10} \left(\frac{\text{MeV}}{m_\chi} \right)^{5/2}. \quad (\text{A.15})$$

In summary, the active–sterile mixing angle θ is forced to be very small by three independent considerations: *i*) correction to the light neutrino mass induced by a seesaw-like mechanism; *ii*) requirement of DM stability; *iii*) constraints by X-ray observations. Taken together, these arguments point to an ultra-suppressed mixing. In particular, taking the most stringent constraint – the one from X-ray observations – we find $\theta \lesssim 10^{-10}$ for a $\mathcal{O}(\text{MeV})$ DM mass.

As a side remark, we note that such tiny mixing also implies that the contribution of χ to active neutrino masses, $m_\nu^{(\chi)} \simeq \theta^2 m_\chi$, is well below the largest measured neutrino mass splittings. In other words, the observed neutrino masses must predominantly arise from additional mechanisms beyond the simple seesaw induced by the dark-matter state.

A.2 Neutrino pseudo-Yukawa term

We now turn to the phenomenology of the pseudo–Yukawa interaction

$$\frac{\hat{g}_{XDM\nu}}{\Lambda} X \bar{\ell} \tilde{H} \chi \xrightarrow{\text{EWSB}} g_\nu X \bar{\nu}_L \chi, \quad (\text{A.16})$$

and we will show, in close analogy with the mixing term discussion, that the coupling g_ν is also strongly constrained and effectively suppressed.

Firstly we will discuss the case in which the DM mass is larger than the mediator mass ($m_\chi > m_X$). The opposite hierarchy ($m_\chi < m_X$) leads to an entirely similar phenomenological picture and will not be treated explicitly here. In both situations existing experimental bounds force the coupling g_ν to be extremely small.

In the first regime, DM can decay via the two–body channel $\chi \rightarrow \nu X$, mediated by the coupling in eq. (A.2). If we assume this to be the dominant decay mode of χ , the corresponding decay width is

$$\Gamma(\chi \rightarrow \nu X) = \frac{g_\nu^2}{16\pi} m_\chi \left(1 - \frac{m_X^2}{m_\chi^2} \right)^2, \quad (\text{A.17})$$

where we have neglected the SM neutrino mass.

As discussed above, DM stability on cosmological time-scales requires its lifetime to exceed the age of the Universe,

$$\tau_\chi \gtrsim T_U \quad \Longleftrightarrow \quad \Gamma_\chi T_U \lesssim 1. \quad (\text{A.18})$$

Identifying $\Gamma_\chi \simeq \Gamma(\chi \rightarrow \nu X)$ and inserting eq. (A.17), we obtain the bound

$$g_\nu \lesssim \sqrt{\frac{16\pi}{m_\chi T_U \left(1 - \frac{m_X^2}{m_\chi^2}\right)^2}}. \quad (\text{A.19})$$

Thus, in the regime $m_\chi > m_X$, DM stability forces the pseudo-Yukawa coupling g_ν to be very small, especially when the mass splitting between χ and X is not too close to threshold ($m_\chi \gg m_X$).

This bound is already extremely strong, roughly:

$$g_\nu \lesssim 10^{-20} \sqrt{\frac{\text{MeV}}{m_\chi}}. \quad (\text{A.20})$$

The discussion above shows that both sources of neutrino interactions with the dark sector the mixing term and the pseudo-Yukawa coupling are subject to extremely stringent phenomenological constraints.

In the case of mixing, the requirements coming from neutrino masses, DM stability and the absence of X-ray lines all force the mixing angle to be ultra-suppressed, $\theta \lesssim 10^{-10}$ for MeV-scale dark matter. Similarly, the pseudo-Yukawa coupling g_ν is constrained by the stability bound on χ , leading to values as small as $g_\nu \lesssim 10^{-20}$ in the relevant mass range.

Such tiny couplings have no observable impact on the dark-sector phenomenology discussed in the main text. For this reason, throughout the thesis we consistently neglect neutrino interactions with the dark fermion χ and the mediator X , concentrating instead on the dominant couplings to electrons which control both the freeze-in production and the experimental signatures of the model.

Appendix B

UV Completion

In this appendix we introduce and discuss in a synthetic way a possible ultraviolet (UV) completion of the effective theory discussed in Chapter 2.

An immediate issue that emerges in this context concerns the couplings between the dark sector and neutrinos. As discussed in Appendix A, interactions of the dark fermion χ with SM neutrinos are subject to extremely stringent bounds coming from cosmology, indirect detection and neutrino-mass constraints. These considerations imply that all the operators in Lagrangian (2.7) inducing sizeable χ -neutrino couplings must be highly suppressed, or absent altogether, in a realistic UV completion. A simple and economical way to account for this suppression is to invoke a discrete Z_2 symmetry acting on the dark sector under which all SM particles and the X_{17} boson are even while the DM particle χ is odd.

The renormalizable terms involving the dark fermion χ at low energy (i.e. after EWSB) are

$$\mathcal{L}_\chi = \bar{\chi} i\gamma_\mu \partial^\mu \chi - \frac{m_\chi}{2} \bar{\chi}^c \chi + g_\chi X \bar{\chi}^c \chi + \text{h.c.} \quad (\text{B.1})$$

The last term of (B.1) is one of the two key ingredients that generate the coupling between the dark matter and the mediator X . The other ingredient, responsible for inducing the coupling of X to electrons in the low-energy model discussed in section 2.2, derives from the non-renormalizable operator

$$\mathcal{L}_{Xee}^{\text{eff}} = \frac{g_{Xee}}{\Lambda} X_{17} \bar{\ell} H e_R + \text{h.c.} \quad (\text{B.2})$$

This dimension-5 operator, that induce the low-energy coupling g_e as in Eq.(2.11) after EWSB, must originate from an ultraviolet completion of the theory, which we now proceed to describe.

We consider a left-handed and a right-handed copies of the right-handed electron, $E_{L,R}$, which are color and $SU(2)_L$ singlets and which have weak hypercharge $Y = -1$. They are also even under the Z_2 symmetry. The renormalizable UV Lagrangian (omitting kinetic terms) reads

$$\begin{aligned} -\mathcal{L}_E = & \bar{L} Y_e H e_R + \bar{L} y_E H E_R + (\mu_E + \lambda_E X_{17}) \bar{E}_L e_R \\ & + (M_E + \lambda'_E X_{17}) \bar{E}_L E_R + \text{h.c.} \end{aligned} \quad (\text{B.3})$$

After electroweak symmetry breaking, H acquires a vacuum expectation value and the terms above generate a 4×4 mass matrix in the (E_L, E_R, e_L, e_r) space. In close analogy with the seesaw-like structure discussed in eq. (A.5), we diagonalize the mass spectrum within the assumption $M_E \gg y_E v_H \gg \mu_E$. The new fermions (E_L, E_R) pair in a new vector-like heavy state of mass $M_E + \mathcal{O}(y_E^2 v_H^2 / M_E)$. Notice that, parameterizing the coupling between the SM electron and the Higgs boson as $\kappa_e m_e h \bar{e} e$, we get $\kappa_e \sim 1 + y_E^2 v_H^2 / m_e M_E$, well below the current limits $\kappa_e \lesssim \mathcal{O}(100)$.

Finally, integrating the heavy fermion, we generate the interaction

$$\frac{\lambda_E y_E v_H}{\sqrt{2} M_E} X_{17} \bar{e} e + \mathcal{O}(y_E^2 v_H^2 / M_E^2). \quad (\text{B.4})$$

is generated. Thus, we can identify the scalar coupling $g_{eX} \sim \lambda_E \tilde{\mu}_E / M_E$.

With a suitable choice of parameters, $(M_E, y_E \lambda_E) \sim \mathcal{O}(100 \text{ TeV}, 0.01)$ provides $g_{eX} \sim 10^{-5}$ and a vector-like electron pair of mass $\sim 100 \text{ TeV}$, which mixes with the electron with mixing angle $\theta_{eE} \sim y_E v_H / M_E \sim 10^{-4}$.

The presence of heavy vector-like leptons offers a characteristic phenomenological handle at high-energy colliders, where they can be directly produced and searched for through their electroweak interactions. A detailed study of these signatures lies beyond the scope of the present thesis, and we refer the interested reader to ref. [48].

Appendix C

Validity of the Narrow-Width and Non-Resonant Approximations

In section 3.4, analytical expressions for the freeze-in abundance from the process $e^+e^- \rightarrow \chi\chi$ were obtained by simplifying the integral in eq. (3.37) in different kinematic regimes of the DM mass with respect to the mediator mass. In this appendix we will assess the validity of those analytical approximations.

By performing a direct numerical integration over \hat{s} , we compare the approximate expressions derived in section 3.4 with the full result, thereby quantifying the accuracy of the corresponding analytic formulas.

In the expression for the abundance in eq. (3.37), the purely kinematical integration over the Mandelstam variable \hat{s} can be isolated as

$$I(m_\chi, m_X, \Gamma_X, m_e) \equiv \int_{\hat{s}_{\min}}^{\infty} d\hat{s} \frac{(\hat{s} - 4m_\chi^2)^{3/2} (\hat{s} - 4m_e^2)^{3/2}}{\hat{s}^{5/2} [\Gamma_X^2 m_X^2 + (m_X^2 - \hat{s})^2]}. \quad (\text{C.1})$$

We begin by considering the resonant regime, in which the center-of-mass energy approaches the pole of the mediator propagator, $\hat{s} \simeq m_X^2$. The presence of a sharp peak at $\hat{s} = m_X^2$ is clearly visible in fig. C.1, where, for simplicity, we have chosen the benchmark value $m_X = 17$ MeV and plotted the integrand for various values of m_χ .

In this situation, the numerical evaluation of the integral in eq. 3.37 requires particular care, due to the Breit-Wigner enhancement near the resonance. In order to properly resolve the peak and ensure numerical stability, we split the integration domain into two separate intervals, namely from 0 to m_X^2 and from m_X^2 to $+\infty$. The integral is then computed numerically in each interval and the two contributions are summed. This procedure avoids instabilities associated with sampling across the resonance and guarantees the convergence of the numerical integration in the resonant regime.

We now compare the numerical value of the integral, I_{Num} , obtained with the procedure described above, with the analytic expression derived in the narrow-width approximation, I_{NWA} , see eq. 3.41.

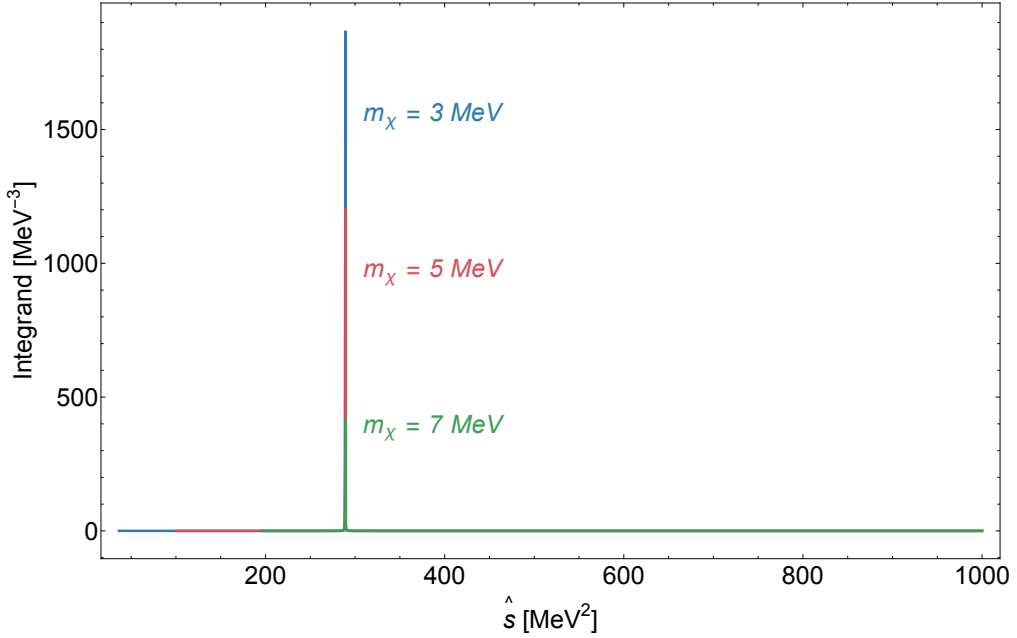


Figure C.1 Integrand in the r.h.s. of Eq.(C.1) as a function of the center-of-mass energy \hat{s} for the benchmark $m_X = 17\text{MeV}$. The three curves correspond to $m_X = \{3, 5, 7\}\text{ MeV}$ (as indicated). A narrow Breit–Wigner peak is clearly visible at $\hat{s} = m_X^2$; away from the pole the integrand decreases rapidly. Axes are linear.

In order to quantify the accuracy of the NWA, we define the relative percentage error as

$$\text{Err} = \left| \frac{I_{\text{NWA}} - I_{\text{Num}}}{I_{\text{NWA}}} \right| \times 100. \quad (\text{C.2})$$

This quantity provides a direct measure of the deviation between the exact numerical result and the analytic approximation obtained in the resonant limit.

We evaluate Err for a range of DM masses m_χ in the resonant regime and display the resulting percentage error as a function of m_χ . We find that the difference between the numerical evaluation and the NWA result is extremely small over the whole range of dark-matter masses considered. Scanning over $\mathcal{O}(10^3)$ values of m_χ in the interval $(1\text{ MeV} - 8.5\text{ MeV})$, and computing the corresponding Err for each point, we evaluate the mean percentage deviation and its standard deviation. The resulting averaged error is

$$\text{Err}_{\text{mean}} \approx 3 \times 10^{-5}\%, \quad (\text{C.3})$$

with a standard deviation

$$\sigma_{\text{Err}} \approx 3 \times 10^{-4}\% \quad (\text{C.4})$$

Both the tiny value of the mean error and the small spread of the distribution confirm that the narrow-width approximation reproduces the full numerical integration with excellent accuracy

throughout the resonant regime. Such a tiny value confirms that the narrow-width approximation reproduces the full numerical integration with excellent accuracy throughout the resonant regime, and validates the use of the analytic expression in our analysis.

In addition to the explicit numerical check above, the validity of the NWA in a thermal bath can be assessed analytically following the criterion proposed in ref. [24]. That work is devoted to a different physical scenario from the one considered here. However, in section F of their third chapter, the authors explicitly study the validity of the NWA for resonant production processes and derive the range of temperatures where the approximation provides an accurate description.

In our case, the role of the mediator discussed in Ref. [24] is played by the scalar X . Translating their results to our notation, and defining the dimensionless width parameter as $\varepsilon \equiv \frac{\Gamma_X}{m_X}$ the corresponding validity range can be expressed in terms of the variable z

$$\sqrt{\varepsilon} \lesssim z \lesssim 14\sqrt{\ln \varepsilon^{-1}}. \quad (\text{C.5})$$

Using the parameter of our setup, $m_X \approx 17 \text{ MeV}$ and a benchmark value for the electron coupling $g_e \approx 5 \times 10^{-4}$, the validity range of the narrow-width approximation translates into the following temperature window:

$$1.0 \times 10^{-4} \lesssim z \lesssim 4.3. \quad (\text{C.6})$$

Since the freeze-in production in our model is dominated around $z \approx 1$, which lies well inside this interval, we conclude that the NWA provides an accurate description of the resonant dynamics in our case.

The analysis above focuses on the resonant regime. For completeness, we have also performed an analogous test in the non-resonant regime, $m_\chi > m_X/2$. In this case the integral $I(m_\chi, m_X, \Gamma_X, m_e)$ in eq. (C.1) is compared with the non-resonant analytic approximation derived in sec. 3.4, and we define a relative error $\text{Err}_{\text{n.r.}}$ in complete analogy with eq. (C.2).

Scanning over $\mathcal{O}(10^5)$ values of m_χ in the non-resonant domain ($8.5 \text{ MeV} \lesssim m_\chi \lesssim 1 \text{ GeV}$), and computing $\text{Err}_{\text{n.r.}}$ for each point, we find that the typical deviation between the analytic estimate and the full numerical result remains at the sub-percent level. In particular, the mean value of the relative error is

$$\text{Err}_{\text{mean, n.r.}} \approx 0.01\%, \quad (\text{C.7})$$

with a standard deviation

$$\sigma_{\text{Err, n.r.}} \approx 0.07\%. \quad (\text{C.8})$$

We therefore conclude that, also in the non-resonant regime, the analytic approximation used in sec. 3.4 provides an accurate description of the exact numerical result for the purposes of our phenomenological analysis.

Bibliography

- [1] A. J. Krasznahorkay et al. Observation of anomalous internal pair creation in ${}^8\text{Be}$: A possible indication of a light, neutral boson. *Phys. Rev. Lett.*, 116:042501, 2016.
- [2] A. J. Krasznahorkay et al. New evidence supporting the existence of the hypothetical X17 particle. *Phys. Rev. C*, 104:044003, 2021.
- [3] A. J. Krasznahorkay et al. Further investigation of the X17 anomaly in ${}^8\text{Be}$ and ${}^{12}\text{C}$. *Universe*, 10:409, 2024.
- [4] F. Bossi et al. Search for a new 17 MeV resonance via e^+e^- annihilation with the PADME Experiment. *JHEP*, 5 2025.
- [5] K. Afanaciev et al. Search for the X17 particle in ${}^7\text{Li}(p, e^+e^-){}^8\text{Be}$ processes with the MEG II detector. *Eur. Phys. J. C*, 85(7):763, 2025.
- [6] Marco Cirelli, Alessandro Strumia, and Jure Zupan. Dark Matter. *JHEP*, 6 2024.
- [7] Yongjun Jiao, Francois Hammer, Haifeng Wang, Jianling Wang, Philippe Amram, Laurent Chemin, and Yanbin Yang. Detection of the Keplerian decline in the Milky Way rotation curve. *Astron. Astrophys.*, 678:A208, 2023.
- [8] N. Aghanim et al. Planck 2018 results. VI. Cosmological parameters. *Astron. Astrophys.*, 641:A6, 2020. [Erratum: *Astron. Astrophys.* 652, C4 (2021)].
- [9] Tim Zimmermann, James Alvey, David J. E. Marsh, Malcolm Fairbairn, and Justin I. Read. Dwarf Galaxies Imply Dark Matter is Heavier than 2.2×10^{-21} eV. *Phys. Rev. Lett.*, 134(15):151001, 2025.
- [10] Scott Tremaine and James E. Gunn. Dynamical role of light neutral leptons in cosmology. *Phys. Rev. Lett.*, 42:407–410, Feb 1979.
- [11] James Alvey, Nashwan Sabti, Victoria Tiki, Diego Blas, Kyrylo Bondarenko, Alexey Boyarsky, Miguel Escudero, Malcolm Fairbairn, Matthew Orkney, and Justin I Read. New constraints on the mass of fermionic dark matter from dwarf spheroidal galaxies. *Monthly Notices of the Royal Astronomical Society*, 501(1):1188–1201, 11 2020.

- [12] Laura Baudis. Dark matter searches. *Annalen der Physik*, 528(1-2):74–83, 2016.
- [13] Daniele Barducci, Davide Germani, Marco Nardecchia, Stefano Scacco, and Claudio Toni. On the Atomki nuclear anomaly after the MEG-II result. *JHEP*, 04:035, 2025.
- [14] Luca Di Luzio, Paride Paradisi, and Nudzeim Selimovic. Hunting for a 17 MeV particle coupled to electrons. *Nucl. Phys. B*, 1021:117177, 2025.
- [15] Daniele S. M. Alves et al. Shedding light on X17: community report. *Eur. Phys. J. C*, 83(3):230, 2023.
- [16] Basabendu Barman, Purusottam Ghosh, Anish Ghoshal, and Lopamudra Mukherjee. Shedding flavor on dark via freeze-in: $U(1)_{B-3Li}$ gauged extensions. *JCAP*, 08(08):049, 2022.
- [17] L. D. Landau. On the angular momentum of a system of two photons. *Dokl. Akad. Nauk SSSR*, 60(2):207–209, 1948.
- [18] C. N. Yang. Selection Rules for the Dematerialization of a Particle Into Two Photons. *Phys. Rev.*, 77:242–245, 1950.
- [19] S. Navas et al. Review of particle physics. *Phys. Rev. D*, 110(3):030001, 2024.
- [20] Lawrence J. Hall, Karsten Jedamzik, John March-Russell, and Stephen M. West. Freeze-In Production of FIMP Dark Matter. *JHEP*, 03:080, 2010.
- [21] Benedetta Belfatto, Dario Buttazzo, Christian Gross, Paolo Panci, Alessandro Strumia, Natascia Vignaroli, Ludovico Vittorio, and Ryoutaro Watanabe. Dark Matter abundance via thermal decays and leptoquark mediators. *JHEP*, 06:084, 2022.
- [22] Ludovico Vittorio. The precision era of flavour physics: from hadronic form factors to dark matter. *Eur. Phys. J. Plus*, 140(6):590, 2025.
- [23] Edward W. Kolb and Michael S. Turner. *The Early Universe*, volume 69. Taylor and Francis, 5 2019.
- [24] Julian Heeck. Unbroken B – L symmetry. *Phys. Lett. B*, 739:256–262, 2014.
- [25] Nicole F. Bell, Matthew J. Dolan, and Sandra Robles. Searching for Sub-GeV Dark Matter in the Galactic Centre using Hyper-Kamiokande. *JCAP*, 09:019, 2020.
- [26] Marco Cirelli, Nicolao Fornengo, Bradley J. Kavanagh, and Elena Pinetti. Integral X-ray constraints on sub-GeV Dark Matter. *Phys. Rev. D*, 103(6):063022, 2021.
- [27] Laurent Bouchet, Andrew W. Strong, Troy A. Porter, Igor V. Moskalenko, Elisabeth Jourdain, and Jean-Pierre Roques. Diffuse emission measurement with the spectrometer on integral as an indirect probe of cosmic-ray electrons and positrons. *The Astrophysical Journal*, 739(1):29, sep 2011.

- [28] Marco Cirelli, Nicolao Fornengo, Jordan Koechler, Elena Pinetti, and Brandon M. Roach. Putting all the x in one basket: Updated x-ray constraints on sub-gev dark matter. *Journal of Cosmology and Astroparticle Physics*, 2023(07):026, jul 2023.
- [29] Joshua W. Foster, Marius Kongsore, Christopher Dessert, Yujin Park, Nicholas L. Rodd, Kyle Cranmer, and Benjamin R. Safdi. Deep Search for Decaying Dark Matter with XMM-Newton Blank-Sky Observations. *Phys. Rev. Lett.*, 127(5):051101, 2021.
- [30] Roman Krivonos, Daniel Wik, Brian Grefenstette, Kristin Madsen, Kerstin Perez, Steven Rossland, Sergey Sazonov, and Andreas Zoglauer. *NuSTAR* measurement of the cosmic X-ray background in the 3–20 keV energy band. *Mon. Not. Roy. Astron. Soc.*, 502(3):3966–3975, 2021.
- [31] JaeSub Hong et al. NuSTAR Hard X-ray Survey of the Galactic Center Region II: X-ray Point Sources. *Astrophys. J.*, 825(2):132, 2016.
- [32] T. Yoshino et al. Energy Spectra of the Soft X-ray Diffuse Emission in Fourteen Fields Observed with Suzaku. *Publ. Astron. Soc. Jap.*, 61:805, 2009.
- [33] Julio F. Navarro, Carlos S. Frenk, and Simon D. M. White. The Structure of cold dark matter halos. *Astrophys. J.*, 462:563–575, 1996.
- [34] Yu. M. Bystritskiy, E. A. Kuraev, G. V. Fedotovich, and F. V. Ignatov. Cross sections of muon and charged pion pair production in electron-positron annihilation near the threshold. *Phys. Rev. D*, 72:114019, Dec 2005.
- [35] Paolo Gondolo and Graciela Gelmini. Cosmic abundances of stable particles: Improved analysis. *Nucl. Phys. B*, 360:145–179, 1991.
- [36] Hitoshi Murayama. Resonant Annihilation of WIMP Dark Matter for Halo Gamma Ray Signal. *Phys. Rev. D*, 12 2025.
- [37] Digvijay Wadekar and Zihui Wang. Strong constraints on decay and annihilation of dark matter from heating of gas-rich dwarf galaxies. *Phys. Rev. D*, 106(7):075007, 2022.
- [38] X. Fan, T. G. Myers, B. A. D. Sukra, and G. Gabrielse. Measurement of the Electron Magnetic Moment. *Phys. Rev. Lett.*, 130(7):071801, 2023.
- [39] R. Eichler et al. Limits for Shortlived Neutral Particles Emitted μ^+ or π^+ Decay. *Phys. Lett. B*, 175:101, 1986.
- [40] S. Egli et al. Measurement of the Decay $\pi^+ \rightarrow e^+ \nu_e e^+ e^-$ and Search for a Light Higgs Boson. *Phys. Lett. B*, 222:533–537, 1989.
- [41] W. Altmannshofer et al. PIONEER: Studies of Rare Pion Decays. 3 2022.

- [42] K. Arndt et al. Technical design of the phase I Mu3e experiment. *Nucl. Instrum. Meth. A*, 1014:165679, 2021.
- [43] W. Elbers et al. Constraints on neutrino physics from DESI DR2 BAO and DR1 full shape. *Phys. Rev. D*, 112(8):083513, 2025.
- [44] Palash B. Pal and Lincoln Wolfenstein. Radiative Decays of Massive Neutrinos. *Phys. Rev. D*, 25:766, 1982.
- [45] Rouven Essig, Eric Kuflik, Samuel D. McDermott, Tomer Volansky, and Kathryn M. Zurek. Constraining Light Dark Matter with Diffuse X-Ray and Gamma-Ray Observations. *JHEP*, 11:193, 2013.
- [46] Mathieu Boudaud, Julien Lavalle, and Pierre Salati. Novel cosmic-ray electron and positron constraints on MeV dark matter particles. *Phys. Rev. Lett.*, 119(2):021103, 2017.
- [47] Hongwan Liu, Wenzer Qin, Gregory W. Ridgway, and Tracy R. Slatyer. Lyman- α constraints on cosmic heating from dark matter annihilation and decay. *Phys. Rev. D*, 104(4):043514, 2021.
- [48] Zijie Poh and Stuart Raby. Vectorlike leptons: Muon g-2 anomaly, lepton flavor violation, Higgs boson decays, and lepton nonuniversality. *Phys. Rev. D*, 96(1):015032, 2017.

Acknowledgments

We would first like to express our deepest gratitude to Federico Mescia for his constant guidance, support, and encouragement throughout the entire development of this thesis. We would also like to express our sincere gratitude to Claudio Toni for his continuous support and availability. His experience and expertise on the X_{17} topic have significantly contributed to clarifying many theoretical and phenomenological aspects addressed in this thesis.